Charge and spin order in highly stoichiometric $YFe_2O_{4-\delta}$ single crystals

von

Thomas Müller

Diplomarbeit in Physik

vorgelegt der

Fakultät für Mathematik, Informatik und Naturwissenschaften
der RWTH Aachen

im Juni 2012

angefertigt am

Peter Grünberg Institut PGI und Jülich Centre for Neutron
Science JCNS, JARA-FIT, Forschungszentrum Jülich

bei

Prof. Dr. Manuel Angst

CONTENTS

1

INTRODUCTION

Solid states physics has always been the driving force for future information technology. Moore's law [1] predicting the doubling of the number of the transistors in a single integrated circle is always quoted as motivation for information technology development. The speed of increasing information storage space following Kryder's Law makes Moore's law appear like a snail [2]. One main aspect on the development route to denser storage media is the heat problem. Magnetic bits in storage devices are written by magnetic moments induced by electric currents following Faraday's law. These currents produce a lot of waste heat, which sets limits to the miniaturization process. One way to overcome this problem would be a good multiferroic material. Multiferroic in this sense means an ferroelectric (anti-)ferromagnet, with coupling between both (Figure 1.1) [3]. In such a system switching the magnetic moment with an electric field instead of electric currents would be possible, eliminating the heat problem [4]. Unfortunately multiferroics are rare, those with coupling are even rarer [5] and materials with such behavior at room temperature are almost not present. This is normally caused by the contradicting symmetry conditions leading to ferroelectricity or ferromagnetism. Ferroelectricity needs breaking of space inversion symmetry, while ferromagnetism requires violation of time inversion symmetry. Therefore Multiferroics require violations of both [6]. Besides different theories multiferroicity driven by charge ordering has come up to be a promising approach. And from Ikeda's famous nature paper [7], $LuFe_2O_4$ has been the primary example for a multiferroic with ferroelectricity driven by charge ordering. Recent studies by de Groot et al. [8] showed that

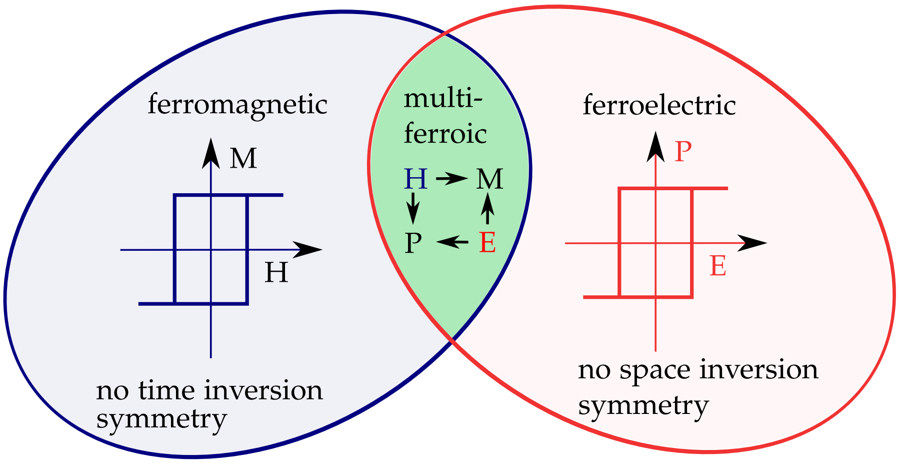

Figure 1.1: Schematic view of ferroic behaviour.

the charge ordering in $LuFe_2O_4$ is incompatible with the ferroelectricity model proposed by Ikeda. Making ferroelectricity in $LuFe_2O_4$ unlikely. This result is further affirmed by broadband dielectric measurements of Niermann et al. [9] and Ruff et al. [10]. Nevertheless $LuFe_2O_4$ stays an interesting highly correlated electron system. About other rare earth ferrites there is much less known, which made us focus on the isostructural $YFe_2O_{4-\delta}$. As for $LuFe_2O_4$, oxygen stoichiometry is an essential parameter for charge and magnetic long-range ordering. Up to now stoichiometric single crystals of $YFe_2O_{4-\delta}$ were, despite many attempts, not available. To understand the charge and spin structure in highly ordered systems, single crystalline samples are necessary and scattering methods are the key technology to examine and understand the microscopic origin of macroscopic properties. X-ray diffraction is used to determine the structure of $YFe_2O_{4-\delta}$and charge ordering, while resonant x-ray diffraction and x-ray absorption spectroscopy, to calculate the x-ray magnetic circular dichroism signal, are used to analyze orbital, charge and magnetic ordering. To examine the magnetic structure neutron, diffraction is the most promising technique. At room temperature $YFe_2O_{4-\delta}$ is a rhombohedral structure with space group $R\bar{3}m$, like $LuFe_2O_4$at higher temperatures. Figure 1.2 shows the structure of $YFe_2O_{4-\delta}$, which consists of alternating triangular layers of Y, O and Fe stacked along crystallographic c-axis. Between two Yttrium layers, there is always a double layer of Fe, which mainly controls the magnetic behaviour, since elemental Y has an electron configuration of $[Kr]4d^1 5s^2$ and therefore Y^{3+} has no unpaired spin moments.

In such a triangular lattice the mean Fe valence in $YFe_2O_{4-\delta}$ of 2.5, which originates from equal parts of Fe^{2+} and Fe^{3+} cannot be fulfilled, which leads to charge frustration, as shown schematically in Figure 1.3. Also an anti-ferromagnetic spin arrangement leads to a frustrated third position on the triangular lattice. Such frustration can lead to complex charge and spin states, or long-range order.

1.1 A BRIEF HISTORY OF $YFe_2O_{4-\delta}$

In 1975 Kimizuka and Katsura [12] found $YFe_2O_{4-\delta}$ as a new phase in the Fe-Fe_2O_3-Ye_2O_3-system. By powder X-ray diffraction, wet-chemical analysis and thermogravimetric measurements they established the phase diagram of the Fe-Fe_2O_3-Ye_2O_3-system at 1200 °C (Fig. 1.4). $YFe_2O_{4-\delta}$ is isostructural to $LuFe_2O_4$ at room temperature with space group $R\bar{3}m$.

In 2004 Kitayama et al. [13] established the phase diagram of the Y-Fe-O-system at 1100°C, in which $YFe_2O_{4-\delta}$ is completely absent.

The first single crystal of $YFe_2O_{4-\delta}$ was grown by Shindo et al. in 1976 [14]. These crystals have been widely studied by magnetic and Mössbauer measurements [15] as well with neutron diffraction [16].

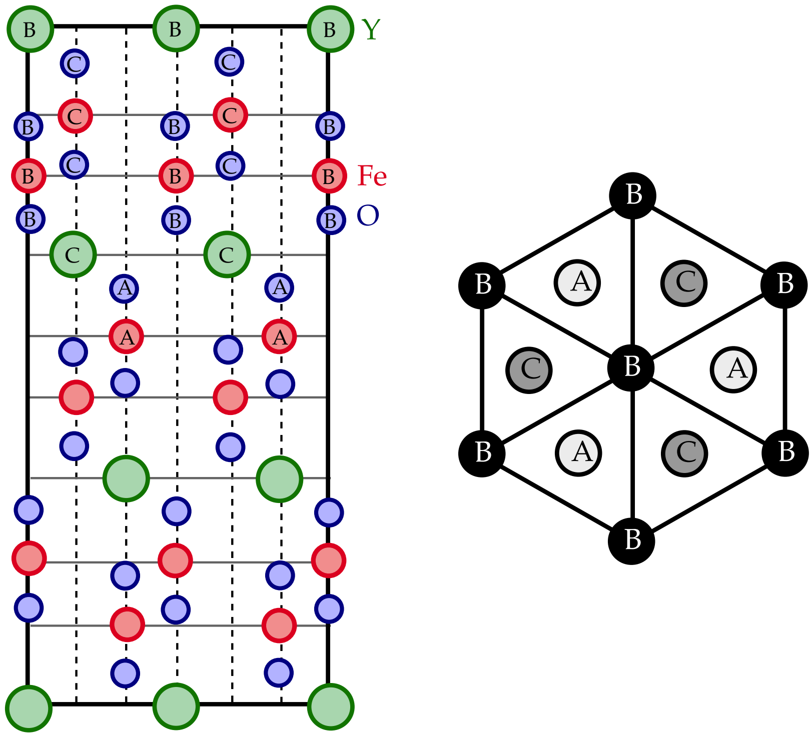

Figure 1.2: Rhombohedral R$\bar{3}$m crystal structure of $YFe_2O_{4-\delta}$ at room temperature. The right part is the projection in **c**-plane, which shows three trigonal layers A, B and C stacked along c-axis as shown in the left part of the figure. The colours of the A, B and C positions identify the occupation by O, Fe or Y. Figure adopted from [7].

In these crystals, the increase of magnetization below 150 K under an applied field, shown in Figure 1.6, was described as "Parasitic Ferrimagnetism" by Sugihara et al. [15]. The magnetization shows one broad glassy maximum in the magnetization during field warming around 200 K and a strong remanent magnetization induced by a previously applied field under cooling.

In 1979 Nakagawa et al. [17] found, that through a well controlled oxygen partial pressure during synthesis and rapid quenching after calcination, it is possible to receive stoichiometric $YFe_2O_{4-\delta}$ powder. They observed a two step anti-ferromagnetic transition in the magnetization curve around 240 K with a huge thermal hysteresis. This transition is also structural, during cooling the rhombohedral R$\bar{3}$m lattice is distorted to a monoclinic one and on further cooling crystal symmetry is lowered to triclinic [17]. The lattice parameters of these three phases can be found in Table 1.1. The difference in magnetization in dependence of the previously applied cooling field is absent in these samples. Inazumi et al. [18] evaluated the magnetic behaviour in dependence of oxygen off-stoichiometry (Figure 1.7 and 1.8). The magnetic behaviour (Figure 1.6) of the crystals grown by Shindo et al. [14] is the same as that of oxygen deficient powder samples [18]. A single crystal growth of stoichiometric YFe_2O_4 is up to now, despite

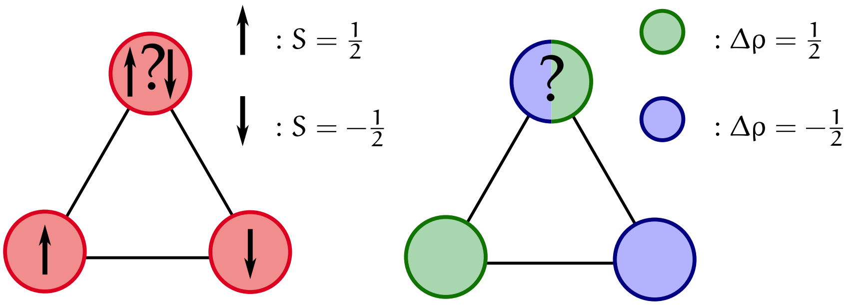

Figure 1.3: Spin and charge frustration in a triangular lattice. Figure adopted from [11].

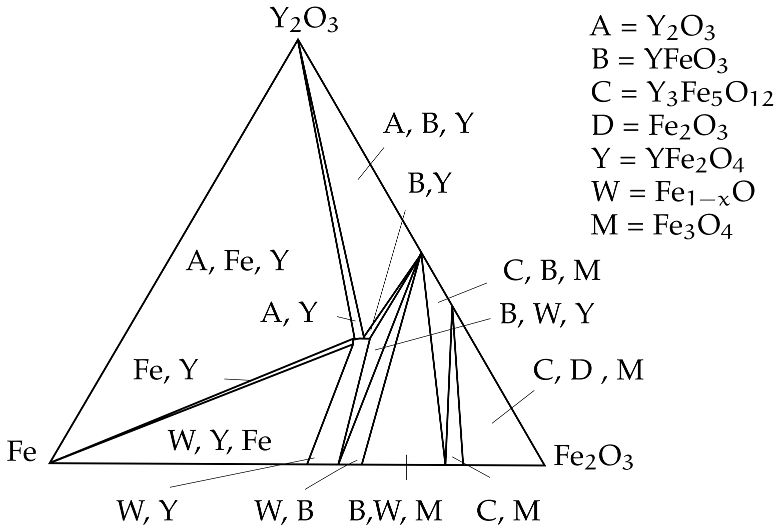

Figure 1.4: Phasediagram of the Fe-Fe_2O_3-Ye_2O_3-system at 1200 °C [12].

many attempts [19], not reported. Charge and spin ordering [16] in these crystals are two-dimensional down to 10 K.

Matsui et al. [20] was the first who examined the superstructure in stoichiometric $YFe_2O_{4-\delta}$ with electron diffraction. Single crystals used for electron diffraction are very small and received from polycrystalline sintered samples. In oxygen deficient samples diffuse lines along $(1/3\ 1/3\ \ell)$ are reported, indicating no long-range order in ℓ-direction, of still ordered layers. The observed lines are slightly twisted indicating non perfect two-dimensional ordering in plane [20]. In stoichiometric samples diffuse lines in $hh\ell$ are replaced by superstructure reflection which can be indexed as $(1/3\ 1/3\ 1/2)$ and $(1/3\ 1/3\ 3/2)$ [20]. These reflections vanish with increased beam intensity, which is interpreted as defect healing under heating [20]. In 1982 Tanaka et al. [21] tried to anneal non-stoichiometric single crystals to increase the oxygen amount. While the magnetic behaviour was improved it was not the same as for stoichiometric samples [21]. They also measured electric resistivity in stoichiometric samples which decreases while warming through both magnetic transitions, in contrast to specific heat which increases through the presence of latent heat being

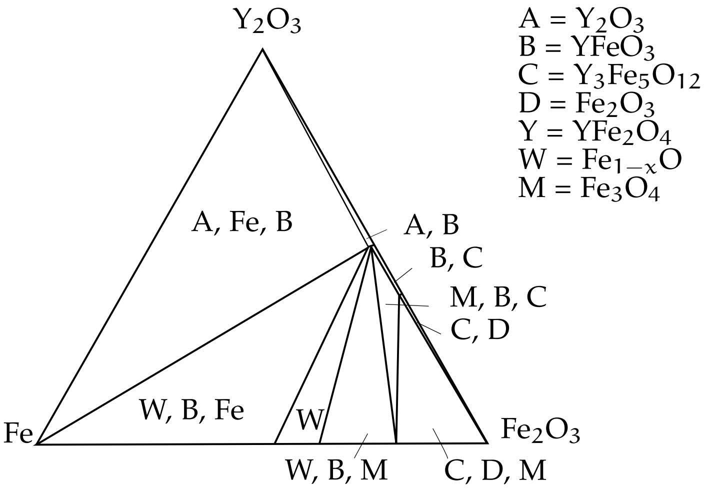

Figure 1.5: Phasediagram of the Fe-Fe_2O_3-Ye_2O_3-system at 1100 °C [13].

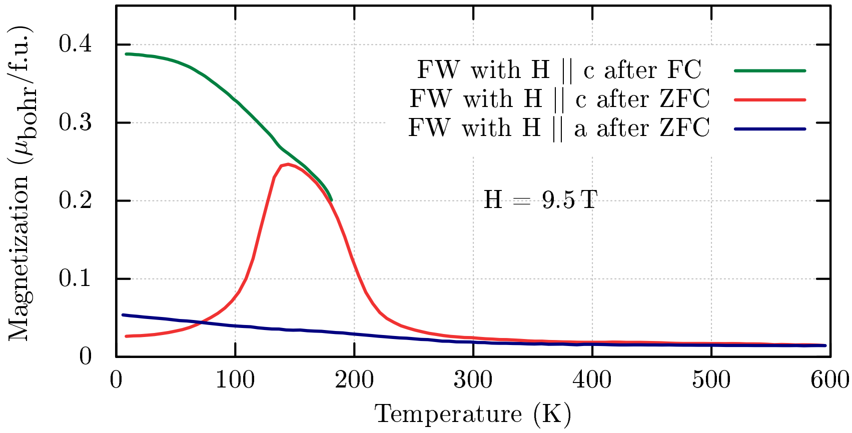

Figure 1.6: Magnetization of non-stoichiometric $YFe_2O_{4-\delta}$ single crystal. (Data taken from [15]).

characteristic for a first order transition [21]. The thermal hysteresis in magnetization [17] and electric resistivity [21] further affirms the first-order character of the transitions. As does the thermal hysteresis and the coexistence of two phases near the transition point in Mössbauer spectroscopy [22]. Kishi et al. [23] and later Siratori et al. [24] as well as Serrao et al.[25] substituted Y in $YFe_2O_{4-\delta}$ with Lu, while Noh et al. [26] substituted Y in $LuFe_2O_4$. Interpretation without addressing different stoichiometry for the substituted samples is difficult. Enomura et al. [27] and Sakai et al. [28] measured the Seebeck coefficient of $YFe_2O_{4-\delta}$. At 4.2 K in fields up to 23 T Iida et al. [29] observed hysteric behaviour in M(H)-curve of non-stoichiometric $YFe_2O_{4-\delta}$. The thermoremanent magnetization after cooling in 23 T field at 4.2 K is with 1.5 μ_{bohr}/f.u. in $YFe_2O_{4-\delta}$ only half as strong as in $LuFe_2O_4$, where it has a value of 2.8 μ_{bohr}/f.u. [29]. Instead of $LuFe_2O_4$, were the thermoremanent magnetization is saturated above 10 T, in $YFe_2O_{4-\delta}$ saturation is not observed up to

Temperature (K)	290	222	77
a (Å)	3.513	3.534	3.574
b (Å)	3.513	3.513	3.540
c (Å)	24.779	24.771	24.505
α (deg)	90	90.23	90.43
β (deg)	90	89.54	88.82
γ (deg)	120	120.20	120.62
V ($Å^3$)	264.83	265.74	266.78

Table 1.1: Lattice parameters of stoichiometric $YFe_2O_{4-\delta}$ from [17].

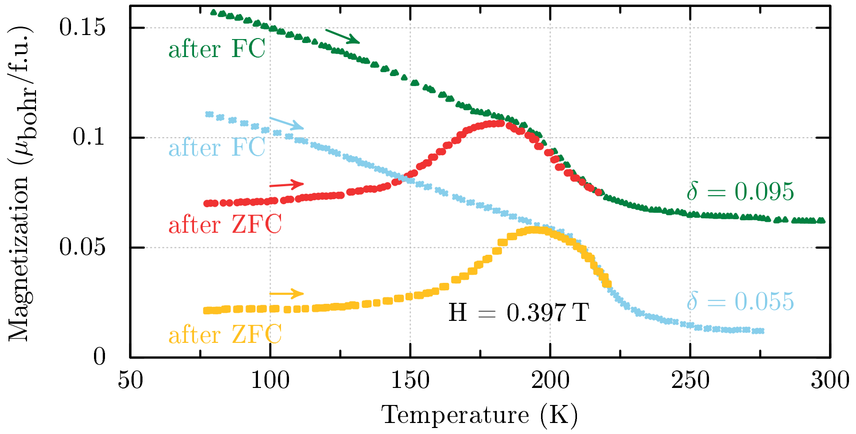

Figure 1.7: Magnetization of $YFe_2O_{4-\delta}$ powder samples with different off-stoichiometry (Data taken from [18].) All curves are measured during warming, with previous cooling in a field $H = 0.397\,T$ (FC) or without applied field ZFC.

29 T [29]. This might indicate that anti-ferromagnetic ordering of the triangular Fe arrangement [30] is stronger distorted in $YFe_2O_{4-\delta}$ compared to $LuFe_2O_4$ where the TRM has almost the value $3\,\mu_{bohr}/f.u.$ expected for perfect 2:1-ferrimagnetic ordering [29]. The influence of pressure on the magnetic behaviour of $YFe_2O_{4-\delta}$ was examined by Siratori et al. [24] and Matsumoto et al. [31, 32]. Katano et al. [33] refined the structure at 225 K from powder neutron diffraction on stoichiometric $YFe_2O_{4-\delta}$. With polarization analysis they separated magnetic scattering, which consists of incommensurate not identified peaks [33], completely different to the diffuse magnetic lines observed in non-stoichiometric samples [19, 34].

Huge temperature dependent variations in the dielectric constant were observed by Ikeda et al. [35] and Horibe et al. [36]. As $YFe_2O_{4-\delta}$ [21, 37] has comparable conductivity to $LuFe_2O_4$ [38] the influence of contacts has to be reviewed carefully in dielectric spectroscopy measurements, as it was done for $LuFe_2O_4$ in [9] and [10]. Recently

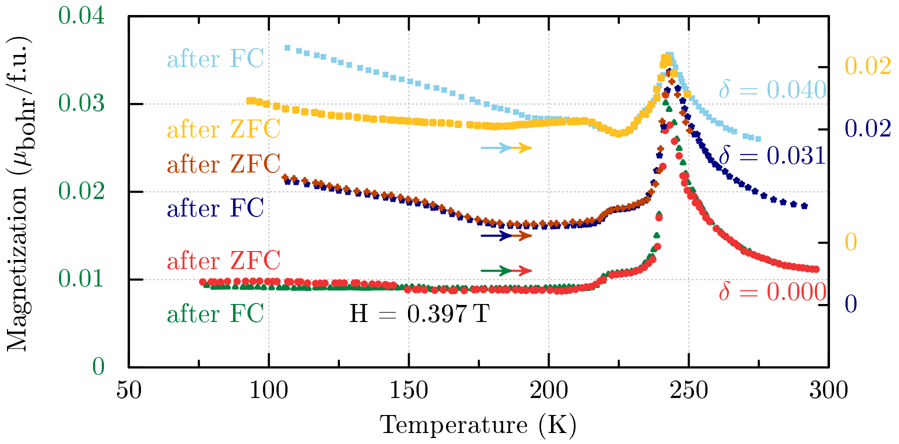

Figure 1.8: Magnetization of $YFe_2O_{4-\delta}$ powder samples with different off-stoichiometry and stoichiometric oxygen amount (Data taken from [18]. The upper four curves are shifted for clarity by $0.007\mu_{bohr}$/f.u.) and $0.014\mu_{bohr}$/f.u.) respectively, as in [18]. All curves are measured during warming, with previous cooling in a field H = 0.397 T (FC) or without applied field ZFC.

several electron diffraction studies reported different kinds of 3D-charge ordering in stoichiometric $YFe_2O_{4-\delta}$. Ikeda et al. [35] observed diffuse scattering along (1/3 1/3 ℓ) at room temperature, which converts at 250 K to superstructure reflections at (1/3 1/3 half-integer) accompanied by peak splitting of the (1 0 1) reflection. Cooling to 225 K, the propagation vector changes to (1/2 1/2 integer) or (1/6 1/6 integer) [35]. Discontinuities in the diffraction at 150 K of the (1 0 10) reflection and at 60 K and 40 K on the (1 1 0) reflection indicate more phase transitions [35]. Below 60 K diffuse scattering around (1/3 1/3 4.5) is again observed [35]. On warming from 130 K the propagation vector changes from (1/3 1/3 0) at 130 K, over (1/7 1/7 0) between 135 and 140 K to (1/4 1/4 0) below 190 K and further from (1/2 1/2 0) between 200 and 225 K to (1/3 1/3 0) at 233 K [7]. At 150 K Horibe et al. [36] observed the same (1/4 1/4 integer) reflections which convert to (0 1/2 0) type at 200 K and are replaced above 250 K by diffuse scattering along (1/3 1/3 ℓ) with incommensurate weak peaks at (1/3-τ 1/3-τ 0) with $\tau \approx 0.11$. In 2005 the propagation vector in this phase was identified by the same group as (1/3-τ 1/3-τ 0) with $\tau \approx 0.066$ [39]. Mori et al. [40] studied the charge ordering in $YFe_2O_{4-\delta}$ in dependence of oxygen vacancies. In samples with the lowest oxygen deficiency three-dimensional charge ordering is already observed at room temperature, which consist of (1/3 1/3 1/2) reflections superposing the diffuse lines along (1/3 1/3 ℓ) [40]. This 3D-ordering vanishes between 368 K and 475 K , while in samples with more oxygen vacancies charge ordering is two-dimensional already at room temperature [40]. The effect of oxygen deficiency on charge and spin ordering was further investigated by Horibe et al. [41]. They observed the same $(1/3\ 1/3\ 1/2)$ superstructure reflections at room temperature with additional $(1/3\ 1/3\ 3/2)$ reflections due to twinning [41]. At 100 K they are replaced by $(1/7\ 1/7\ 9/7)$ reflections in the samples with the least oxygen vacancies [41]. With higher oxygen deficiency only two-dimensional scattering is observed at room temperature, which is accompanied with $(1/3\ 1/3\ 1/2)$ reflections at 100 K [41]. Even higher oxygen deficiency leads to zig-zag type diffuse scattering at room temperature which converts to straight diffuse scattering along $(1/3\ 1/3\ \ell)$ at 100 K [41]. The transition temperatures decrease with increasing oxygen deficiency [41]. Another intensive study by the same group on the low temperature phase came to the conclusion, that the electron diffraction at 100 K is described by a modulation wave vector of $(\overline{1/14}\ 2/7\ 1/14)$.

2

EXPERIMENTAL TECHNIQUES AND THEORY

This chapter gives a detailed description of the experimental methods used during this thesis, including the necessary theoretical background beyond the common solid state physics.

2.1 POWDER SYNTHESIS AND CHARACTERISATION TECHNIQUES

At the beginning of new materials research is always sample preparation. For single crystal growth using the floating zone technique, polycrystalline rods of $YFe_2O_{4-\delta}$ are needed, therefore this section describes the synthesis process and examination methods for polycrystalline samples.

2.1.1 *Synthesis process*

The synthesis process (Fig. 2.1) follows the procedure described by Shindo et al. [14]. Powdered Fe_2O_3 and Ye_2O_3 are mixed in the stoichiometric ratio, i.e. one part Ye_2O_3 to two parts of Fe_2O_3 (equivalent in mass percent 41.42 of Ye_2O_3 to 58.58 of Fe_2O_3). The mixture is ball-milled under isopropanol in an aluminium oxide crucible for several hours to reduce the grain size and obtain a homogeneous composition. Under nitrogen atmosphere the powder is dried at 70 °C, which is below the boiling point of isopropanol, for at least 12 hours. The material is then filled to an aluminium oxide boat and placed in an already hot tube furnace at 1250 °C under controlled oxygen atmosphere. Fixing the flow rate of CO_2 and H_2 at a constant temperature gives us a very precise way to control oxygen partial pressure.

The equilibrium reaction between CO_2, H_2 and H_2O,

$$\begin{aligned} CO_2 &\rightleftharpoons CO + \tfrac{1}{2}\,O_2 \\ CO_2 + H_2O &\rightleftharpoons H_2 + CO \\ H_2O &\rightleftharpoons H_2 + \tfrac{1}{2}\,O_2 \end{aligned}$$

produces a reduced oxygen atmosphere, which is essential to control the coexistence of bivalent and trivalent iron in the $YFe_2O_{4-\delta}$-system [14]. To prevent an explosive H_2-concentration a gas mixture of 4 % H_2 to 96 % Ar is used. The iron valence is triggered by the reaction of the starting material with the ambient oxygen.

$$2Fe^{2+} + \tfrac{1}{2}\,O_2 \rightleftharpoons 2\,Fe^{3+} + O^{2-}$$

Subsequent quenching has been found to be essential to obtain $YFe_2O_{4-\delta}$ as the only phase [17]. After about 16 hours the calcined material is therefore quenched (in ca. 5 min) from 1250 °C to slightly above room temperature, by pulling the boat to the end of the aluminium oxide tube. As for $LuFe_2O_4$ [11], exposing the hot material to atmospheric oxygen concentrations will immediately lead to partial decomposition of the $YFe_2O_{4-\delta}$. In case of the $YFe_2O_{4-\delta}$ the most common foreign phases are Wüstite and perovskite type $YFeO_3$. To avoid foreign phases the quenching is performed within the reduced oxygen atmosphere, where the material will cool down for another hour, before it is exposed to normal atmosphere. Again the material is ball-milled under isopropanol and finally dried.

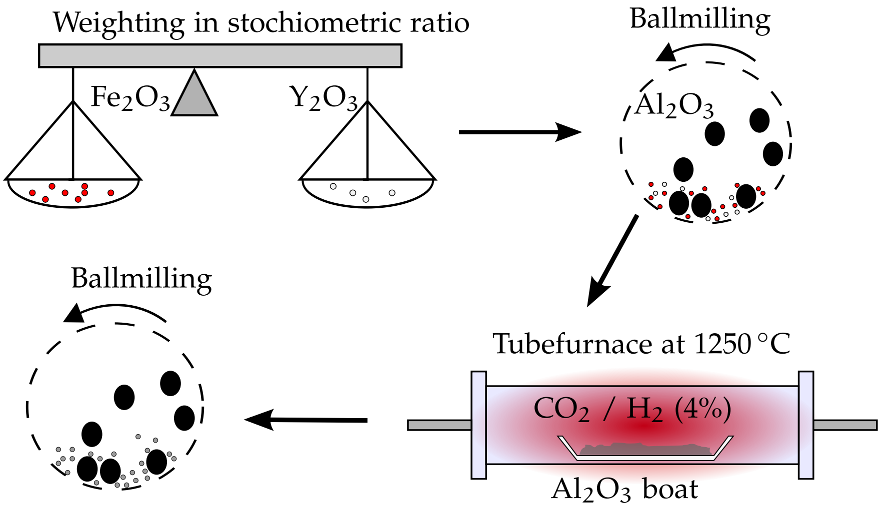

Figure 2.1: Process-diagram of the powder synthesis.

$YFe_2O_{4-\delta}$ is absent in the phasediagram at 1100 °C established by Kitayama et al. (Fig: 1.5), which is in contradiction to the results from Piekarczyk et al. [42], who observed $YFe_2O_{4-\delta}$ be present above 1010 ± 9 °C. Nevertheless both results give a lower temperature border for the appearance of $YFe_2O_{4-\delta}$ in the phasediagram. The quenching process is therefore necessary to reach a metastable state containing $YFe_2O_{4-\delta}$ at room temperature.

Different powder samples exhibiting varying oxygen deficiency were prepared, by the previous described solid state reaction. Tab. 2.1 shows the used gas mixtures, beside the starting material and the synthesis time.

2.1.2 *Powder x-ray diffraction*

Powder Diffraction on the calcined $YFe_2O_{4-\delta}$ samples is performed for two reasons. First to check if the material is single phase, without impurities from other phases, and second to investigate if there is some influence from the stoichiometry on the lattice constants. If such an influence exists, it is expected to be quite small [18]. Powdered samples consist of randomly oriented very small crystallites, through

Name	CO_2 (ml/min)	H_2 4% (ml/min)	CO_2/H_2	starting material	time (h)
C001	3.00	30	2.50	$Fe_2O_3 + Y_2O_3$	16
C002	4.00	30	3.33	C001	6
C003	5.00	30	4.17	C001+C002	16
C004	7.00	30	5.83	$Fe_2O_3 + Y_2O_3$	16
C005	6.00	30	5.00	$Fe_2O_3 + Y_2O_3$	19
C006	4.50	30	3.75	C005	5
C007	5.50	30	4.58	C005	19
C008	5.50	30	4.58	C005	10
C009	6.50	30	5.42	C007	3
C011	6.80	30	5.67	C001	15
C012	3.50	30	2.92	$Fe_2O_3 + Y_2O_3$	>12
C013	5.70	30	4.75	$Fe_2O_3 + Y_2O_3$	>12
C014	5.25	30	4.38	C011	20
C015	4.80	30	4.00	C012	22
C016	5.00	30	4.17	$Fe_2O_3 + Y_2O_3$	>12
C017	2.00	30	1.67	$Fe_2O_3 + Y_2O_3$	>12
C018	5.00	30	4.17	$Fe_2O_3 + Y_2O_3$	>12

Table 2.1: Overview of different calcination conditions. Temperature was 1250 °C — Annotations: C011 was calcined at 1220 °C, C005 was inserted into a cold furnace, C007 was exposed to air before the sample was cold.

this random orientation of the lattice planes, the three-dimensional condition in Braggs law is reduced to one dimension, normally represented by the scattering angle 2θ. And for varying 2θ it is in principle possible to receive constructive interference for every set of lattice planes. The scattering angle 2θ is directly connected to the interplanar spacing d through brags law $n\lambda = 2d\sin\theta$.

All powder diffraction experiments were performed at room temperature, using a Cu-anode, a Ge(111) monochromator (wavelength 1.54 Å) and a Huber G670 Gunier-camera in transmission geometry.

For all synthesized samples from Tab. 2.1 powder diffractograms were collected, with one hour counting time. Powder diffraction was performed after each synthesis. To minimize the influence of the instrumental parameters, all powder measurements were repeated consecutive, without any change on the instrumental setup and without perturbation through other users. The obtained profiles were matched by le-Bail-refinement [43] using Jana2006 [44] to obtain lattice constants. Further structural refinement was not done due to the focus on crystal growth. To exclude subjective influence on the refinement process, the refinement was done without knowledge of the synthesis conditions of the refined sample.

2.1.3 *Magnetometry*

Since the magnetization of $YFe_2O_{4-\delta}$ powder for diversifying δ is well known [18], magnetization measurements give us a good way of quality control for different powder calcinations. The magnetization measurements performed on powder samples were all performed on a Quantum Design PPMS using the vibrating sample magnetometer option (VSM). The PPMS offers an environment with controlled magnetic field up to 9 T and temperature down to 4.2 K. The VSM option is built of a motor unit and some pick up coils. The motor unit vibrates the sample, mounted on a long stick reaching in the vacuum chamber, in a magnetic field. This will, following Faradays law, induce a voltage in the sample surrounding pick up coils, which is directly addicted to the magnetization of the sample.

For a low background signal the sample holder should be perfectly homogeneous, on the other hand the relative position of the sample to the sample stick must be fixed.

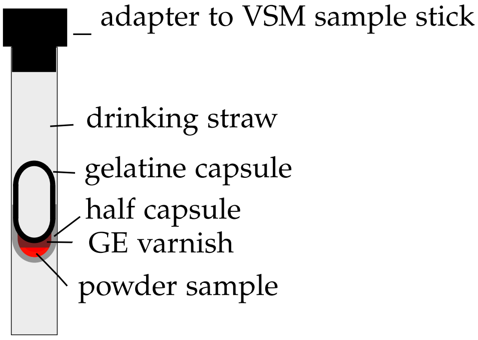

Figure 2.2: Powder sample holder for the PPMS VSM.

The sample holder construction shown schematic in Fig. 2.2 is a necessary departure frm homogeneity to secure a powder sample. An amount of powder in the 10 mg region is placed in a half gelatine capsule and as less as possible GE varnish is applied to the top of the powder. After that the whole construction is compressed and enclosed by another gelatine capsule, which is pressed into the previous one. The complete sample enclosure is placed in a plastic drinking straw which can be connected to the VSM sample stick. To secure the capsule in the straw and for a better gas exchange, small holes are pierced through the straw and the capsule.

2.2 CRYSTAL GROWTH

For scattering investigations, which should lead to a better understanding of the charge ordering and magnetic transitions, a stoichiometric single crystal is desirable, since stoichiometric powder shows large differences, compared to oxygen deficient samples.

Controlling the oxygen partial pressure during growth in a very small range is essential to obtain stoichiometric single crystals. With increasing oxygen partial pressure the probability of the occurrence of foreign phases during crystal growth increases, due to the very small region in the phase diagram Fig. 1.4, where $YFe_2O_{4-\delta}$ is the only phase.

Shindo et al. [14] used the optical floating zone technique, which offers several advantages, like the missing crucible, the small molten zone, and the very good atmospheric control all around the melt. The optical floating zone method with a CO-CO_2-atmosphere was used to grow highly stoichiometric single crystals of $LuFe_2O_4$ [45]. In contrast to the H_2-CO_2-atmosphere, the CO-CO_2-atmosphere does not produce water, which has been found to disturb the crystal growth [46].

2.2.1 *Growth procedure*

Polycrystalline powder has been prepared using the method described in Section 2.1.1. Finely ground powder is tamped in a latex tube which is hold in form by two halves of an aluminium tube. The filled tube is placed in a hydrostatic press and exposed to a pressure of ca. 30 MPa. After removing the rod from the press, the latex tube is cut apart using a hot scalpel. The rod is gently placed in an aluminium boat and slowly inserted into the already hot tube furnace at 1250 °C. After at least 12 h the sintered rod is slowly pulled to the cold front part of the tube under controlled oxygen atmosphere and remained there for one hour to cool to room temperature. An overview about the procedure can be found in Fig. 2.3.

The mirror furnace consists of four mirrors, equipped with halogen lamps, which surround a quartz-glass tube, see Fig. 2.3. The quartz-glass tube is flushed with a CO-CO_2-mixture, in a desired ratio. Two sintered rods, one as seed and the other as feed are mounted in the quartz-tube. In the focus of the halogen lamps the two rods are molten and connected by the melt. The rods are counter rotating against each other to mix the melt. Both rods move downwards by 1 mm/h trough the focus, and therefore establish a travelling floating zone. At the border between melt and solid crystallites arise. Due to thermodynamic preferences molecules from the melt settle down at this crystallites, making them larger. In some cases larger crystallites suppress the others and only one single crystal continuous growing.

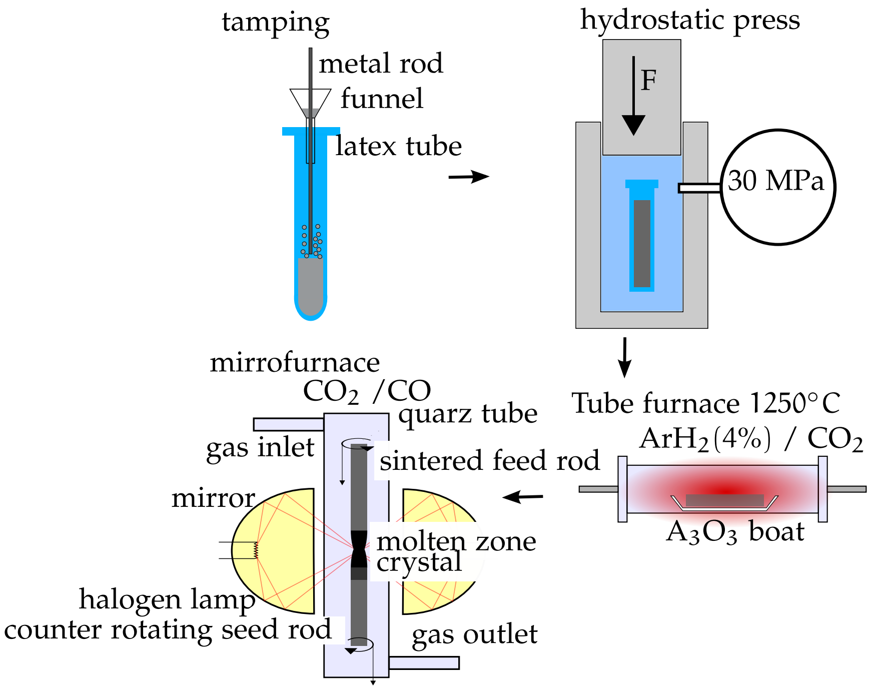

Figure 2.3: Schematic view of the crystal growth procedure.

An overview of the conditions during growths under different CO / CO_2 ratios, i. e. oxygen partial pressures, can be found in Tab. 2.2.

To receive small single crystals from the grown bowl, the growth is cut in to slices using a diamond wire saw. The slices are crushed with a hammer and the splinters are checked under an optical microscope.

2.2.2 *Magnetometry*

Since the magnetic behaviour of stoichiometric $YFe_2O_{4-\delta}$ powder is well known [18], magnetization measurements will give a fast and precise, but indirect, information about the stoichiometry of a grown crystal. magnetization measurements on single crystals are done using the PPMS, already used on powders, or the Quantum Design Magnetic Property Measurement System (MPMS) with the Reciprocating Sample Option (RSO). The MPMS uses the Faraday effect of a moving magnetic moment on conducting loops, like the PPMS VSM. But the detection coils are superconducting in the MMPS and the induced current is detected by a rf-SQUID.

2.3 SINGLE CRYSTAL X-RAY DIFFRACTION

Single crystal x-ray diffraction is used to examine the crystal structure and charge ordering. All single crystal x-ray diffraction work is done on an Agilent SuperNova diffractometer, which offers Mo and Cu x-

Name	CO (ml/min.)	CO_2 (ml/min.)	CO_2/CO	Power (%)	Feed/Seed (rounds/min.)	length (mm)
Z1	9.97	23.48	2.36	37.6	25 / 15	
Z2	7.98	23.48	2.94	38.2	20 / 10	40.0
Z3	5.98	23.48	3.93	39.2	20 / 10	35.0
Z4	17.95	46.97	2.62	40.0	23 / 11	0.0
Z5	17.95	46.97	2.62	39.8	23 / 11	
Z6	16.95	46.97	2.77	39.8	24 / 10	56.0
Z7	14.96	46.97	3.14	39.7	20 / 10	21.5
Z8	15.95	46.97	2.94	39.6	20 / 10	61.5
Z9	10.97	46.97	4.28	39.6	20 / 10	0.0

Table 2.2: Crystal growth conditions.

ray sources with micro focus, a 4-circle kappa goniometer and large area Atlas CCD detector [47].

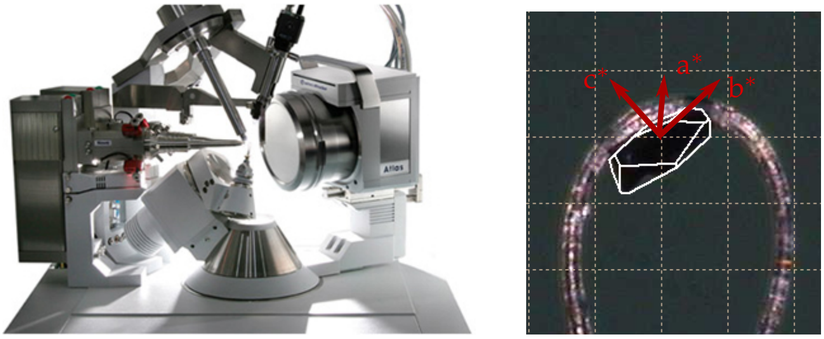

(a) SuperNova Diffractometer [47].

(b) Mounted crystal.

Figure 2.4: (a) Picture of the Agilent SuperNova Diffractometer.
(b) Single crystal on glass wire mounted on the goniometer of the SuperNova diffractometer with crystal facets used for absorption correction.

With a Cryojet a N_2 gas flow can change the sample temperature in the range of 90-490 K, and with a Helijet using gas flow of cold He_2 the temperature can be controlled down to 10 K [48, 49]. With the area detector it is possible to collect in comparable short time a complete set of all unique $hk\ell$ reflections. For absorption correction and improvement of data quality, collecting redundant data on symmetry equivalent $hk\ell$ reflections is useful. The CrysAlis$^{\text{Pro}}$ software [50] which controls the diffractometer is also used to search for a proper unit cell and after indexing to integrate the intensity of the Bragg reflections over different image frames. The absorption correction is done using indexed crystal facets. For crystal structure refinement the WinGX [51] program package including SHELX [52] is used. SIR92 [53] was found to be helpful for solving crystal structures.

Since in scattering experiments only the intensity (Equation 2.1) of reflections is measured and therefore the phase of the structure factor is unknown, it is not possible to receive the real space distribution of atoms from reciprocal images by simply applying inverse Fourier transform.

$$I(\mathbf{Q}) = |F(\mathbf{Q})|^2 = \left| \sum_j f_\alpha e^{i\mathbf{Q}(hk\ell)\mathbf{r}_j} \cdot e^{\frac{1}{3}\mathbf{Q}^2|\mathbf{U}_{ij}|^2} \right|^2 \tag{2.1}$$

Here F are the structure factors, f_α are the atomic form factors, $\mathbf{Q}$ is the scattering vector, $\mathbf{r}_j$ is the vector of the atomic positions and $\mathbf{U}_{ij}$ are the anisotropic displacement parameters. Direct methods try to solve the phase problem directly by using symmetry relayed relationships between phases and the intensity inside reflection groups. A nice introduction to the topic from Schenk can be found in [54]. SIR92 [53] uses direct methods bases on the representation theory of Giacovazzo [55, 56]. Once you have several phases one can calculate the structure factors according to Equation 2.1. By reducing the difference between these calculated squared structure factors F^2_{calc} and the observed F^2_{obs} ones, it is possible to refine the atomic positions in the model. Also the six anisotropic displacement parameters U_{ij}, describing the thermal elongation from lattice positions, are refined. In SHELX [52] this is done with minimization of χ^2 in Equation 2.2. The following equations are adopted from [11, 57].

$$\chi^2 = \sum_j \omega_{(hk\ell)} |F^2_{obs} - F^2_{calc}| \tag{2.2}$$

Here j is the summation index over all atomic positions while ω is a weighting factor as defined in Equation 2.3. The weighting factor controls how strong the impact of different reflections on the refinement is. It is mainly based on the measurement accuracy of different reflections. By reducing the weight of strong reflections, problems with the extinction correction can be accounted. While σ is the standard deviation, a and b are automatically optimized parameters ensuring an equal distribution of the variances over different intensity ranges and scattering-angles [57].

$$\omega = \frac{1}{\sigma^2(F^2_{obs}) + (a \cdot G)^2 + b \cdot G} \qquad \text{with} \qquad G = \frac{1}{3}\max(F^2_{obs}) + \frac{2}{3}F^2_{calc} \tag{2.3}$$

To judge the quality of a structural refinement residuals, so called R-values, are used.

R1 gives the difference between calculated structure factors and observed ones, the best possible value would be zero.

$$R1 = \frac{\sum_j ||F_{obs}| - |F_{calc}||}{\sum_j |F_{obs}|} \tag{2.4}$$

In contrast the weighted $\omega R2$ factor uses directly the least-squares of the structure factors, minimized during refinement. Usually the $\omega R2$ value is two or three times higher than the R1 value for the same data quality.

$$\omega R2 = \frac{\sum_j \omega (F_{obs}^2 - F_{calc}^2)^2}{\sum_j \omega_{(hkl)} (F_{obs^2})^2} \tag{2.5}$$

The goodness of fit Goof is sign of quality, for a good model and weighting scheme it should approach one. Here n is the number of reflections and p is the number of refined parameters.

$$\mathrm{Goof} = \left(\frac{\sum_j \omega_{(hk\ell)} (F_{obs}^2 - F_{calc}^2)^2}{n - p} \right)^{1/2} \tag{2.6}$$

[57]

2.4 RESONANT X-RAY DIFFRACTION

At P09 at Petra III we measured resonant x-ray diffraction at the Fe K-edge, which was not done on stoichiometric $YFe_2O_{4-\delta}$ before, and searched for anisotropy, possible caused by orbital ordering, in the x-ray polarization on superstructure reflections.

By tuning the x-ray energy to the absorption edge, resonance effects caused by virtual multipolar transitions of resonantly excited electrons, lead to a sensitivity for local electronic structure [58]. Usually the deviations of the scattering amplitude f from the non energy dependent Thompson part f_0 are small.

$$f = f_0(\mathbf{Q}) + f'(E) + if''(E) \tag{2.7}$$

At absorption edges the anomalous parts f' and f'' can become significant and are influenced by the local environment of excited electrons and therefore by charge, orbital and magnetic order. [59] These anisotropic contributions can no longer be described by scalar f' and f'' but by tensor expressions so called Templeton scattering or anisotropy of the tensor of x-ray susceptibility [58]. In the case of the iron K-edge there are 1s electrons virtually excited into 4p states, followed by a recombination of the empty hole and the excited electron. RXD on the Fe K-edge has been used by Mulders et al. to prove full charge separation into Fe^{2+} and Fe^{3+} in $LuFe_2O_4$ [60]. Through the chemical shift of the iron K-edge between different Fe valence sates, a good contrast for Fe^{2+} and Fe^{3+} charge ordering is expected.

2.4.1 *Polarization Analysis*

Figure 2.5 shows the setup used for polarization analysis.

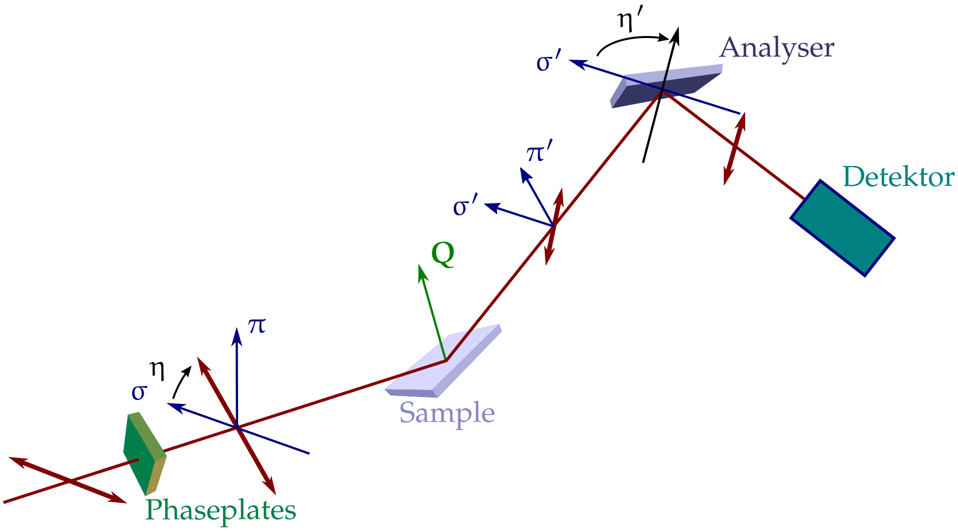

Figure 2.5: Schematic view of the diffractometer beam path in the polarization analysis setup [58].

The polarization direction of the linear polarized beam can be changed with the phase plates to an arbitrary direction. η gives the aberration of the polarization direction from σ which is perpendicular to the scattering plane. The polarization analysis follows the procedure described by Mazzoli et al. [61]. The incident polarization state can be described by the Poincaré Stokes parameters.

$$P_1 = \frac{|\epsilon_\sigma|^2 - |\epsilon_\pi|^2}{P_0'} \tag{2.8}$$

$$P_2 = 2\,\mathrm{Re}\,\frac{\epsilon_\sigma^* \epsilon_\pi^*}{P_0'} \tag{2.9}$$

$$P_3 = 2\,\mathrm{Im}\,\frac{\epsilon_\sigma^* \epsilon_\pi^*}{P_0'} \tag{2.10}$$

with the polarization vector ϵ and $P_0' = |\epsilon_\sigma|^2 + |\epsilon_\pi|^2$ [61]. For a fully polarized beam the sum of the squares of all the stokes parameters has to be unity.

$$P_1^2 + P_2^2 + P_3^2 = 1 \tag{2.11}$$

Stokes parameter P_1 is 1 for σ polarization and -1 for π polarization. While P_2 describes the situation at 45°, so $P_2 = 1$ for $\eta = 45°$ and $P_2 = -1$ for $\eta = -45°$.

The Poincaré Stokes parameters P_1', P_2' and P_3' of the scattered beam, are received by replacing ϵ with the polarization vector of the scattered beam ϵ'. For plane waves, ϵ could be replaced with the electric field amplitudes [58]. For an ideal linear polarized beam P_3 which corresponds to the circular component is zero.

The polarization is analysed using a Cu(220) analyser scattering at nearly 90°, therefore suppressing the polarization component in the scattering plane of the analyser crystal. By rotating the analyser setup including the detector, the polarization direction η' of the scattered beam can be measured. Several rocking curves of the bragg angle θ_a of the analyser crystal were recorded for different analyser angles η' and different polarization directions η of the incident beam. The rocking curves were fitted with squared Lorentzians to receive integrated intensities.

Figure 2.6 shows exemplary the rocking curve of the analyser crystal for incident polarization $\eta = 180°$ and analyser angle $\eta' = -30°$, together with such a fit, measured on a resonant feature at 7116.5 eV in the x-ray diffraction of $YFe_2O_{4-\delta}$ at 10 K.

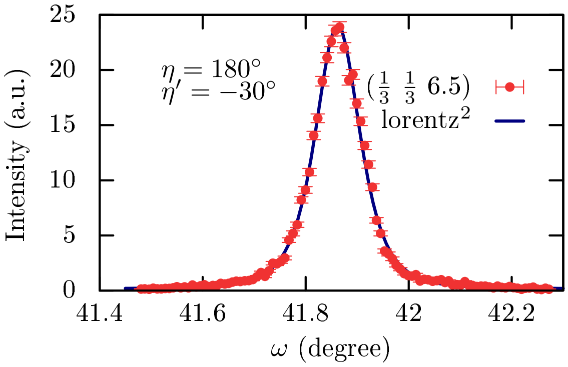

Figure 2.6: Rocking curve of the analyser crystal at 10 K at 7116.5 eV on $(\frac{1}{3}\ \frac{1}{3}\ 6.5)$ superstructure reflection.

To get the Poincaré Stokes parameters, the integrated intensities are fitted in dependency of η' with Equation 2.12.

$$I = \frac{P_0'}{2}\left[1 + P_1'(\eta)\cos(2\eta') + P_2'(\eta)\sin(2\eta')\right] \tag{2.12}$$

[61]

Taking into account the deviation from $\theta = 90°$ of the scattering angle of the Cu(220) analyser crystal, which can be found in Table 2.3, Equation 2.12 changes to Equation 2.13, which is used for fitting. All the fitting of the polarization analysis is mainly based on Matlab scripts written by Dr. Dinesh Kumar Shukla, Instrument scientist at P09.

$$I = \frac{P_0'}{2}\left[1 + \cos(2\theta_a)^2 + \sin(2\theta_a)^2\left(P_1'\cos(2\eta') + P_2'\sin(2\eta')\right)\right] \tag{2.13}$$

The resulting intensities were fitted in dependency of η' for all different incident polarizations η with Equation 2.13. Figure 2.7 shows exemplary the fit for $\eta = 75°$.

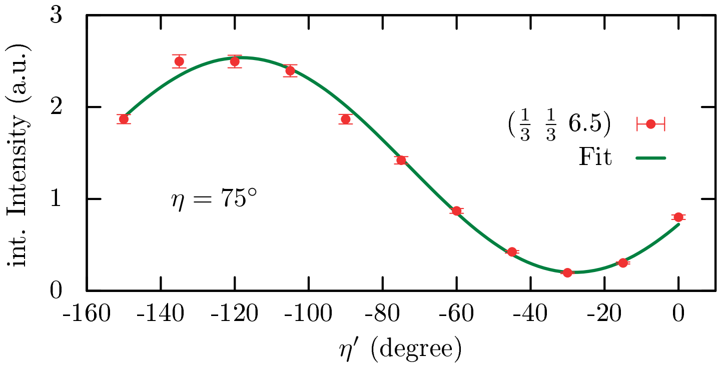

Figure 2.7: Fit of Equation 2.13 to the integrated intensities for incident polarization angle $\eta = 75°$.

The variation of the Poincaré Stokes parameter in an ideal Thompson scattering process can be expressed by Equations 2.14–2.16, with $x = \cos(2\theta)$ [62].

$$P_1' = \frac{1 - x^2 + P_1(1 + x^2)}{1 - x^2 + P_1(1 - x^2)} \tag{2.14}$$

$$P_2' = \frac{2P_2x}{1 - x^2 + P_1(1 - x^2)} \tag{2.15}$$

$$P_3' = \frac{2P_3x}{1 - x^2 + P_1(1 - x^2)} \tag{2.16}$$

Reflection	$(\frac{1}{3}, \frac{1}{3}, 6.5)$		$(\frac{1}{2}, \frac{1}{2}, 10.75)$	
Energy (eV)	7116.5	7130	7117.5	7125.5
θ (degree)	85.794	85.685	85.876	85.686

Table 2.3: Scattering angles of the analyser crystal for the reflections and energies on which polarization analysis was performed.

Obviously P_3' can not be received from this fit, in case of a fully polarized beam and perfect analysis it could be calculated from the sum of $P_1'^2$, $P_2'^2$ and $P_3'^2$, which has to be unity.

2.4.2 *The P09 beamline*

Figure 2.8 gives an overview of the P09 beamline at Petra III at HASYLAB from the undulator to the first experimental hutch, which contains the high precise Psi-diffractometer with open Chi-circle.

The high heat load monochromator uses either Si(111) or Si(311) crystal pairs and offers an energy range from 2.7 keV to 24 keV. The polarization of the linear polarized beam is 99.98 %. The polarization direction is changeable using a double phase retarder. The setup offers a photon flux at the sample of 10^{13} photons/sec at 10 keV. The

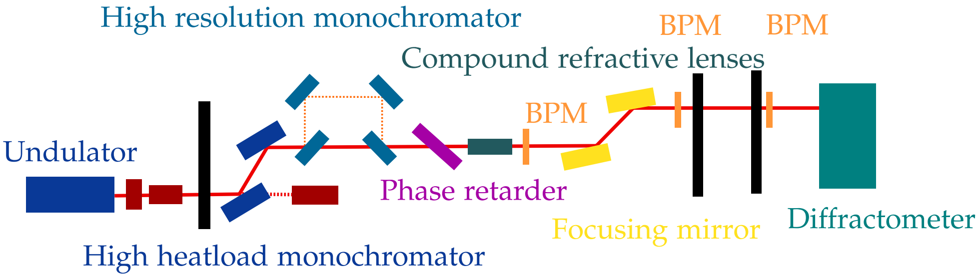

Figure 2.8: Schematic view of the P09 beamline at Petra III [63].

temperature at the sample can be controlled by a displex cryostat in a range of 4–450 K. As detector there were an avalanche-photodiode point detector and for fluorescence a VORTEX Si-drift diode available.

2.5 POLARIZED NEUTRON DIFFRACTION AT DNS

At DNS we examined diffuse magnetic scattering on highly stoichiometric $YFe_2O_{4-\delta}$ single crystals above the Néel-temperature. We further investigated the temperature dependency of the 3D magnetic ordering below the Néel-Temperature. Furthermore, we used polarization analysis to determine the moment direction both below and above the Néel-Temperature.

2.5.1 *The DNS instrument*

DNS is a cold neutron diffractometer from JCNS at FRM II with the capability of polarization analysis [64]. We use the large detectorarea of DNS for fast reciprocal space mapping, of the $hh\ell$-plane and polarization analysis to determine the origin of different scattering contributions.

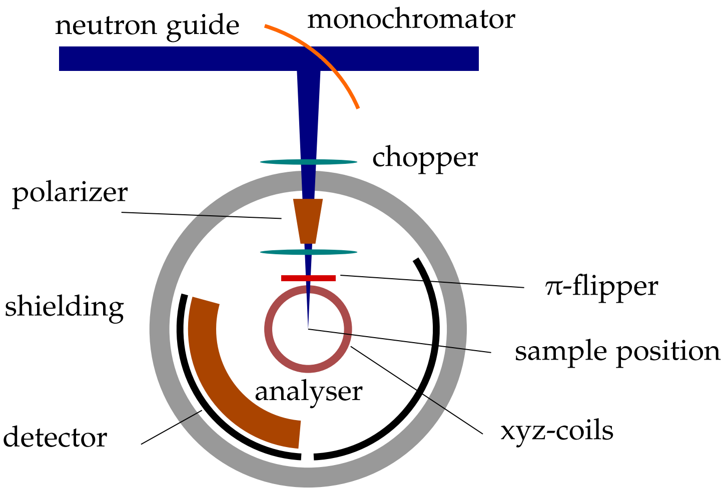

Figure 2.9: Schematic view of the DNS-instrument. [65]

A schematic view of the instrument in given in Fig. 2.9. The neutrons are transported from the cold source though the NL6a neutron guide to the PG(002)-monochromator. The monochromatized beam, with a wavelength of 4.2 Å is polarized by supermirror benders and the neutrons are further on guided by a weak magnetic field, to preserve the polarization. To inverse the direction of the neutron spin quantization, on demand, a π-flipper is seeded in the beam-path. An electric current applied to the coil, of which the π-flipper consists, generates a magnetic field. A neutron in a magnetic field perpendicular to its polarization direction will start to precess. The coil has a length, that a neutron passing the coil with a fixed velocity will exactly reverse the sign of its polarization due to the Larmor precession. [65]

Around the sample a set of Helmholtz-coils is placed, which offers the possibility to apply a small guide field ($< 10\,\mathrm{Oe}$) in an arbitrary direction, and therefore orient the neutron polarization to a desired direction. After the neutrons are scattered, they are also transported using a weak guide-field to preserve spin orientation. Before they reach the detector their polarization is analysed again using supermirror benders.

2.5.2 *Experimental set-up*

Our first experiment on DNS was placed in December 2011 where we had some overtime on an experiment dedicated to diffuse scattering in Magnetite. Our plan was to map the reciprocal $hh\ell$-plane at different temperatures, belonging to different macroscopic magnetization regions and charge ordered structures observed in x-ray diffraction. We focused on the $hh\ell$-plane because magnetic ordering in $LuFe_2O_4$ is present around the $(^1/_3\ ^1/_3\ l)$-line [66]. A 52 mg $YFe_2O_{4-\delta}$ crystal from growth No. 8 (sample name Z8G5_S1) of good stoichiometry, as show in Figure 3.14 in Section 3.1.2.1 , was prealigned by Jörg Perßon using x-ray Laue-diffraction. The c-axis was defined clearly but there were some uncertainties in determination of the [110]-direction. The sample was therefore fully aligned on the four circle diffractometer. The DNS instrument offers only sample movement in the ω-direction. For obtaining $hh\ell$-maps the sample was oriented that the c-axis and the [110]-axis build the horizontal scattering plane (Fig. 2.10). By rotating around ω it is, with the additional 2-θ-degree-of-freedom from the detector position, possible to scan the whole $hh\ell$-plane. After mounting the sample on the aluminium sample holder, the orientation was fine tuned by bending the holder and controlling the orientation with x-ray Laue-diffraction which was done by Susanne Mayr from the TUM.

To distinguish between magnetic and non magnetic scattering contributions, spin-flip and non-spin-flip measurements with magnetic

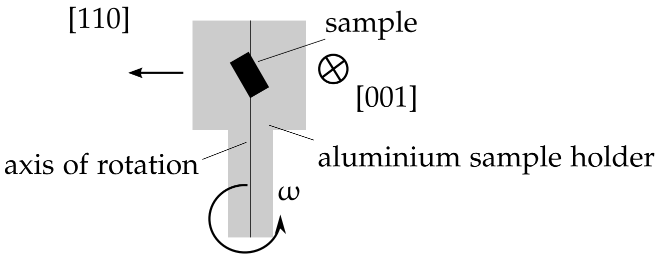

Figure 2.10: Sample holder and sample orientation in the DNS set-up.

field parallel z-direction were performed. The different field directions are shown in Fig. 2.11.

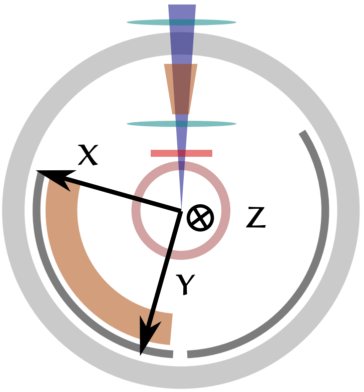

Figure 2.11: Field directions at DNS.

Z-field means a field in vertical direction perpendicular to the horizontal scattering plane. The x-direction is facing the end of the detector array and is parallel to the average $\bar{\mathbf{Q}}$. The y-axis is defined as being perpendicular to x and z.

With aligning the neutron polarization $\mathbf{P}$ parallel to z, $\mathbf{P}$ is always perpendicular $\mathbf{Q}$. As described in [65] only the component of $\mathbf{M} \perp \mathbf{Q}$ contributes to the scattering cross-section and $\mathbf{M}_x^{\perp \mathbf{Q}} = 0$ because $x \parallel \bar{\mathbf{Q}}$.

In approximation $\mathbf{P} \parallel z$ and $\mathbf{P} \perp \bar{\mathbf{Q}}$ leads to the following rules:

$$\mathbf{M}^{\perp \mathbf{Q}} \perp \mathbf{P} \text{ leads to SF-scattering} \tag{2.17}$$

$$\mathbf{M}^{\perp \mathbf{Q}} \parallel \mathbf{P} \text{ leads to NSF-scattering} \tag{2.18}$$

With the sample orientation given like in Fig. 2.10, contributions in the SF-channel are from $\mathbf{M}^{\perp \mathbf{Q}}$ parallel to a linear combination of [001] and [110]. As $YFe_2O_{4-\delta}$ is supposed to be an Ising-spin-system with $\mathbf{c}$ as the easy axis, magnetic scattering contributions are most likely from magnetic moments parallel $\mathbf{c}$. To exclude an in-plane spin moment in the a-b-plane, we used and field in x-direction in a later DNS experiment.

With the neutron polarization $\mathbf{P}$ parallel to x, which is roughly parallel to the average scattering vector $\bar{\mathbf{Q}}$, all magnetic scattering regardless of the direction of the magnetic moment will be spin-flip, because

$$\mathbf{M} \perp \mathbf{Q} \quad \text{predicts} \quad \mathbf{M} \perp \mathbf{P} \quad \text{since} \quad P \parallel \bar{Q} \quad . \tag{2.19}$$

Fig. 2.12 gives a overview about the temperatures at which a $hh\ell$-maps were collected, green lines correspond to experiments from the December beamtime, all those were measured on cooling.

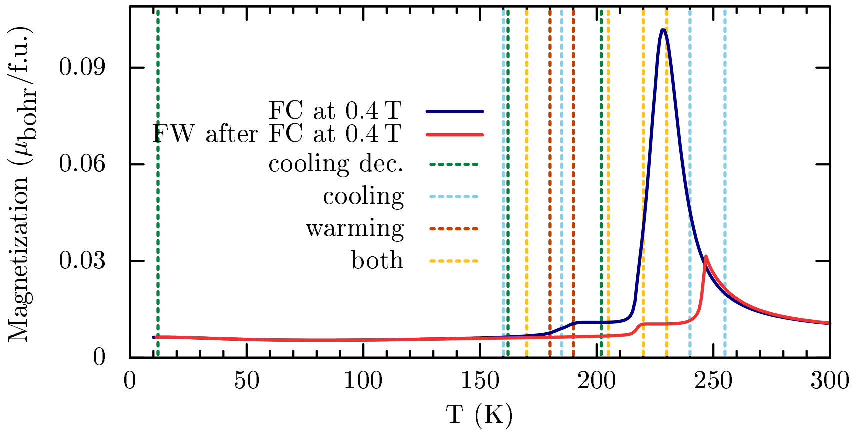

Figure 2.12: Magnetization of sample Z8G5_S1, green curve is measured during cooling in a field of 0.4 T; red curve on warming in the same field. The dotted lines mark temperatures at which a $hh\ell$-map was collected at DNS.

To obtain a microscopic confirmation of the thermal hysteresis of the magnetic phase transitions, we performed measurements on cooling (dotted blue line in Fig. 2.12) and warming (dotted brown line). At yellow lines on both cycles an experiment was done.

All DNS images have been corrected for the detector efficiency using background measurement of an empty sample holder and a standard sample of the nuclear incoherent scatter Vanadium [67]. The imperfect flipping ratio was not corrected. The noise which was created by using NiCr-data for flipping-ratio correction, vitiates the advantages. The overall degree of polarization at the DNS instrument of $0.88 \leqslant P \leqslant 0.92$ was measured in [68], this includes imperfect flipping ratio and non full polarization of the primary beam which is the majority contribution.

To obtain a better resolution different detector bank positions are measured. The idea behind this method is to vary the detector-area, especially the overlap between different detectors, connected to a specific scattering angle, and therefore reduce the influence of detector width and death area on the detector resolution. After the measurement the values of the $hh\ell$-map are received from interpolated counts from different detector bank positions.

2.5.3 *Second beamtime*

The main task for the second beamtime was to collect data on the diffuse scattering. We also investigated if the magnetic moment is aligned along $[001]$, by measuring in a field in x-direction. Further on we examined the temperature dependence described in Fig. 2.12. For the second DNS experiment the same sample was used, unfortunately the orientation of the sample from the previous experiment was lost and a 8 mg part was broken off during demounting. The sample was again aligned using Laue diffraction in the same set-up as shown in Fig. 2.10, but the in plane direction specified as [110] could be one of the symmetry equivalent axes $[\bar{2}\ \ 1\ \ 0]$ or $[1\ \ \bar{2}\ \ 0]$ (this has to be taken into account when comparing measurements from both experiments).

3 RESULTS

3.1 STOICHIOMETRIC SINGLE CRYSTALS

3.1.1 *Single phase polycrystalline $YFe_2O_{4-\delta}$*

Single phase polycrystalline $YFe_2O_{4-\delta}$ is the first step in the crystal growth process.

3.1.1.1 *Powder x-ray diffraction results*

The $YFe_2O_{4-\delta}$ powder synthesized with different oxygen deficits by the solid states reaction described in Section 2.1.1, is checked for foreign phases by x-ray diffraction.

Figure 3.1 shows a typical powder diffractogram of $YFe_2O_{4-\delta}$. The easiest way to check the material for foreign phases is to compare the diffractogram with a published ICSD-data [69].

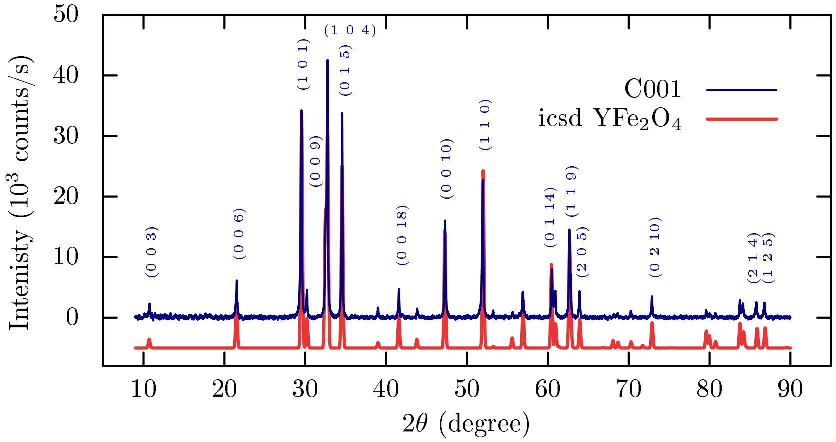

Figure 3.1: Powder x-ray diffractogram of C001 compared to the ICSD-Data of $YFe_2O_{4-\delta}$ from [32]. (C001-Data is corrected for background. ICSD Data is shifted and scaled for clarity.)

In Figure 3.1 there is no foreign phase observable. The huge background originating from Fe-fluorescence, which is near to the Cu K_α wavelength [70], was subtracted from the shown data (Raw-data without background subtraction and excluded primary beam can be found in App. A.1.). Using Mo-wavelength to avoid the Fe-fluorescence was tried, but found unserviceable due to the lower **Q**-resolution, which did not allow to resolve all peaks, and also due to lower intensity and strong contribution of the primary beam caused by non optimal instrumental alignment.

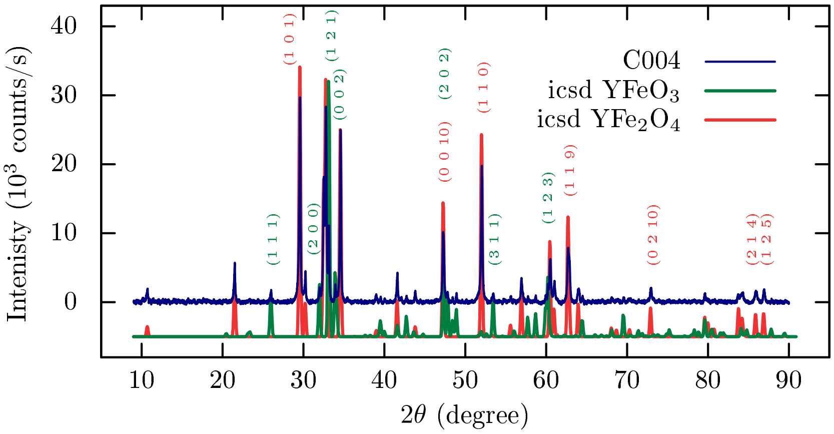

Figure 3.2: Powder x-ray diffractogram of C004 compared to the ICSD-Data of $YFe_2O_{4-\delta}$ from [32] and $YFeO_3$ from [71]. (C004-Data is corrected for background. ICSD Data is shifted and scaled for clarity.)

Figure 3.2 shows the diffractogram of sample C004 which contains contributions from foreign phase contaminations. By comparison with the ICSD-Data for the possible contamination candidates from the phase diagram (Fig. 1.4), one can conclude that the foreign phase is $YFeO_3$. At the surface between the aluminium oxide boat and the synthesis material, there is always Fe_2O_3 present, which might be caused by a catalytic effect of the aluminium oxide. This material is mechanically removed, before further studies, which can easily be done due to its red colour compared to the black $YFe_2O_{4-\delta}$. Beside this $YFeO_3$ is found to be the most common foreign phase, indicating too high oxygen partial pressure, this is in accordance with [14]. Since $YFeO_3$ is a weak ferromagnet and $Y_3Fe_5O_{12}$ a ferrimagnet at room temperature small amounts of both can also be detected in magnetometry. Magnetite, which is a common foreign phase in $LuFe_2O_4$ [11], is unlikely to occur regarding to the phase diagram of $YFe_2O_{4-\delta}$. In a few samples a kink at the characteristic Verwey [72] transition at 120 K was observed in magnetization. This might be induced through surface oxidation of the sample, which can take part while removing a warm sample from the controlled atmosphere in the tube furnace. With less oxygen partial pressure metallic iron occurs in the synthesized material.

The lattice parameters of $YFe_2O_{4-\delta}$ in the hexagonal representation of $R\bar{3}m$ for all different samples from Table 2.1 can be found in Appendix A.2. Figure 3.3 shows both lattice constants in dependence of the gas-mixture used during synthesis. There is a clear tendency for the in plane lattice constants a and b to be smaller with increasing off stoichiometry, i. e. a larger δ in $YFe_2O_{4-\delta}$ which corresponds to a smaller CO_2/H_2-ratio and therefore lower oxygen partial pressure. The out-of-plane lattice constant c possess a strong increase from $CO_2/H_2 = 1.5$ to 3.0, followed by an almost constant behaviour between $CO_2/H_2 = 3$ to 5.5. The strong increase to $CO_2/H_2 = 3.0$ is connected to the change in the magnetic transition temperatures, as shown in Figure 3.11. The a/b lattice constants for the samples with the best oxygen partial pressures fit well with the one observed by Inazumi et al. [18]. But they did not observe an influence of the off-stoichiometry δ on the a/b lattice constants between $\delta = 0.00$ and $\delta = 0.095$ at room temperature. The increase of the c lattice constant with lower off-stoichiometry δ was also observed in [18], while the reported c lattice constants are up to 0.01 Å larger than our highest one. This indicates some systematic error in the absolute lattice constants either in [18] or in our measurement. Since the c-lattice constants reported in [32] are also higher and our lowest a-lattice constant corresponds to the a constant in [18] and [32], it is assumed that there is some systematic error in our instrument, leading to slightly too small lattice constants. However, relative values of lattice constants are trustworthy and the unit cell volume decreases with larger oxygen content, like it is expected from [73, 74] and is also observed in $LuFe_2O_4$ [75, 76].

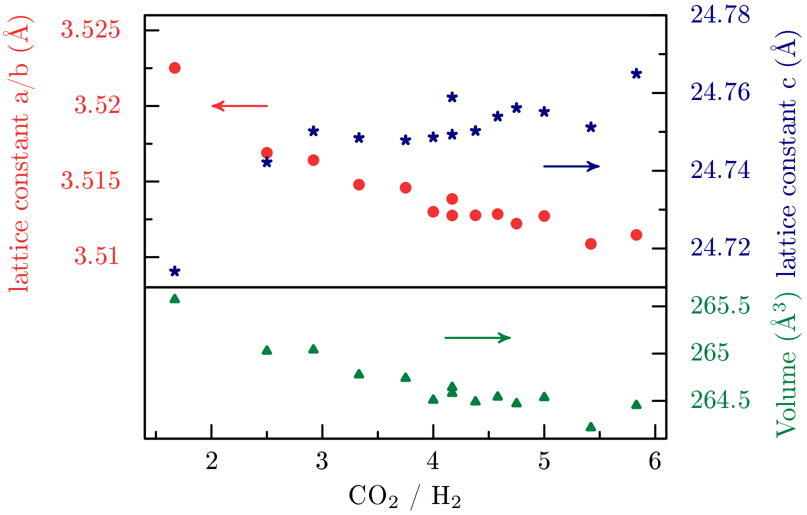

Figure 3.3: Dependence of the hexagonal lattice constants and the unit cell volume of $YFe_2O_{4-\delta}$ from CO_2/H_2-gas-mixture-ratio during synthesis. Higher ratio corresponds to smaller δ.

3.1.1.2 *Magnetometry*

Magnetization measurements on powdered samples are done to achieve an indirect indication for stoichiometry. The question how stoichiometry influences the occurrence and the temperatures of magnetic transitions was already targeted in [18]. Since the oxygen vacancy is not measured during this thesis, comparison with [18] is our standard method for sample quality control.

The magnetic behaviour of the powder samples can roughly be divided into four different kinds.

- no peak, broad rise to lower temperatures and no thermal hysteresis
- non-stoichiometric behaviour with one broad peak with thermal hysteresis between warming and cooling
- stoichiometric behaviour with two step transition with thermal hysteresis
- two step transition with ferromagnetic contamination

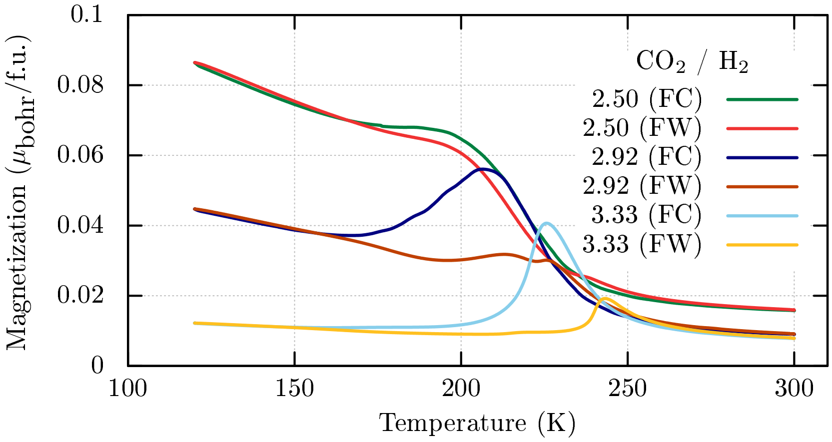

Figure 3.4: Magnetization during field cooling and field warming at 3970 Oe for the calcinations C001 (CO_2/H_2 = 2.5), C012 (CO_2/H_2 = 2.92) and C002 (CO_2/H_2 = 3.33).

Figure 3.4 shows the magnetization for the samples grown under low oxygen concentration. $C001_{U=2.5}$ shows only a broad rise to lower temperatures with a broad maximum around 200 K, it obeys no thermal hysteresis between field-warming and field-cooling. All magnetization curves with higher ratio U of CO_2 to H_2, i. e. oxygen partial pressure, inhibit a huge thermal hysteresis. The magnetization of $C001_{U=2.5}$ has the same transition temperature as the sample Inazumi specified with an oxygen deficit of $\delta = 0.095$ [18] in $YFe_2O_{4-\delta}$. The magnetization curve from C017 which was synthesised at a CO_2 to H_2 ratio of 1.67, which is the lowest used ratio, can be found in App. A.4. The magnetization curve of $C012_{U=2.92}$ shows some ripple, especially around the maximum in the heating curve. This is most likely due to multiple phases and not an intrinsic two step phase transition, since both $C001_{U=2.5}$ and $C002_{U=3.33}$ do not show this features.

Samples C006$_{U=3.75}$ and C015$_{U=4.00}$ are from the same type as C002$_{U=3.33}$ showing a huge thermal hysteresis and only moderate rising to lower temperatures, the curves can both be found in App. A.3.

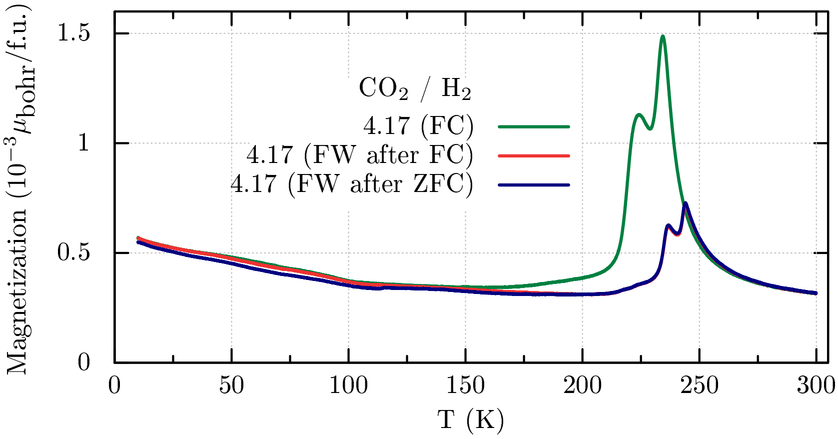

Figure 3.5: Magnetization during field cooling, following field warming and field warming after zero field cooling at 100 Oe for the calcination C003 (CO_2/H_2 = 4.17) at a cooling rate of 1.5 K/min.

Figure 3.5 shows the field cooling, field warming after FC and field warming behaviour after zero field cooling of sample C003$_{U=4.17}$, at 100 Oe. The sample clearly shows two maxima and almost no influence of a previously applied cooling field, which is characteristic for stoichiometric $YFe_2O_{4-\delta}$. The shape of the two maxima with almost equal heights differs from that observed in [18]. Since C003$_{U=4.17}$ consists of two different starting materials (Tab. 2.1) there was the possibility that this behaviour is induced through multiple phases and is not the intrinsic two step phase transition of stoichiometric $YFe_2O_{4-\delta}$.

The small buckle around 120 K is probably a small magnetite contamination, since it is in the region of the Verwey transition.

To exclude this possibility, C016$_{U=4.17}$ was synthesised under the same conditions starting from stoichiometric mixture of Ye_2O_3 and Fe_2O_3. magnetization for C016$_{U=4.17}$ is shown in Fig. 3.6.

Since the two step character of the magnetization in Fig. 3.6 is similar to that observed in [18], the two equal maxima in Fig. 3.5 are caused by the mixed starting materials. Therefore for $YFe_2O_{4-\delta}$ it is not recommended to recycle calcined powders, which has been found convenient for $LuFe_2O_4$ [77]. The difference between FW after ZFC and FW after FC in Fig. 3.6 indicates slightly off-stoichiometry of sample C016. While the shifting of the higher temperature transition peak in FW away from the FC curve to higher temperatures is caused by the cooling rate of 4 K/min. The sample temperature differs from the measured temperature of its environment, which is shifted in direction of the temperature increase or decrease. Such in-

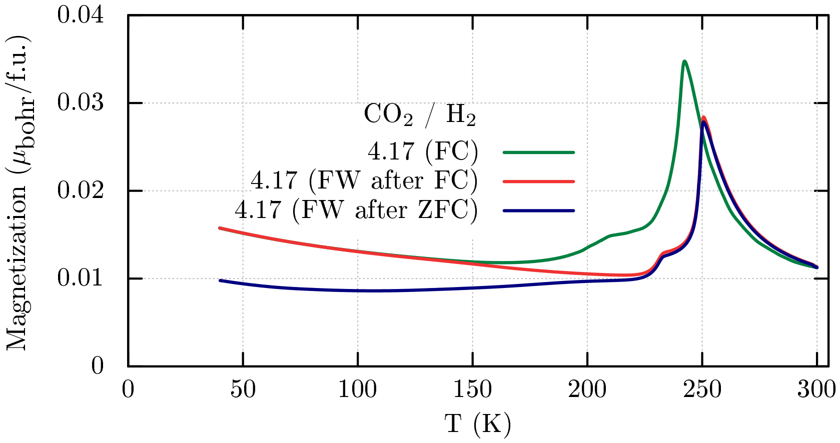

Figure 3.6: Magnetization during field cooling and field warming at 3970 Oe for the calcination C016 (CO_2/H_2 = 4.17) at a cooling rate of 4 K/min.

fluence is much smaller for slower cooling rates like in Fig. 3.5, where the cooling rate is 1.5 K/min.

The samples $C014_{U=4.38}$, $C008_{U=4.58}$, $C013_{U=4.75}$, $C005_{U=5.00}$ and $C009_{U=4.42}$ show all magnetic behaviour (see App. A.5) from the same type as $C016_{U=4.17}$ Fig. 3.6., but the two step character is not so clear. Only sample $C005_{U=5.00}$ Fig. A.7 is remarkable, because it shows a comparable magnetization with two maxima like Fig. 3.5, but the higher temperature maxima is the one with lower magnetization now. $C005_{U=5.00}$ was synthesized from Fe_2O_3 and Ye_2O_3 therefore the theory of multiple phase contamination through different starting materials is inapplicable. But besides all other samples $C005_{U=5.00}$ was inserted into a cold tube furnace (see Tab. 2.1). Due to this, the material will pass slowly different phases which might lead to multiple phases in the final material. Therefore the sample should not only be quenched at the end of the synthesis, but also inserted into a hot tube furnace at the beginning.

Increasing the oxygen partial pressure further will lead to contamination with $YFeO_3$ and FeO from which the first one gives a ferromagnetic contribution, which is clearly observed in magnetization (Fig. 3.7).

As conclusion we can give in Tab. 3.1 a range for the gas mixture which will lead to a two-step transition $YFe_2O_{4-\delta}$ without observable foreign materials, .

	lower border	optimum	upper border
CO_2/H_2	4.00	4.17	5.00

Table 3.1: Conditions found suitable for calcination of single phase $YFe_2O_{4-\delta}$ with two step magnetic transition.

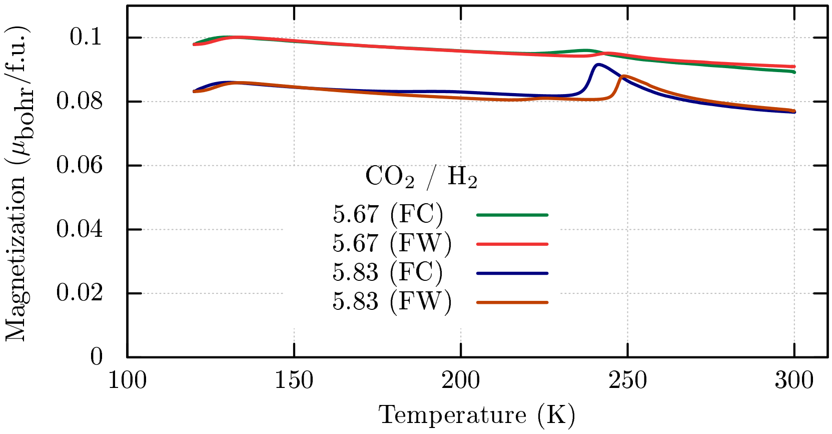

Figure 3.7: Magnetization during field cooling and field warming at 3970 Oe for the calcinations C011 (CO_2/H_2 = 5.67) and C004 (CO_2/H_2 = 5.83).

High field magnetization for sample $C003_{U=4.17}$ is given in Fig. 3.8, this was done on C003 because it was the best sample at this time. Also thermoremanent magnetization (TRM) after 9 T field cooling is shown.

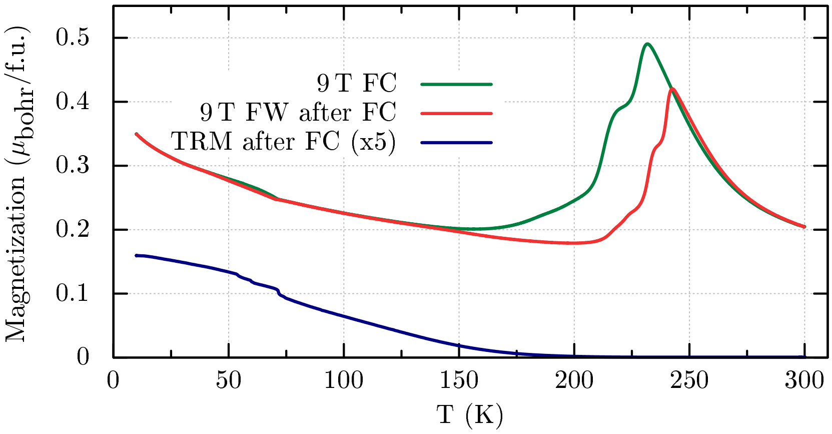

Figure 3.8: Magnetization during field cooling (1.5 K/min.) and following field warming (1.5 K/min.) at 9 T, also thermoremanent magnetization (1.5 K/min.) after 9 T field cooling (20 K/min.) for sample C003 (CO_2/H_2 = 4.17).

The curve is mostly a broader version of Fig. 3.5, the only difference is the small buckle at 70 K, which is also present in thermoremanent magnetization and the absence of the 120 K kink. The buckle at 70 K might be the same feature as the 120 K kink in Fig. 3.5 with a field induced shift of the transition temperature.

To exclude the possibility of sample contamination the measurement was repeated on sample C008 (Fig. 3.9).

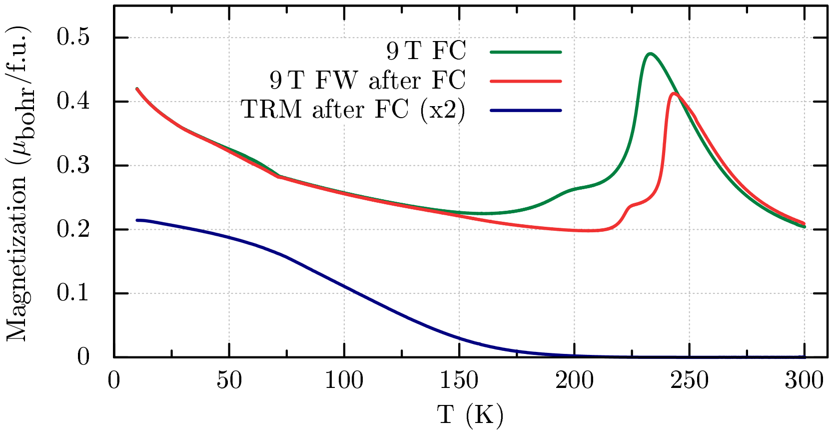

Figure 3.9: Magnetization during field cooling (1.5 K/min.) and following field warming (1.5 K/min.) at 9 T, also thermoremanent magnetization (1.5 K/min.) after 9 T field cooling (20 K/min.) for sample C008 (CO_2/H_2 = 4.58) — TRM is scaled by a factor of 5.

C008 shows the same buckle at 70 K. The low temperature magnetization at 100 Oe (Fig. 3.10) shows also a large step at 120 K.

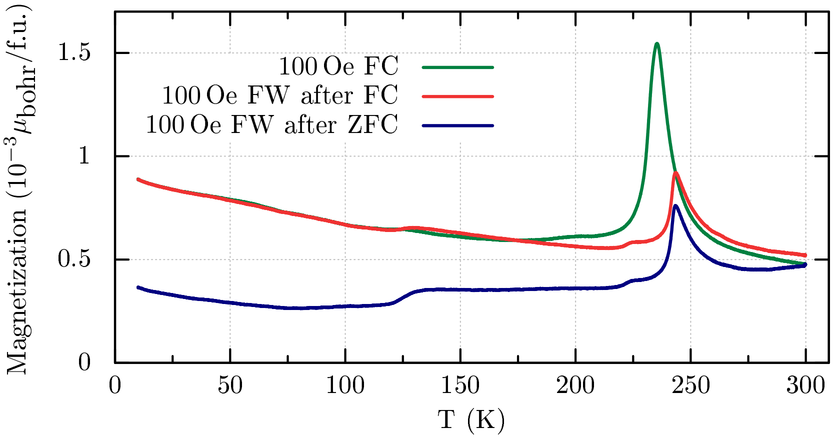

Figure 3.10: Magnetization during field cooling (1.5 K/min.) and following field warming (1.5 K/min.) at 100 Oe also field warming at 100 Oe (1.5 K/min.) after zero field cooling (20 K/min.) for sample C008 (CO_2/H_2 = 4.58).

The most interesting observation in Fig. 3.10 is that the FW after ZFC curve is much smaller that FW after FC. This is most likely caused by some ferromagnetic contribution, which encourages the thesis of a contamination with magnetite, although magnetite seems unlikely to occur in the syntheses process regarding to the phase diagram. Fe_2O_3 and $YFeO_3$ should participate before there would be some magnetite contribution. The difference between ZFC and FW after FC could also be explained by slightly off stoichiometry like described in [18].

The influence of the oxygen partial pressure, i. e. the mixing ratio of CO_2 and H_2 during growth, on the position of the higher temperature peak is analysed in Fig. 3.11.

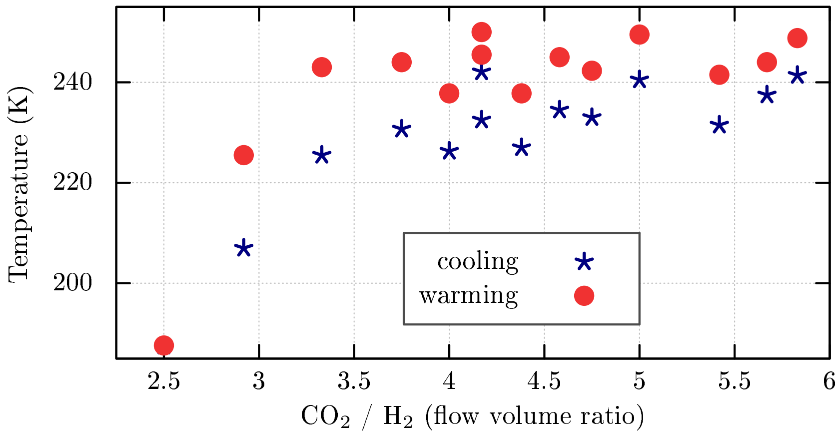

Figure 3.11: Analysis of the higher transition temperature (peak position) under the influence of varying CO_2 to H_2 ratio. Measured in a magnetic field of 3970 Oe.

Besides the step from a broad peak for a non-stoichiometric sample to a two step transition in stoichiometric sample, there is no change in the transition temperature above statistical fluctuations, observable. Fig. 3.11 gives also a nice overview about the thermal hysteresis of the magnetization.

3.1.2 *Crystal growth*

Several crystals were grown under different low oxygen partial pressure, as listed in Table 2.2.

Fig. 3.12 shows a picture of the seed rod after growth Z6. Only the shiny part consist of crystalline $YFe_2O_{4-\delta}$, the decomposed material is mostly FeO and $YFeO_3$. During growth while the seed rod moves downwards, the rod cools. $YFe_2O_{4-\delta}$ is absent in the phasediagram at 1100 °C (Fig: 1.5). During cooling, the Crystal has to pass this temperature region, which leads to this partial decomposition of $YFe_2O_{4-\delta}$ to FeO and $YFeO_3$ as described in [14].

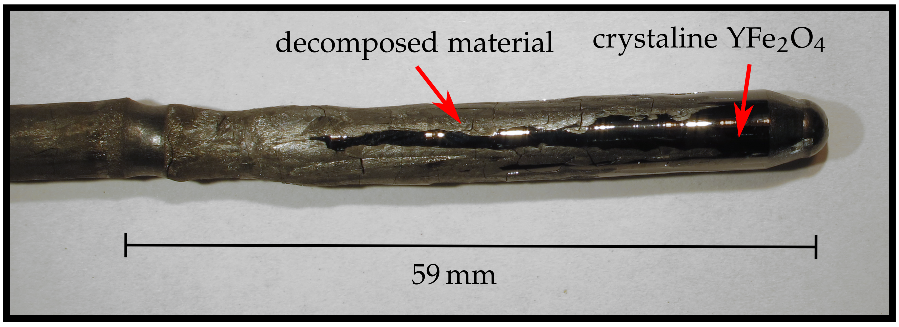

Figure 3.12: Photograph of growth Z6.

Crystals with big facets, i. e. large flat surfaces, are separated for further investigations. $YFe_2O_{4-\delta}$ does not prefer to split at c-facets building small a-b-plates, unlike $LuFe_2O_4$ [11], which is surprising since it has the same hexagonal layered structure with a large c-axis. Crystalline $YFe_2O_{4-\delta}$ which shows smooth shiny black surfaces, can be easily distinguished from the decomposed polycrystalline material by optical microscopy.

Samples are named after the following scheme Z00G11S22 where 00 is the number of the growth from Tab. 2.2. G11 describes the position on the seed rod, starting from G1 for the last grown part up to G∞ for the lowest part of the seed rod. The number following S is a consecutive number for different crystals from the same crushed rod slice.

3.1.2.1 *Magnetometry*

Like for powder, magnetic behaviour will give a fast precise, but indirect, information about the stoichiometry of a grown crystal.

Magnetic behaviour of $YFe_2O_{4-\delta}$ single crystals, with a field applied parallel to hexagonal **c** axis, can be distinct in three different kind of samples.

1. The magnetization of **Type A** non-stoichiometric samples shows a broad glassy transition peak slightly below 200 K,. In field cooling it is followed by a broad rise to lower temperatures.

There is no thermal hysteresis between field cooling and field warming after field cooling observable. In contrast to the field warming curve after cooling in zero field, which is much lower at temperatures below the transition. Figure 3.13 shows the magnetization of sample Z5G2 which is Type A. The behaviour is comparable to non-stoichiometric powder samples, and the oxygen off-stoichiometry could be estimated from [18] to be larger than $\delta = 0.05$. The behaviour is similar to that of non-stoichiometric $LuFe_2O_4$ which shows the same huge differences between field warming after FC and after ZFC. And a broad glassy transition at slightly higher temperature as in $YFe_2O_{4-\delta}$. [78, 79] The $YFe_2O_{4-\delta}$ crystals grown by Shindo et al. [14] are also identified as Type A by magnetization measurements of Sugihara et al. [15]. The weak ferromagnetic moment below 200 K was called "induced parasitic ferrimagnetism" [15] and is strongly anisotropic. Sugihara et al. [15] found non-stoichiometric $YFe_2O_{4-\delta}$ be a good example for an Ising spin system, since this behaviour is only observed in magnetization measurements with field applied parallel to the hexagonal **c** axis, making this the easy axis. The magnetic moment is thought to be induced by preferential occupation of Fe^{2+} and Fe^{3+} on two antiferromagnetic ordered sublattices [15].

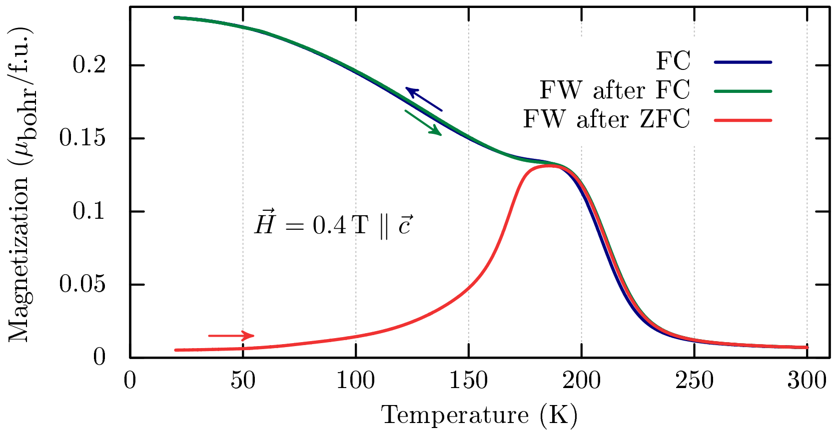

Figure 3.13: Magnetization of sample Z5G2 of NS-type. The red curve is measured during field warming (FW) at $H = 0.4\,T$ after cooling without field, the green curve during FW after cooling in a 0.4 T field and the blue curve is field cooling (FC).

2. **Type B** is considered to be stoichiometric. It shows a two step transition in field cooling and in field warming after field cooling as after zero field cooling. Both transitions show a huge thermal hysteresis of 20 K between field warming and field cooling. The higher transition peak, which is sharp, is at $T_h^w = 248\,K$ on warming and $T_h^c = 228\,K$ on cooling. While the lower transition,

which is a broad dip in magnetization, lays at $T_l^w = 215\,K$ on warming and $T_l^c = 185\,K$ on cooling. There is no difference observable between field warming after zero field cooling or after field cooling. Which is totally different to type A samples.

Figure 3.14 shows the magnetization of sample Z8G5_S1 which is comparable to the polycrystalline sample identified by Inazumi et al. with an oxygen deficit of $\delta = 0.00$ [18]. $\delta = 0.03$ is the upper limit of the oxygen deficit, since the powder sample with this oxygen deficit shows parasitic ferrimagnetism at lower temperatures in [18], which is not observed in our crystal. This is the first observation of such antiferromagnetic two step transition in $YFe_2O_{4-\delta}$ single crystals. The sample is considered to be stoichiometric and of Type B.

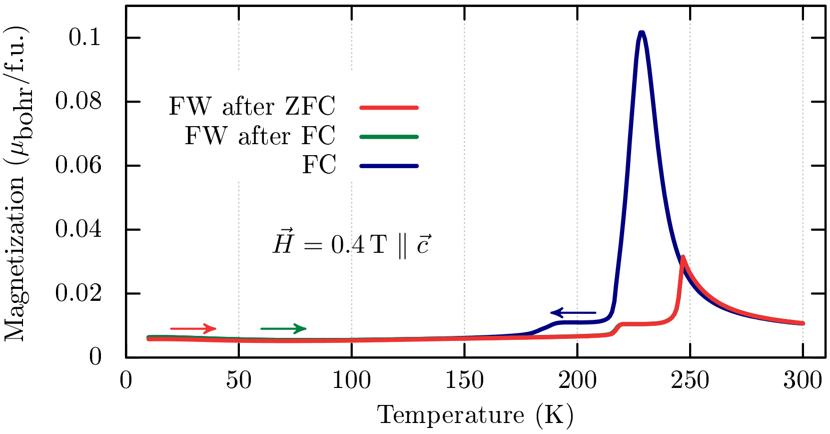

Figure 3.14: Magnetization of sample Z8G5real_S1 of Type B. The red curve is measured during field warming (FW) at $H = 0.4\,T$ after cooling without field, the green curve during FW after cooling in a 0.4 T field and the blue curve is field cooling (FC).

3. **Type C** sample show all the properties of stoichiometric samples of Type B with an additional transition at 60 K which is only present in field warming. Somewhat similar behaviour in a much stronger matter was found in $LuFe_2O_4$ at much higher temperatures and called "anomalous field-heating-effect" [80]. In $YFe_2O_{4-\delta}$ this behaviour was never reported before and in this thesis it was only observed in samples from one growth. This type of stoichiometric single crystals was obtained during growth six with a lower (than during growth eight) oxygen partial pressure. Figure 3.15 shows the magnetization of the sample Z6G2_S6 which shows stoichiometric behaviour but also the additional transition peak around 60 K during warming. The curve is noisy because of the small sample size. The magnetization rises much stronger at lower temperatures than in Figure 3.14, which might indicate slightly off-stoichiometry or a small con-

tamination with foreign ferromagnetic material. The behaviour is similar to that of the powder sample with $\delta = 0.03$ in [18]. Whether the additional peak is intrinsic, is at least questionable.

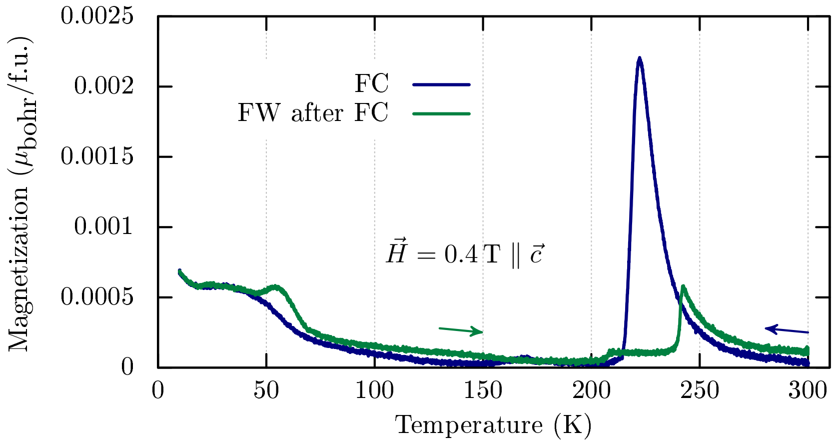

Figure 3.15: Magnetization of sample Z6G2_S6 of SB-type. The green curve is measured during field warming (FW) at $H = 0.4\,\mathrm{T}$ after cooling in the same field and the blue curve during field cooling (FC).

The raise of the magnetization to lower temperatures, the height of the background and the width of the higher transition peak, can be used to further distinguish different qualities of the latter two types. Best samples have no raise, low background and a sharp transition peak.

Figure 3.16 shows the low temperature region of Figure 3.14 in higher resolution, which shows two additional transitions, one around 80 K characterised by a reversion of the slope of the magnetization and the second identified by a local maximum at 18 K. The absolute change in the magnetization is very small compared to the transition peak at the Néel temperature. This might be the same kind of transition observed in Type C samples. The fact that it is extremely weak in Type B samples, further encourages the theory of a non intrinsic effect.

Figure 3.17 and 3.18 show the field dependence of the magnetization for the stoichiometric sample Z2GinfS3, which shows temperature dependent magnetization (Fig. A.9) of Type B. Away from the transition temperatures, the filed dependence is strictly linear (Fig. 3.17). The magnetization shows no saturation up to 7 T (not show here). Non-stoichiometric $YFe_2O_{4-\delta}$is even at 29 T at 4.2 K not saturated in contrast to $LuFe_2O_4$where the magnetic moment saturates above 10 T at 4.2 K [29]. The thermoremanent magnetic moment in $YbFe_2O_4$ is somewhere between $LuFe_2O_4$and $YFe_2O_{4-\delta}$while the magnetic moment is higher through the paramagnetic moment of the Yb^{3+} ions [29]. Jumps in the magnetization of non-stoichiometric

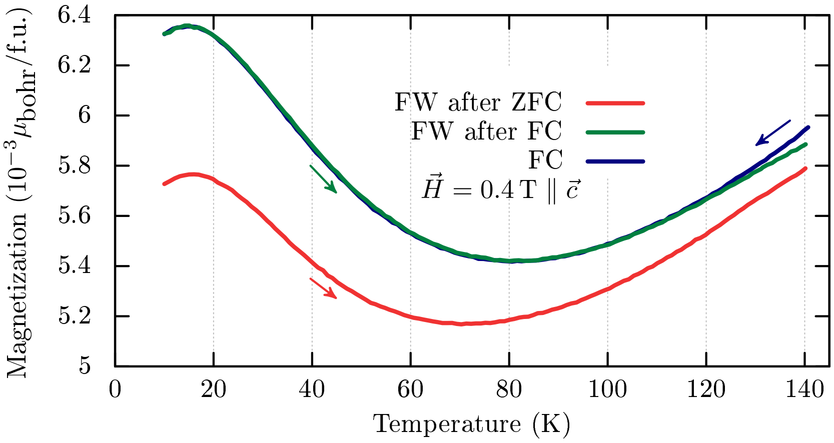

Figure 3.16: Magnification of the low temperature region of Fig. 3.14, showing the magnetization of sample Z8G5real_S1 below 140 K. The red curve is measured during field warming (FW) at $H = 0.4\,\mathrm{T}$ after cooling without field, the green curve during FW after cooling in a 0.4 T field and the blue curve is field cooling (FC).

$YFe_2O_{4-\delta}$ at 4.2 K are observed above 15 T. The magnetic field dependence in Figure 3.17 shows some loop effect at 180 K, with an open hysteresis (yellow curve). The closed part between 0 and 5 T was measured directly after cooling from 300 K. This part differs form the part marked with the blue arrow, which was measured after cycling from 0 T to 5 T to −5 T and up to 5 T again. Since the magnetic moment is not saturated, there is no stable end domain state achieved while cycling the field. The magnetization curve at 5 T therefore could end at different values, in dependence of the statistical domain turns. The end state is also influenced by sample history which leads to the observed open loop at 180 K.

The slope of the linear correlation between magnetization and magnetic field decreases from 100 K up to 160 K, where it starts increasing until 230 K. At 230 K there is a strong increase in the magnetic moment and a non linear behaviour showing a small hysteresis loop without saturation observed (Figure 3.18). These derivation is also much weaker present at 240 K and vanishes above 250 K, from where on the field dependence is again strictly linear. The slope of the field dependent magnetization reaches its maximum at 230 K and decreases again for higher temperatures.

The deviations form linear behaviour are in contradiction to [18], who observed only linear field dependence in stoichiometric $YFe_2O_{4-\delta}$ at various temperatures after heating from 77 K. The behaver at 230 K is more similar to the ferrimagnetic magnetization observed in non-stoichiometric samples [15, 18, 81]. But in non-stoichiometric samples these deviation is present at every temperature, with an increase in magnetization to lower temperatures. The temperature dependent magnetization in our samples clearly exclude the possibility of a ferrimagnetic phase away from the transition points.

The temperature dependence of stoichiometric $YFe_2O_{4-\delta}$ Type B samples with no increase to lower temperatures and the absence of hysteresis loops affirm the antiferromagnetic character of $YFe_2O_{4-\delta}$ below 200 K.

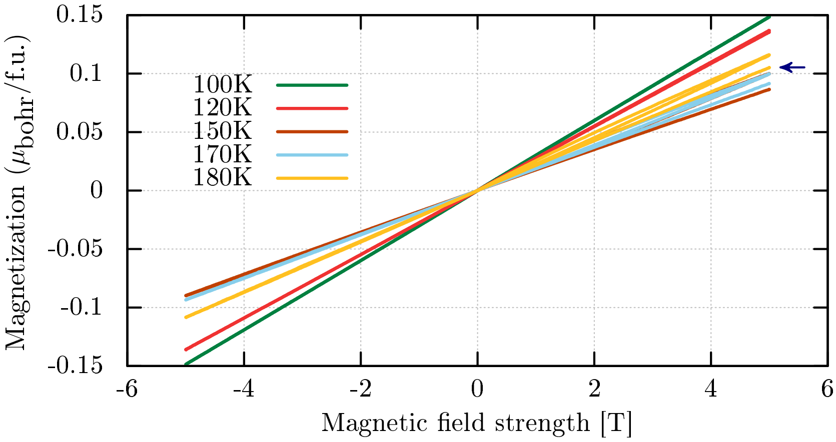

Figure 3.17: Field dependence of magnetization of sample Z2GinfS3 at temperatures between 100 K and 200 K with $\mathbf{H} \parallel \mathbf{c}$.

In the region of the thermal transition points in magnetization at $T_h^c = 228\,\text{K}$ and $T_l^c = 185\,\text{K}$ the field dependence of the magnetization strongly differs form the linear behaviour observed well above or below the transition points. The temperature at the reversal points of the slope of the field dependent magnetization correlate with the transition points in the temperature dependent magnetization.

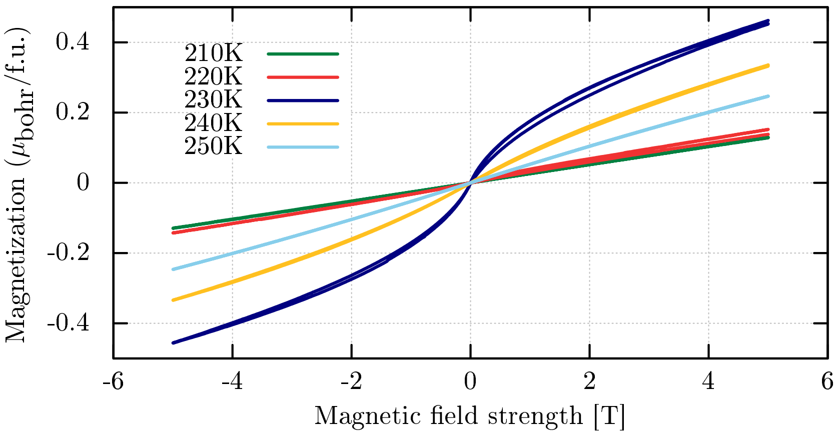

Figure 3.18: Field dependence of magnetization of sample Z2GinfS3 at different temperatures above 200 K with $\mathbf{H} \parallel \mathbf{c}$.

Metamagnetic transitions, as there are observed in $LuFe_2O_4$ below the Néel temperature [11], are not observed in stoichiometric

$YFe_2O_{4-\delta}$ up to 7 T. Switching between the cooling and warming phases through magnetic field, could not be established in $YFe_2O_{4-\delta}$. A ferrimagnetic phase like in $LuFe_2O_4$ [66] is not present in $YFe_2O_{4-\delta}$, the magnetic phase diagram consist only of two regions an antiferromagnetic below the Néel temperature of ca. $T_h^c = 228\,K$ and a paramagnetic phase above the Néel temperature.

3.1.2.2 *Specific heat*

The specific heat measured with a Quantum Design PPMS on a stoichiometric single crystal is show in Figure 3.19. The heat capacity obeys two peaks at the same transition temperatures as observed in magnetization. The jump at the higher transition temperature is much bigger, which is in accordance with the magnetic transitions. Tanaka et al. [21] observed in polycrystalline specimens an increase of the slope in specific heat at the lower temperature transition, which is in contrast to our observed peak. The jump in specific heat indicating latent heat is characteristic for a first order transition. At the higher temperature transitions these latent heat leads to a larger specific heat as the prediction from Dulong-Petit law.

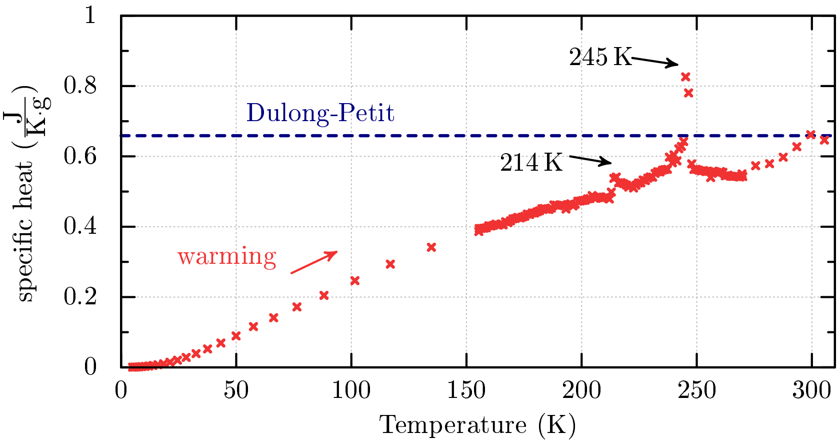

Figure 3.19: Specific heat of 1.08 mg sample Z2Ginf_S3 which is stoichiometric from magnetically Type B. The blue curve is the prediction from Dulong-Petit law, which sets an upper limit for the phononic specific heat contribution, ignoring molecule degrees of freedom or electron contributions.

3.1.2.3 *Conclusion*

We were able to grow stoichiometric single crystals of $YFe_2O_{4-\delta}$ with $\delta < 0.03$. The control of the oxygen partial pressure during growth is essential to receive stoichiometric samples. Only with a $CO_{2}{}_{7}CO$ ratio between 2.77 and 2.94, stoichiometric crystals were obtained. We further found strong inhomogeneities of the crystals stoichiometry in samples from the same growth. Beside the gas mixture also the position on the growth rod is important. The last grown part which has the best crystal quality, is always found to be non-stoichiometric, even with the best gas mixture. While the lowest part of the seed rod, which was grown first, tends to be stoichiometric while choosing the right gas mixture. The difference between both parts is the cooling process. While the first grown part slowly cools, as it travels downwards during growth with 1 mm/h, the last grown part is abruptly cooled when seed and feed rod are separated after the growth. One can see in Figure 3.12 that the first grown part consist of partially decomposed material. Due to the metastable state of $YFe_2O_{4-\delta}$ below 1100 °C [13], it decompose to $YFeO_3$ and FeO. Why the decomposition process, already observed by Shindo et al. [14] is only partially is unknown. Since the cooling rate is very low for the first grown part, quenching, as it is used in powder synthesis, is an unlikely explanation. One can observe that big crystallites with large facets survive the decomposition process. This might indicate that the energy benefit of the crystal structure might be enough to prevent dissociation. The last grown part, which is rapidly cooled shows no decomposition. Beside this the decomposition is isotropic over the rod, with no preferential dissociation at the surface. Even near stoichiometric samples exhibit subtle differences for example in magnetization between Type B and C, which indicates a competition of ground states.

3.1.3 *Room temperature structure*

The crystals structure of our grown crystals at room temperature for different stoichiometry was determined using single crystal x-ray diffraction. The structure of $YFe_2O_{4-\delta}$ was correctly identified by the Diffractometer Software, as rhombohedral layered structure with space group $R\bar{3}m$. Any diffuse scattering from charge ordering was ignored in structure refinement. Table 3.2 gives the lattice constants for a sample from the first growth, the full structure parameters including atomic positions and anisotropic displacement parameters can be found in Section A.7.1. The solution is comparable to [32], while the residual $R1 = 0.0319$ is better.

a (Å)	3.5199(3)	α / β (°)	90	R(int)	0.0456
c (Å)	24.822(2)	γ (°)	120	R(σ)	0.0156
Volume (Å^3)	266.34(5)	Reflections	1376	unique	114
R1	0.0319	ωR2	0.0665	Goof	1.204

Table 3.2: Lattice constants and residuals from structural refinement of single crystal x-ray diffraction data of non-stoichiometric sample Z1.

Table 3.3 gives the lattice constants for sample Z8G5_S1, which was also used in neutron diffraction, and is stoichiometric. The full structure parameters can be found in Section A.7.2. Both the a and the c lattice constants are significant smaller compared to the non-stoichiometric sample. For the a lattice constant this is in accordance with the observations in powder (Fig. 3.3), but in case of the c lattice constant an increase with decreasing oxygen vacancies is observed in powder samples. Figure 3.20(b) compares the observed structure factors F_{obs} with the calculated ones F_{calc}. The blue curve in Figure 3.20(b) is $f(x) = x$, the ideal distribution. For both samples the calculated structure factors are in good agreement with the observed ones. For sample Z8G5_S1 the correlation is a slightly inferior to that of sample Z1, which is also indicated by the higher R1 value of 0.047 compared to $R1 = 0.0319$ for Z1.

a (Å)	3.51425(19)	α / β (°)	90	R(int)	0.039
c (Å)	24.771(2)	γ (°)	120	R(σ)	0.025
Volume (Å^3)	264.94(6)	Reflections	653	unique	118
R1	0.047	ωR2	0.108	Goof	1.284

Table 3.3: Lattice constants and residuals from structural refinement of single crystal x-ray diffraction data of stoichiometric sample Z8G5_S1.

Figure 3.20(a) shows the determined structure of the stoichiometric sample.

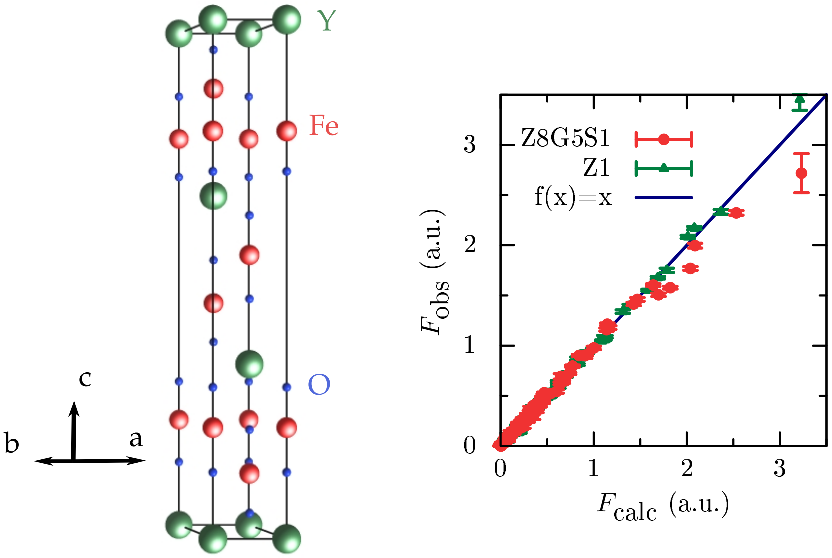

(a) Room temperature R$\bar{3}$m structure of stoichiometric $YFe_2O_{4-\delta}$ sample Z8G5_S1. (Figure created with [82].)

(b) Observed structure factors against calculated ones for sample Z1 and Z8G5_S1.

Figure 3.20

3.2 CHARGE ORDER

In the $YFe_2O_{4-\delta}$ crystals grown by Shindo et al. [14] no scattering from charge ordering was observed [16]. Electron diffraction studies on small non-stoichiometric single crystals showed diffuse scattering along reciprocal (1/3 1/3 ℓ), originating from two-dimensional charge ordering [20]. This superposes the diffuse magnetic scattering at the same position [16], making separation in non polarized neutron scattering difficult. Single-crystals x-ray diffraction, which would easily identify a scattering contribution from charge order, is not reported so far.

In stoichiometric $YFe_2O_{4-\delta}$ a huge variety of electron diffraction experiments showed three-dimensional charge ordering [7, 20, 36, 39–41, 83, 84]. Due to a lack of larger stoichiometric $YFe_2O_{4-\delta}$ crystals, single crystal x-ray and neutron diffraction is not reported.

In contrast to $LuFe_2O_4$ where the charge ordered superstructure was developed using single crystal x-ray diffraction [8], the low temperature ordering in $YFe_2O_{4-\delta}$ is not understood. Therefore we focused on x-ray diffraction studies on $YFe_2O_{4-\delta}$ single crystals.

3.2.1 *Two-dimensional charge ordering in non-stoichiometric single crystals*

Figure 3.21 shows the projection of the reciprocal hhℓ plane received from single crystal x-ray diffraction of sample Z5G2. The sample is non-stoichiometric with magnetic behaviour of Type A (Figure 3.13). Shown are measurements at room temperature and at 100 K which is well below the transition temperature around 200 K in non-stoichiometric $YFe_2O_{4-\delta}$. The indexation follows the hexagonal metric of the rhombohedral $R\bar{3}m$ structure. The projections consists of more than 1500 unique frames each, with counting times between 5 and 20 seconds in dependence of the scattering angle 2θ. The form factor decreases with increasing 2θ, which is compensated by a higher counting time. The step width of the ω scans is 1°.

Beside the structural $R\bar{3}m$ reflections, there are at 300 K diffuse lines along (1/3 1/3 ℓ) and (2/3 2/3 ℓ) observable. Indicating a two-dimensional ordered threefold superstructure, which is in general in accordance with Matsui [20], Mori [40] and Horibe [41]. The zig-zack-type twisting of the diffuse lines, observed by all three in strongly non-stoichiometric $YFe_2O_{4-\delta}$ is not observed in our sample within experimental resolution. The variation should be visible if it is as large, as observed for the sample with $CO_2/CO=0.5$ in [41]. But it is unlikely, that our sample has such a strong off-stoichiometry in consideration of the gas mixture during growth. Such a zig-zack variation of the diffuse lines would indicate perturbations in the two-dimensional ordering inside the hexagonal planes. The broadness along ℓ is char-

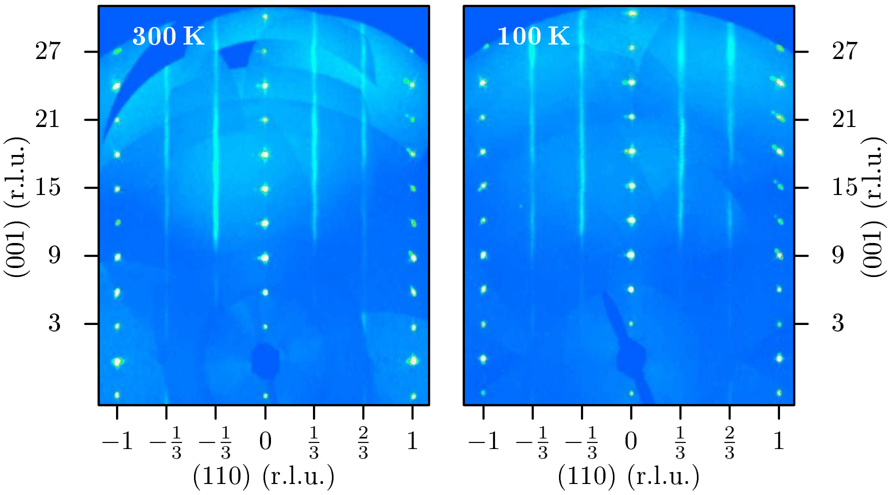

Figure 3.21: X-ray diffraction precession image of non-stoichiometric $YFe_2O_{4-\delta}$ single crystal with magnetic behaviour of Type A. Projection in the (hhℓ) plane at 300 K (left) and 100 K (right) on cooling.

acteristic for a two-dimensional system. While in plane the Fe^{2+} and Fe^{3+} are well ordered, there is no long-range correlation between different layers. Since the distance of irons in different layers is much bigger than the in plane nearest neighbour distance, in plane correlation is much stronger. Cooling to 100 K there is no change in the x-ray diffraction pattern in our sample. For the non-stoichiometric sample showing straight diffuse scattering at room temperature, Horibe et.al [41] observed at 100 K the superposition of (1/3 1/3 1/2) superstructure reflections with straight diffuse scattering. While the diffuse zig-zag-type scattering observed in samples with more oxygen vacancies, converts into straight diffuse lines along (1/3 1/3 ℓ) at 100 K [41]. Such zig-zag-type diffuse scattering was also observed in $YbFe_2O_4$ [85] and $LuFe_2O_4$ [86, 87], where it was explained by charge density waves [11]. Our sample seems to be between the two $YFe_2O_{4-\delta}$ samples from Horibe et al. [41], showing straight diffuse scattering, which stays completely two-dimensional down to 90 K. Since our sample is much bigger than these used for electron diffraction, possible surface influences are reduced.

The projection images at 100 K and 300 K show both a small second grain, which distributes small peaks, slightly shifted from the structural positions of the primary crystal. These additional reflections can be well observed at (0 0 24), (1 1 24) and (1 1 21).

3.2.2 *Three-dimensional charge ordering in stoichiometric single crystals*

Figure 3.22 and 3.23 show the reciprocal hhℓ map of stoichiometric sample Z2Ginf_S3 which has a magnetization of Type B (App. A.6). At room temperature x-ray diffraction shows the same diffuse lines along reciprocal ($^1/_3$ $^1/_3$ ℓ) (Fig. 3.22 (left)). Although the lines appear non continuously, the zig-zag-type twisting [41] is not observed, like it is in our non-stoichiometric sample.

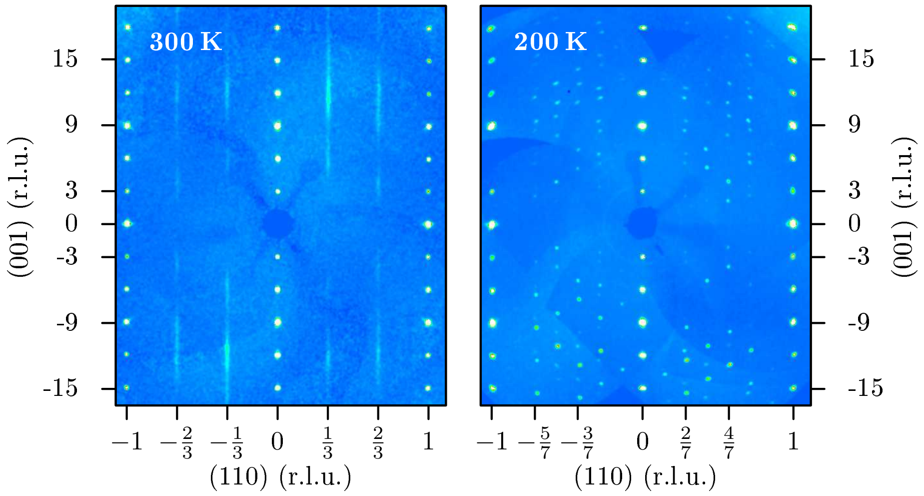

Figure 3.22: X-ray diffraction precession image of stoichiometric $YFe_2O_{4-\delta}$ single crystal with magnetic behaviour of Type B. Projection in the (hhℓ) plane at 300 K (left) and 200 K (right) on cooling.

The ($^1/_3$ $^1/_3$ $^1/_2$) superstructure observed at room temperature in [41] and [40] is not present. In [41] this was clearly linked to an oxygen deficit, which might suggest that our sample is still slightly off stoichiometric. This is in contrast to the magnetic behaviour, which is the same as those of $YFe_2O_{4-\delta}$ samples with oxygen deficient $\delta = 0.00$ [18]. magnetization curves or measurements of the oxygen deficit are not reported in [41] or [40] and differences by electron diffraction from XRD have been observed also for $LuFe_2O_4$[86]. Furthermore a recent report [76] indicates it might be due to oxygen vacancy ordering. Only for synthesis gas mixture $CO_2/CO = 1.5$ the temperature dependence of the magnetic susceptibility in [41] is the same as for $\delta = 0.00$. In [40] it is unclear if three-dimensional charge ordering was observed for synthesis gas mixture $CO/CO_2 = 1.5$ or $CO/CO_2 = 0.5$. Since the sample synthesized under $CO/CO_2 = 0.5$ would have a lower oxygen deficit, three-dimensional charge ordering should occur here, which would be in compliance with [41], where 3D charge ordering was only observed for synthesis gas mixture of $CO_2/CO = 1.5$ and $CO/CO_2 = 0.67$ respectively. Matsui et al. [20] observed that the ($^1/_3$ $^1/_3$ $^1/_2$) superstructure reflections vanishes with increasing electron beam intensity. They assume that the ($^1/_3$ $^1/_3$ $^1/_2$) reflections originate from ordered lattice distortions which are healed by beam heating [20]. For example oxygen vacancy ordering could lead to an additional superstructure. This explanation is incompatible with Horibes [41] observation that the ($^1/_3$ $^1/_3$ $^1/_2$) superstructure reflections occur only in samples with least oxygen vacancies. One explanation could be the formation of $YFe_2O_{4-\delta}$ with a negative δ (i.e. more than four oxygen per formula unit), but it is unclear if and how additional oxygen could be arranged in the rhombohedral crystal. In the phase diagram of the Fe-Fe_2O_3-Y_2O_3 system [12], there is no indication for such a compound, they specified the maximum deviation from stoichiometry in $YFe_2O_{4-\delta}$as $0.000 \leqslant \delta \leqslant 0.095$. In case of $LuFe_2O_4$, $LuFe_2O_4 - \delta$ with a negative δ is observed [75, 76].

Cooling to 200 K, which is directly below the higher temperature transition in magnetization, the precession image of the reciprocal hhℓ-plane (Fig.3.22 (right)) changes drastically and complex three-dimensional charge ordering occurs and the diffuse scattering vanishes. For a sample showing only diffuse scattering at room temperature, this is in contradiction to the electron diffraction in [41], where diffuse lines stay down to 100 K. Ikeda et al. [7] observed a similar behaviour with diffuse lines at room temperature which convert to superstructure reflections below the Néel temperature. The present superstructure reflections in our sample could all be described by a single propagation vector **Q** = ($^1/_7$+τ $^1/_7$+τ $^9/_7$). The small incommensurability τ observable in the hh position is smaller than 0.009 (r.l.u.). However a lot of superstructure reflections with propagation vector **Q** = ($^1/_7$+τ $^1/_7$+τ $^9/_7$) are missing. There are large empty areas in reciprocal space, could be explained by twinning. The sample is relatively large and for different sample orientations it could be, that the beam only scatters on the twin. The same propagation vector is found in stoichiometric $YFe_2O_{4-\delta}$ at 100 K in [41, 83, 84], while there is no incommensurate shifting reported. And all these samples show, in contrast to ours, superstructure reflections already at room temperature. In contrast a ($^1/_2$ $^1/_2$ 0) propagation vector is reported for the temperature region between 200 and 225 K on warming [7]. Assuming the same thermal hysteresis as observed in magnetization, the phases should be shifted to lower temperatures on cooling about 20 K. At a temperature above 233 K on warming which would correspond to our phase with **Q** = ($^1/_7$+τ $^1/_7$+τ $^9/_7$) a threefold superstructure **Q** = ($^1/_3$ $^1/_3$ 0) is observed [7]. In contrast we observe the phase being shifted to higher temperatures, which could be explained through oxygen deficits. In our sample the charge ordering changes drastically while passing the higher temperature magnetic transition, like in [7]. While in the sample from [88], charge ordering does not vary at the magnetic transition on heating. And Mori et al. [40] suggested based on electron diffraction, that three-dimensional charge ordering stays up to 368 K in stoichiometric samples. The observed jumps in electric conductivity [21, 37] in $YFe_2O_{4-\delta}$at the magnetic transitions points, as well as the transition in the Seebeck coefficient [27], indicate changes in the charge ordering at the magnetic transition points. This is in contrast to the observation of long-range three-dimensional charge ordered phases far above the Néel temperature [40, 41], without any change at the magnetic transition points [88].

While coupling between charge ordering and magnetic ordering might be more likely for a common transition, the continuity of three-dimensional charge ordering well above the Néel temperature is also observed in $LuFe_2O_4$ [11, 89].

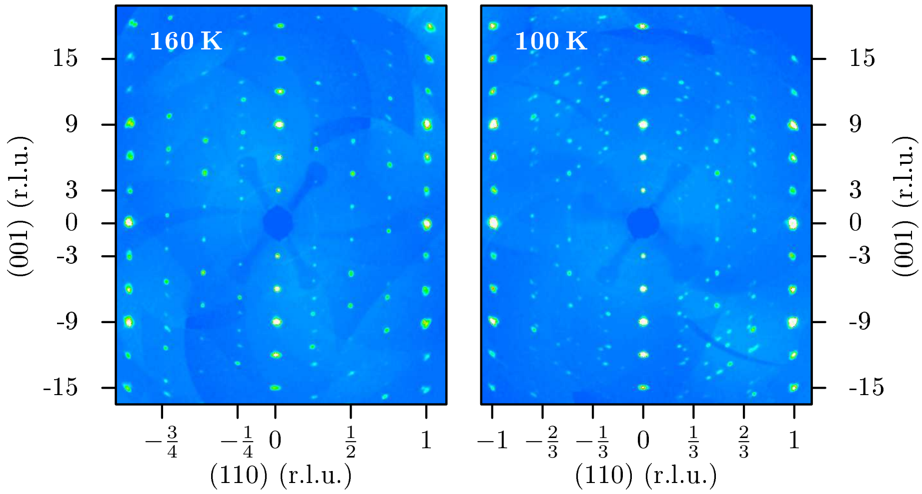

Figure 3.23: X-ray diffraction precession image of stoichiometric $YFe_2O_{4-\delta}$ single crystal with magnetic behaviour of Type B. Projection in the (hhℓ) plane at 160 K (left) and 100 K (right) on cooling.

Cooling further, below the lower transition temperature in magnetization, the x-ray diffraction pattern change, to that in the left part of Figure 3.22. This phase seems to be the only commensurate phase with propagation vector $\mathbf{Q} = (1/4\ 1/4\ 3/4)$. Again a lot reflections, which could be indexed with this propagation vector, are missing. Regardless of thermal hysteresis this phase corresponds to the one in electron diffraction reported by Ikeda et al. [7] between 140 K and 190 K which obeys (1/4 1/4 0) reflections in the $(hk0)$-plane. While they also observed a four times in plane enlarged supercell, the reflections observed in the $(hk0)$-plane are incompatible with the propagation vector $\mathbf{Q} = (1/4\ 1/4\ 3/4)$ in our sample. The additional phase with superstructure reflections at (1/2 1/2 0) between 190 K and 225 K on warming [7] is not observed in our sample on cooling.

At 100 K the x-ray diffraction precession image changes again, to that in the right part of Figure 3.23. The transition temperature is somewhere between 160 K and 100 K, and was not evaluated. The propagation vector here is hard to estimate. The reflections which could be indexed with **Q** = (1/4 1/4 3/4) are still present but weaker than at 160 K. Some of the other reflections could be indexed with **Q** = (1/7+τ 1/7+τ 9/7). Horibe et al. [84] observed at 100 K also a very complex structure with propagation vector **Q** = ($\overline{1/14}$ 2/7 1/14), which is compatible to our observation, but does not describe all reflections.

At the Hasylab PETRA III P09 beamline we observed an additional phase at 10 K with (1/3 1/3 half-integer)-reflections, which might be equal a phase observed of $LuFe_2O_4$ [8, 90, 91]. This is so far the only confirmation for this phase and it is only observed in sample Z2Ginf_S3. The magnetization of this sample (Fig. A.9) is of Type B and shows no difference to other high quality samples in the low temperature region. Sample Z8G5_S1 shows no structural or magnetic transition below 160 K in neutron diffraction. Figure 3.24(a) shows a scan along reciprocal ℓ-line trough this (1/3, 1/3, half-integer)-reflections. The peak at $\ell = 15.5$ is much stronger than the others, through a possible misalignment of the UB-matrix, and aligning on this peak before the ℓ-scan.

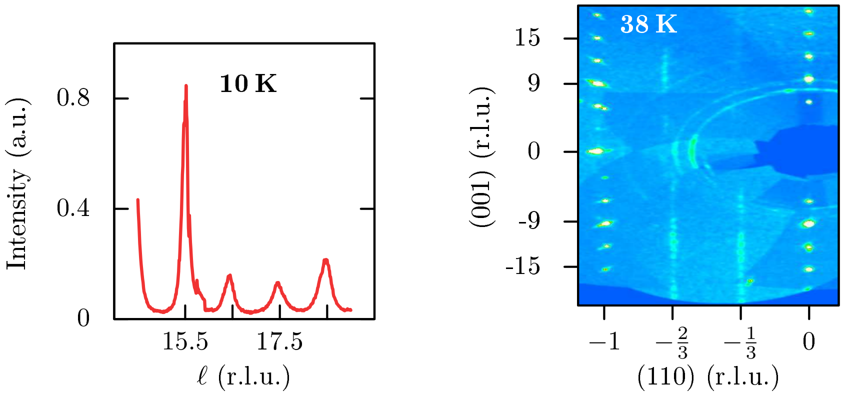

(a) Reciprocal scan along (1/3 1/3 ℓ) at 10 K on cooling. Recorded at the PETRA III P09 beamline.

(b) Projection in the (hhℓ) plane at 38 K on cooling. Recorded with the SuperNova diffractometer and the HeliJet option.

Figure 3.24: X-ray diffraction of stoichiometric $YFe_2O_{4-\delta}$ single crystal with magnetic behaviour of Type B. (Sample Z2Ginf_S3, for the Supernova experiment only a small part of the sample is used.)

Further efforts to examine this temperature region using the Helijet on the SuperNova diffractometer, were prevented by a defect of the Helijet, which could not reach a temperature below 37 K. At 37 K the three-dimensional charge ordering vanishes and is replaced by the same diffuse lines along (1/3 1/3 ℓ), which are observed at room temperature (Figure 3.24(b)). The reduction to a lower ordered system on cooling is very surprising, but is in accordance with Ikeda et al. [35, 88], who observed diffuse Bragg rods through (1/3 1/3 4.5) below

60 K. There is no change in neutron diffraction between 160 K and 10 K in sample Z8G5 shown in Figure 3.36. The charge ordering, present in non spin-flip channel, is dominated at both temperatures by (1/2 1/2 3/2) superstructure reflections. They are compatible with the observed charge ordering in x-ray diffraction with a propagation vector of $\mathbf{q} = (1/4\ 1/4\ 3/4)$. The (1/2 1/2 3/2) reflections are in x-ray diffraction the strongest superstructure reflections, since two different $\mathbf{q} = (1/4\ 1/4\ 3/4)$ reflections superpose here. Identifying other superstructure reflections in the neutron diffraction is difficult.

Due to the large detector area which also collects reflections laying outside the horizontal scattering plane, it is not clear if all the weak reflections in Figure 3.36 and Figure 3.35 are laying in the reciprocal $hh\ell$-plane, or in slightly shifted parallel planes. Also the neutron sample obeys a small twin, which could also lead to very weak superstructure reflections. The (1/3, 1/3, half-integer) superstructure reflections in the x-ray diffraction in Figure 3.24(a) are not observed in neutron diffraction at 10 K, which is most likely caused by sample variations.

Regarding the diffuse lines at 37 K in x-ray diffraction one should consider, that the sample could have become non-stoichiometric over time or during previous experiments. The sample was never heated above room temperature, which could cause oxidation in air or loss of oxygen in vacuum. But the heat capacity measurement was performed directly after the P09 experiment, before the observation of the diffuse lines at lower temperature. As well the sample was cleaned with aceton after the P09 experiment. To exclude this possibility, the charge ordering at 160 K for example should be checked again by x-ray diffraction, which was not done so far. The powder rings observed in Figure 3.24(b) originate from ice, which developed on the sample during operation of the HeliJet.

Through modelling of the near edge structure of the resonant x-ray diffraction of $LuFe_2O_4$ over the Fe K edge on various (1/3 1/3 half-integer) superstructure reflections, Mulders et al. [60] received the anomalous scattering factors of both Fe sites, which allows them to proof the full charge separation into Fe^{2+} and Fe^{3+} through the calculation of the chemical shift between both Fe ions [60].

We have done an similar experiment on $YFe_2O_{4-\delta}$ at the P09 PETRA III beamline, one the (1/3 1/3 half-integer) supersturcture at 10 K, show in Figure 3.24(a). Figure 3.25 shows the x-ray energy spectra of $YFe_2O_{4-\delta}$over the iron K-edge at 10 K in $\sigma \rightarrow \sigma$ on $(1/3\ 1/3\ \ell)$ for different half integer ℓ-values. The scattering vector $\mathbf{Q}$ was kept constant during each energy scan. The data is normalized and shifted. In Figure 3.26 the same data is presented after correction for absorption using the fluorescence signal. The shown curves are the mean of four independent energy scans each, the statistical fluctuations are strong.

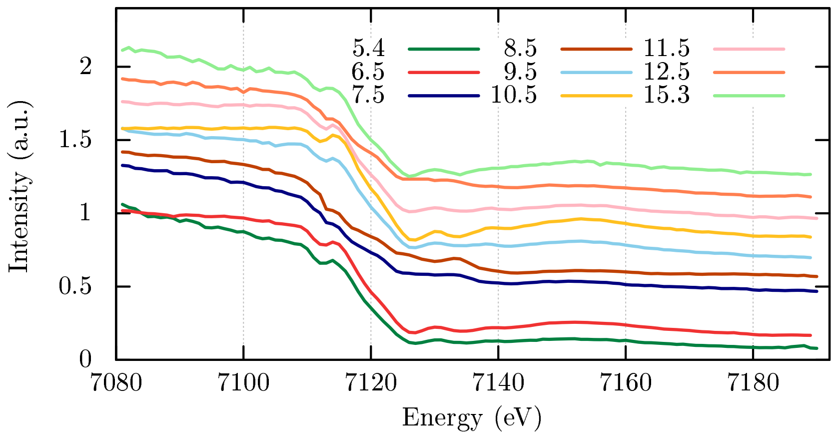

Figure 3.25: Energy spectra over the Fe K-edge on $(1/3\ 1/3\ \ell = \text{half-integer})$ for different half-integer ℓ at 10 K (data is normalized and shifted) but not corrected for absorption.

The resonant signal in $YFe_2O_{4-\delta}$ compared $LuFe_2O_4$ is weak [60]. The characteristic up-down variations of the post edge features observed by Mulders et al. [60] in $LuFe_2O_4$ are observable in $YFe_2O_{4-\delta}$ after absorption correction, but the energy resolution and the statistic fluctuations are unsatisfactory. Nevertheless it is possible to differ two types of RXS spectra, best observable in the variation of the post edge feature at 7130 eV. The spectra for $\ell \in \{5.4,\ 6.5,\ 9.5,\ 10.5,\ 11.5\}$ feature local maxima at 7130 eV (Fig. 3.26(a)), whereas the spectra for $\ell \in \{7.5,\ 8.5,\ 12.5\}$ exhibit local minima (Fig. 3.26(b)). The switch between the feature heading from ↑ at $\ell = 6.5$ to ↓ at $\ell = 7.5$ and 8.5 and back to ↑ at $\ell = 10.5$, occurs at the same ℓ values which where found on the $(2/3\ -1/3\ \text{half-integer})$-reflections in $LuFe_2O_4$ by Mulders et al. [60]. Neglecting the different h and k position the heading of the feature is reversed for the same ℓ-values compared to $LuFe_2O_4$. Fitting the near edge structure like it was done in [92], to receive the chemical shift between different iron valences in $YFe_2O_{4-\delta}$ is beyond the scope of this thesis.

The charge ordering in non-stoichiometric samples is two-dimensional down to 90 K, the lowest temperature in the measurement.

In contrast the observed charge ordering in highly stoichiometric $YFe_2O_{4-\delta}$ single crystals on cooling in x-ray diffraction, which differs from result from electron diffraction [40, 41, 84], could be summarized as followed:

- **300 K–250 K** diffuse lines along $(1/3\ 1/3\ \ell)$
- **250 K–170 K** propagation vector $\mathbf{q} = (1/7{+}\tau\ \ 1/7{+}\tau\ \ 9/7)$ with $\tau \leqslant 0.009$
- **160 K** propagation vector $\mathbf{q} = (1/4\ 1/4\ 3/4)$

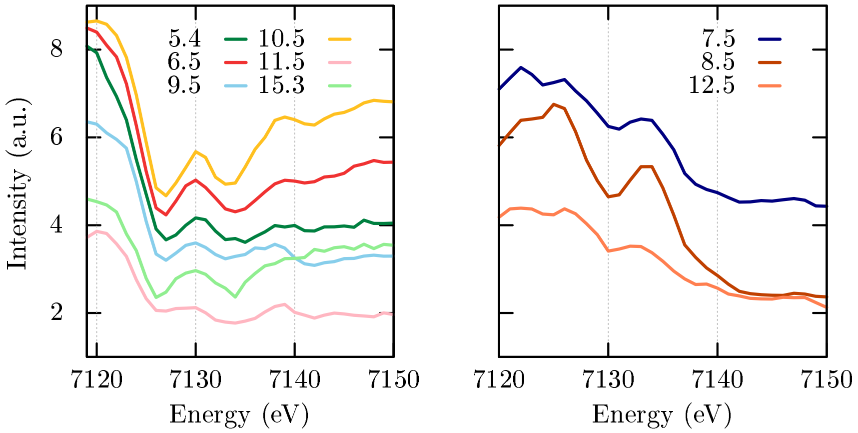

(a) 7130 eV up-feature.

(b) 7130 eV down-feature.

Figure 3.26: Energy spectra over the Fe K-edge on $(^1/_3\ ^1/_3\ \ell)$ for different half-integer ℓ at 10 K (data is normalized, corrected for absorption and shifted) .

- **100 K** complex pattern with $\mathbf{q} = (^1/_4\ ^1/_4\ ^3/_4)$ reflections and additional not clear propagation vector
- **37 K** diffuse lines along $(^1/_3\ ^1/_3\ \ell)$
- **10 K** $(^1/_3\ ^1/_3$ half-integer) reflections (not in neutron diffraction)

The error on the temperature ranges is always 10 K. Data on not specified ranges is not available.

3.2.3 *The question of orbital order*

[1] Since we have only insufficient data on the superstructure reflections at 10 K in Figure 3.24(a), the origin of them is unknown. Beside the obvious possibility of charge ordering of Fe^{2+} and Fe^{3+}, orbital ordering is another alternative explanation. The question if there exists an orbital ordered state was for $LuFe_2O_4$ discussed by Mulders et al. [60]. They found no anisotropy in the x-ray scattering in dependence of polarization or azimuthal angle, which indicates random orientation of Fe ions and therefore and orbital glass state [60]. Orbital long-range ordering is theoretically expected in the RFe_2O_4 system (R = rage earth) [11, 93, 94]. In $LuFe_2O_4$ no additional reflections originating from orbital order were observed, and a contribution of orbital order would lead to anisotropy in the charge order scattering [11, 95]. De Groot [11] observed a dependence of incoming polarization state in the x-ray scattering of the $(\tau\ \overline{2\tau}\ ^3/_2)$ reflection at the Fe $L_{2/3}$-edges, here τ marks the incommensurable of the satellite reflection. The soft

---

[1] Parts of this chapter have been submitted as an experimental report to the DESY annual report.

x-ray experiment at the Fe $L_{2/3}$-edges is more sensitive to electronics, as the resonances at the Fe K-edge are smaller. This anisotropy is also present in the high temperature region where orbital order was excluded by XMCD [11]. An orbital contribution in the low temperature region was excluded by full polarization analysis on the $(\tau\, \tau\, ^{27}/_{2})$ superstructure reflection in the resonant x-ray diffraction over the Fe K-edge [11].

In the case of $YFe_2O_{4-\delta}$ the question of orbital order was never addressed before. Which makes us focus on studies on polarization dependent anisotropy in the resonant x-ray diffraction over the iron K edge.

We first focused on the 10 K superstructure in Figure 3.24(a).

Figure 3.27 compares the resonant spectra of the $(^1/_3\ ^1/_3\ 6.5)$ superstructure reflection in $\sigma \rightarrow \sigma$ to that in $\sigma \rightarrow \pi$. The intensity in $\sigma \rightarrow \pi$ is scaled by a factor of 5000.

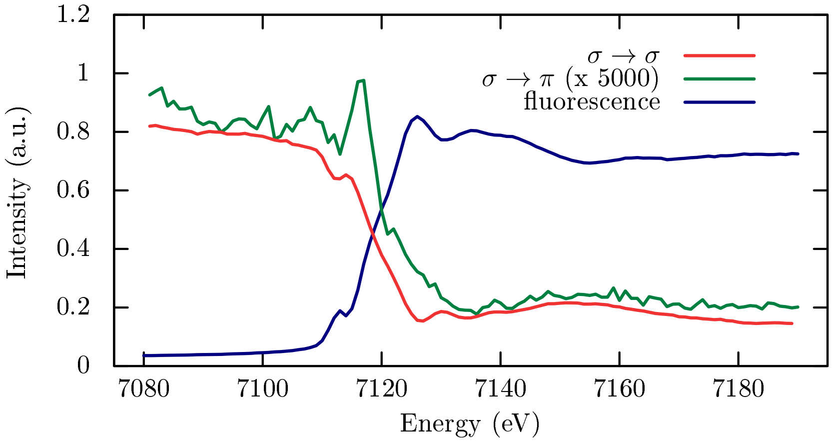

Figure 3.27: Energy spectra around the Fe K-edge on $(^1/_3\ ^1/_3\ 6.5)$ at 10 K.

The feature at 7116.5 eV, being relatively larger in $\sigma \rightarrow \pi$, indicates some anisotropy. To examine this anisotropy full polarization analysis was performed, as described in Section 2.4.1.

The resulting Stokes parameters are shown in (Fig. 3.28). The yellow and blue dots mark Stokes parameters P1 and P2 for the direct beam, the solid lines of the same colour are sinusoidal fits. The red and green dots mark Stokes parameters from the scattered beam at 7116 eV, the solid lines correspond to calculations for an ideal Thompson scatter, after Equations 2.14–2.16.

The behaviour is very similar to that calculated for an ideal Thompson scatterer. Therefore the scattering contribution is dominated by isotropic charge scattering. This could be explained by the weakness of the feature present in $\sigma \rightarrow \pi$ in comparison to the intensity in $\sigma \rightarrow \sigma$. Therefore even at the resonance energy the polarization analysis mainly probes the structure.

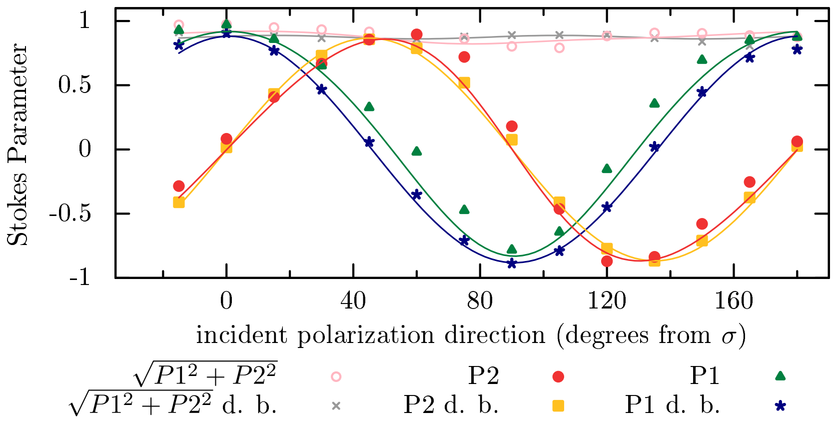

Figure 3.28: Polarization analysis at 10 K on 7116 eV feature in RXRD on (1/3 1/3 6.5) superstructure reflection (errors are the size of the symbols or smaller).

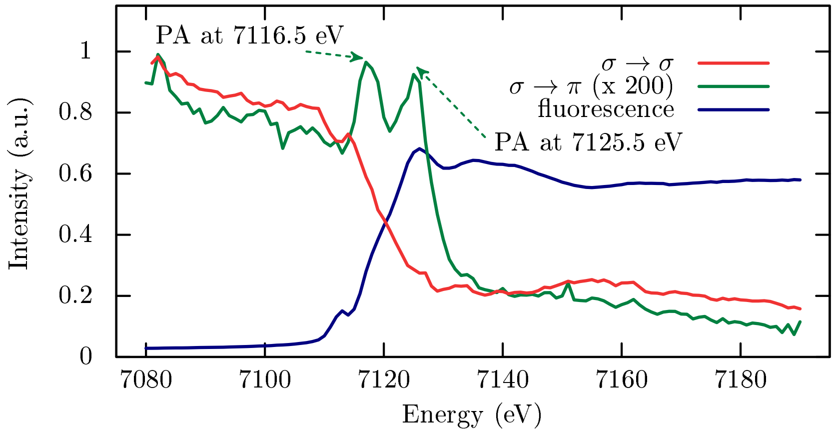

Figure 3.29: Energy spectra around the Fe K-edge on (1/2 1/2 10.75) at 120 K.

In addition to the peaks at (1/3 1/3 half-integer), shown in figure 3.29, we observed peaks at half integer h and k positions. Further studies revealed that they were induced due to beam heating. To examine these peaks we did energy scans at 120 K, where the (1/3 1/3 half-integer)-peaks are absent and one at (1/2 1/2 10.75) is present without beam heating. The energy spectra over the iron K-edge, shown in Figure 3.29, are normalized but not corrected for absorption, which is proportional to the shown fluorescence. At both pre edge features, relatively stronger in $\sigma \rightarrow \pi$, full polarization analysis was performed, for the feature at 7125.5 eV the resulting Stokes parameter are given in Figure 3.30.

The aberration in the polarization analysis from the ideal Thomson scatterer (solid red and green curve) is much stronger for the (1/2 1/2 10.75)-reflection than for the (1/3 1/3 6.5)-reflection. Although the variation to the direct beam is mostly caused by the $2\theta \approx 55°$

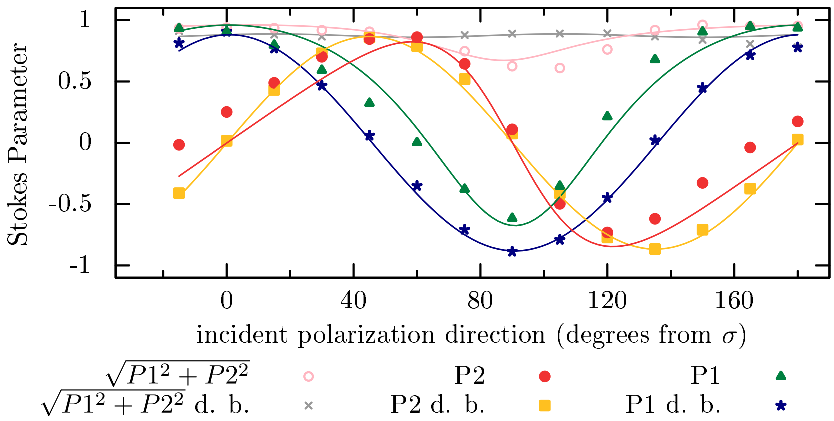

Figure 3.30: [Polarization analysis at 120 K on 7125.5 eV feature in RXRD on (1/2 1/2 10.6) superstructure reflection (errors are the size of the symbols or smaller).

which is closer to 90° than the $2\theta \approx 34°$ of the (1/3 1/3 6.5)-reflection, the polarization analysis gives indication for an anisotropic scattering contribution. The sinusoidal fits of the direct beam should in principle have a fix amplitude of one. In all previous figures the amplitude was freely fitted, because fixing the amplitude to one leads to a bad correlation of the fit with the direct beam data. In Figure A.10 in Appendix A.8, there is exemplary show Figure 3.30 with a fixed amplitude of one in the direct beam fit. Because the improper fit would make the comparison of the polarization dependence of the resonant feature with the isotropic Thompson scattering difficult, the amplitude was freely fitted. The deviation from the ideal amplitude of one, indicates non perfect polarization of the primary beam, which is most likely caused by a misalignment of the phase plates. The polarization analysis of the feature at 120 K on 7118 eV in Figure 3.29 can be found in Figure A.11 in Appendix A.8. The anisotropy is weaker at this energy compared to 7125.5 eV.

The resonant features at 7118 and 71125.5 eV are weak in the x-ray diffraction at 120 K, therefore the polarization analysis mainly tests non-resonant diffraction, thus structural anisotropy. In contrast to $LuFe_2O_4$ with no indications for anisotropy in the resonant x-ray diffraction over the Fe Kedge connected to orbital order , there are indications for weak anisotropy in the resonant x-ray diffraction of $YFe_2O_{4-\delta}$. An orbital contribution in $YFe_2O_{4-\delta}$ can not be excluded, but if it exist, it is expected to be small. Soft x-ray diffraction over the Fe $L_{2/3}$ edges might be better suited to probe orbital order, like it was done in $LuFe_2O_4$ [11], since the resonances at the Fe K edge are weak.

3.3 SPIN ORDER

[2] Spin ordering in $\mathrm{YFe_2O_{4-\delta}}$ single crystals was previously only examined in non-stoichiometric crystals, where diffuse magnetic lines along ($1/3$ $1/3$ ℓ) are observed from room temperature down to 9 K [16, 19, 34]. There is a tendency to three-dimensional ordering observable in less oxygen deficit non-stoichiometric single crystals [19]. Also in stoichiometric powder samples magnetic Bragg peaks incompatible with the diffuse lines are observed [19, 33]. Both Akimitsu et al. [16] and Funahashi et al. [19], remarked that in a perfect single crystal the two-dimensional spin ordering could not be the ground state, and the correlation along the c axis is perturbed through oxygen defects. Since we have grown single crystals, showing for the first time the same macroscopic magnetic behaviour (Fig. 3.14) as stoichiometric powder, we except three-dimensional spin ordering to occur below the Néel temperature. The three-dimensional spin ordering in $\mathrm{LuFe_2O_4}$ below the Néel temperature is present in the hhℓ-plane [66]. And the same diffuse lines along ($1/3$ $1/3$ ℓ) as in $\mathrm{YFe_2O_{4-\delta}}$ are observed well above the Néel temperature [66]. This makes us focus on the reciprocal hhℓ-plane on $\mathrm{YFe_2O_{4-\delta}}$. Since neutrons directly interact with the magnetic Fe spins, they are the ideal probe for spin ordering. Due to the very complex charge ordering and our ignorance of the possible magnetic ordering in $\mathrm{YFe_2O_{4-\delta}}$, we chose the DNS instrument which would allow fast reciprocal space mapping, together with polarization analysis to separate magnetic scattering. The experimental setup can be found in Section 2.5.

3.3.1 *Diffuse magnetic scattering*

Fig. 3.31 shows diffuse scattering observed in the $\mathtt{hh\ell}$-plane after cooling to 252 K.

The signal to noise ratio in Fig. 3.31 is not satisfactory, therefore we decided to redo the experiment at a lower temperature. Cooling down to a temperature slightly above the transition temperature should increase the diffuse scattering intensity drastically, under the estimation, that its behaviour is comparable to the macroscopic magnetization. Increasing the counting time would also increase the signal to noise ratio, but the ratio is only growing with the square root of the counting time. In consideration of the limited beamtime, we decided to use the same counting time of 120 s. We cooled the sample to 236 K, which is slightly above the macroscopic transition peak at 230 K. The $\mathtt{hh\ell}$-map on this temperature obeys already superstructure peaks, which let us assume that the transition point was already underrun, the $\mathtt{hh\ell}$-map can be found in App. A.9. Since we were interested in the diffuse scattering, we heated up the sample to 280 K, to

---

[2] Parts of this chapter have been submitted as an experimental report to the FRM II.

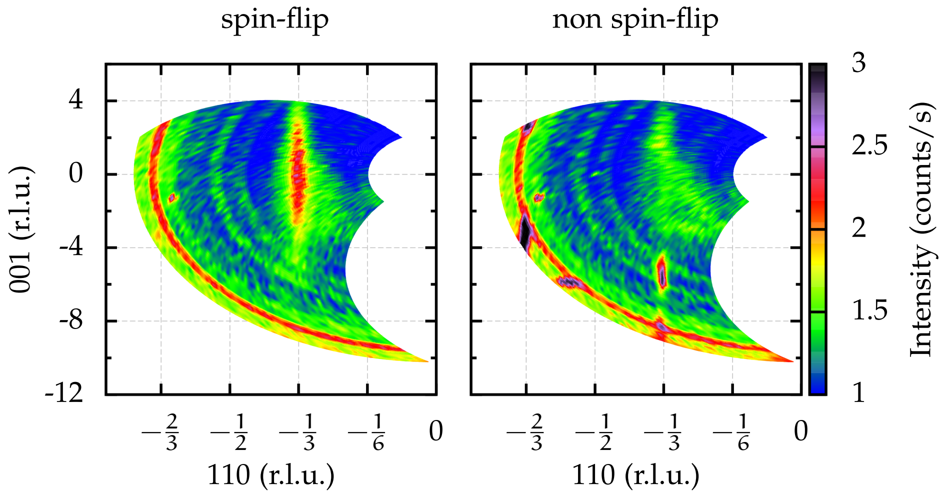

Figure 3.31: hhℓ-plane at 252 K in spin-flip (left) and non spin-flip (right) channel with magnetic field **H** ∥ z — counting time: 120 s — two detector bank positions.

prevent hysteretic effects. Afterwards the sample was cooled to 242 K. The hhℓ-map at 242 K is shown in Fig. 3.32.

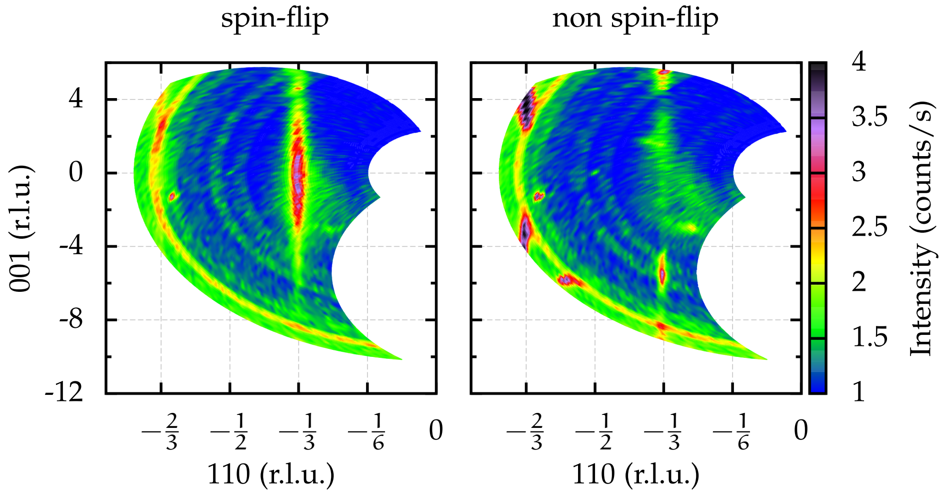

Figure 3.32: hhℓ-plane at 242 K on cooling in spin-flip (left) and non spin-flip (right) channel with magnetic field **H** ∥ z — counting time: 120 s — two detector bank positions.

Above the Néel-temperature $T_N \approx 230$ K on cooling, which is also the charge ordering temperature, diffuse magnetic scattering is observed along (1/3 1/3 ℓ) with neutron polarization **P** ∥ z (Fig. 3.32). The magnetic scattering in spin-flip-channel, with magnetic field **H** ∥ z, is from magnetic moments lying in the hhℓ-plane. From macroscopic magnetic behaviour and crystal symmetry magnetic moments along [110] are very unlikely, so the main spin heading is along [001]. Since the magnetic scattering is broad in ℓ-direction and sharp in hh-direction there is two-dimensional spin ordering in plane of the rhombohedral $YFe_2O_{4-\delta}$-layers. But there is no magnetic long-range correlation between different layers.

To determine the orientation of the magnetic moment also measurements with field in x-direction, i. e. parallel to $\bar{Q}$, were performed. In this orientation all magnetic scattering will be spin-flip, independent of the orientation of the magnetic moment. This is an approximation and is only exact for detectors in the middle of the detector array.

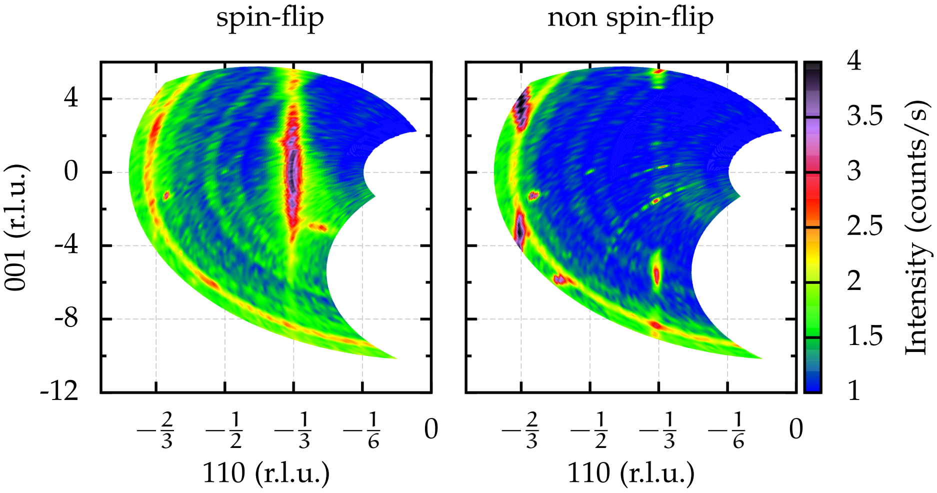

Figure 3.33: $hh\ell$-plane at 242 K on cooling in spin-flip (left) and non spin-flip (right) channel with magnetic field $H \parallel x$ — counting time: 120 s — two detector bank positions.

The diffuse magnetic scattering becomes stronger when the polarization is changed parallel to x (Fig. 3.33), which is roughly parallel to the average $\mathbf{Q}$. Therefore in the two-dimensional ordered phase, the spins are not perfectly aligned along $\mathbf{c}$, but have some ab-components as well. This is also confirmed by a diffuse scattering contribution in the non-spin-flip channel under magnetic field $H \parallel z$, which transfers to spin-flip channel when the field direction is changed to x. The classic XYZ-polarization analysis methode [96] to separate the magnetic scattering contribution is not applicable to single crystals since it require isotropy. But Schweika [97] showed that full XYZ-polarization analysis, to completely separate the diagonal part of the polarization tensor, is also possible for single crystals on multi detector instruments. Since we did not expect strong variations from the Ising spin system, we skipped measuring the third field direction and focused on additional measurements on the temperature dependency in the ordered phase.

The non-spin-flip channel in Fig. 3.32 shows at (-1/2 -1/2 0) the second order of the (-1 -1 0) reflection affirming good crystal alignment. The peak around (-2/3 -2/3 -1.8) is most likely a (0 0 9) contamination of a second grain. The reduction of intensity for the diffuse magnetic scattering to higher ℓ is in accordance with the magnetic form factor and the polarization factor [45].

The ring of high intensity is probably from a small polycrystalline part of the sample. The scattering angle $2\theta \approx 108^\circ$ fits well with the (0 1 5) reflection of $YFe_2O_{4-\delta}$, which is a quite strong reflection with an intensity comparable to (0 0 3). A contribution of the aluminium sample holder is not compatible with the 2θ angle. This ring is only observable in the measurements on the diffuse scattering through the long counting time of 120 s.

The magnetic ordering in $YFe_2O_{4-\delta}$ above the Néel-Temperature consists of ordered layers, which are randomly stacked. This lead to diffuse scattering along ($1/3$, $1/3$, ℓ), which is the same as observed by neutron scattering in the high-temperature-phase of $LuFe_2O_4$ [66]. This was also observed in non-stoichiometric $YFe_2O_{4-\delta}$ [34] by Funahashi et al. They remarked, that the two-dimensional ordering in non-stoichiometric $YFe_2O_{4-\delta}$ could not be interpreted as a variation of the 3D-ordered state in stoichiometric $YFe_2O_{4-\delta}$, disturbed by stacking faults in the spin structure [19]. And that the spin state in non-stoichiometric $YFe_2O_{4-\delta}$ can be described as an anisotropic spin glass [19]. The in plane component of the magnetic moment, is in good agreement with a spin glass state reducing the anisotropic character, which is mainly caused by different inter and intra neighbour distances. The forces between neighbours in one layer are stronger than that to the atoms in a different layer. The intralayer ordering could also be disturbed through oxygen vacancies in the non stoichiometric sample. In $LuFe_2O_4$ no measurements with neutron polarizations $\mathbf{P} \parallel \bar{\mathbf{Q}}$, which could probe the assumption of an Ising spin system, were reported neither in the diffuse phase above the Néel temperature or in the ordered phase.

3.3.2 *Three dimensional magnetic ordering*

Fig. 3.34 shows the $hh\ell$-reciprocal-plane at 200 K after cooling from room temperature. The left figure corresponds to spin-flip scattering and the right to non-spin-flip scattering.

200 K is just below the higher temperature transition and in x-ray-diffraction there is 3D-charge ordering observed.

Cooling further below the second transition the pattern changes to the one shown in Fig. 3.35.

Besides background fluctuations, the pattern obtained at 12 K looks exactly the same as the one at 160 K, it is shown in Figure 3.36. Since the pattern does not change, we assume that there is no magnetic transition between 160 K and 12 K. As shown in Figure 3.37 and described in Section 3.2.2 there is at least one additional charge ordering transition in this region, which is not affecting macroscopic or microscopic magnetisation at all. Surprising is that there is also no change in non-spin-flip channel observed. Although neutrons scatter at atomic cores, due to crystal distortion, charge ordering should also

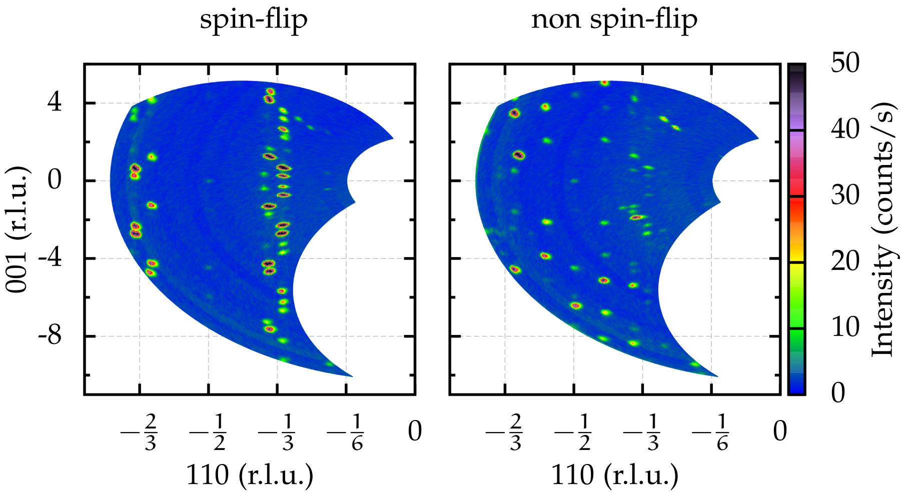

Figure 3.34: hhℓ-plane at 200 K in spin-flip (left) and non spin-flip (right) channel with magnetic field $\mathbf{H} \parallel z$.

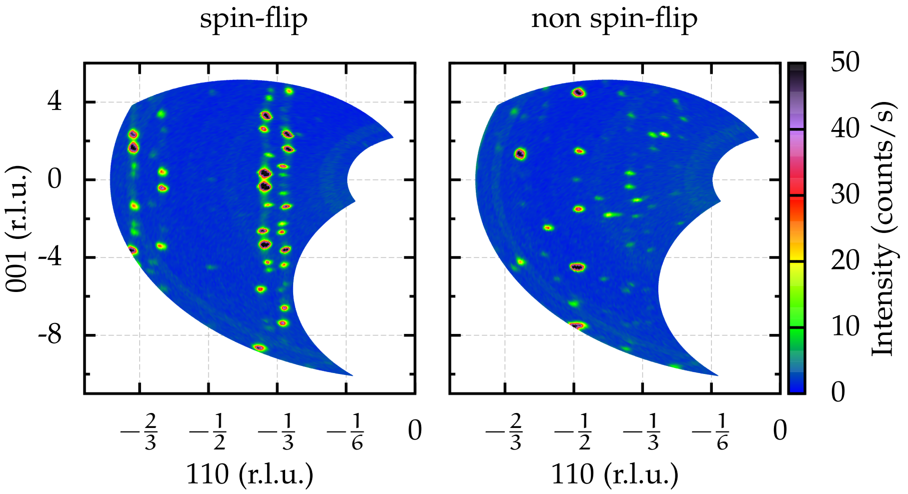

Figure 3.35: hhℓ-plane at 160 K in spin-flip (left) and non spin-flip (right) channel with magnetic field $\mathbf{H} \parallel z$.

be observable in neutron diffraction. One possible explanation could be sample varieties, but the x-ray diffraction experiments shown in Section 3.2.2, were repeated with a small part of the DNS sample with similar results.

To specify the moment direction also in the low temperature phase, one measurements with x-field at 160 K was done. Considering the possible different sample orientation (in the second beamtime), the measurement with z-field was repeated at this temperature.

Cooling below the Néel-Temperature the diffuse scattering vanishes in stoichiometric samples and 3D-magnetic ordering occurs (Fig. 3.34). Therefore beside intra-layer ordering there is also long-range correlation between different layers present. The hhℓ-pattern consists of peaks arranged on four lines along ℓ slightly incommensurate shifted from (-1/3, -1/3, ℓ) and (-2/3, -2/3, ℓ), the incommensurability is always

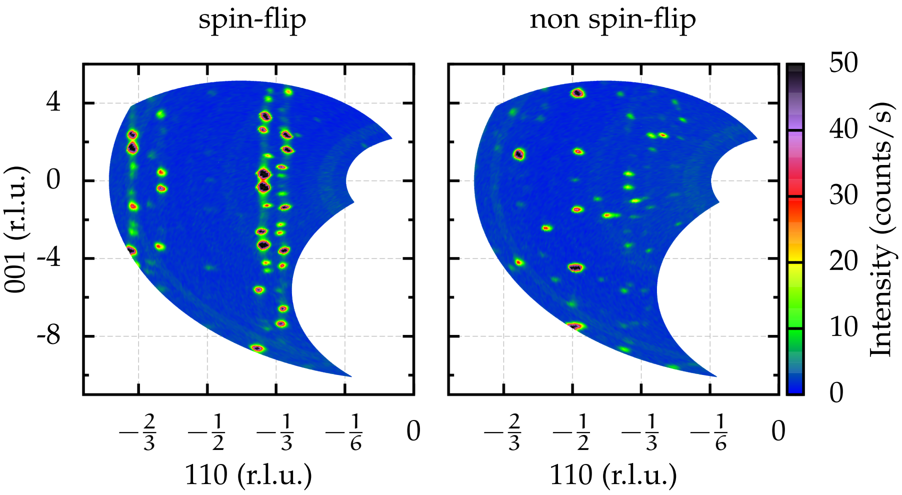

Figure 3.36: hhl-plane at 12 K in spin-flip (left) and non spin-flip (right) channel with magnetic field $\mathbf{H} \parallel z$.

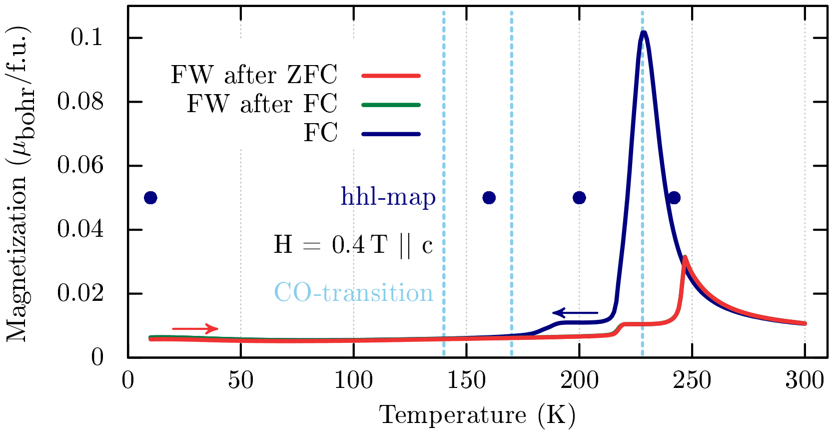

Figure 3.37: Magnetisation of sample Z8G5_S1, the blue dot marks position at which full hhℓ-maps were measured at the DNS experiment, while the light blue lines are roughly the charge ordering transitions.

smaller than 0.03 r.l.u... This is completely different to results on non-stoichiometric $YFe_2O_{4-\delta}$ single crystals from Funahashi et al., where magnetic scattering stays two-dimensional down to 9 K [34]. The origin of the strong intensity variations between different reflections on the same line is not understood. The formation of multiple domains, which all contribute to the observed pattern, as it was suggested for the charge ordering in $LuFe_2O_4$ in [90], could explain partially such variations.

The shifting of these lines from the (0 0 ℓ)-line is strongly temperature dependent. Fig. 3.39 shows profiles of the along ℓ integrated intensity in dependence of the hh0-position for different temperatures measured during warming. The local maxima in the integrated intensities were fitted with Gaussian functions, for all temperatures

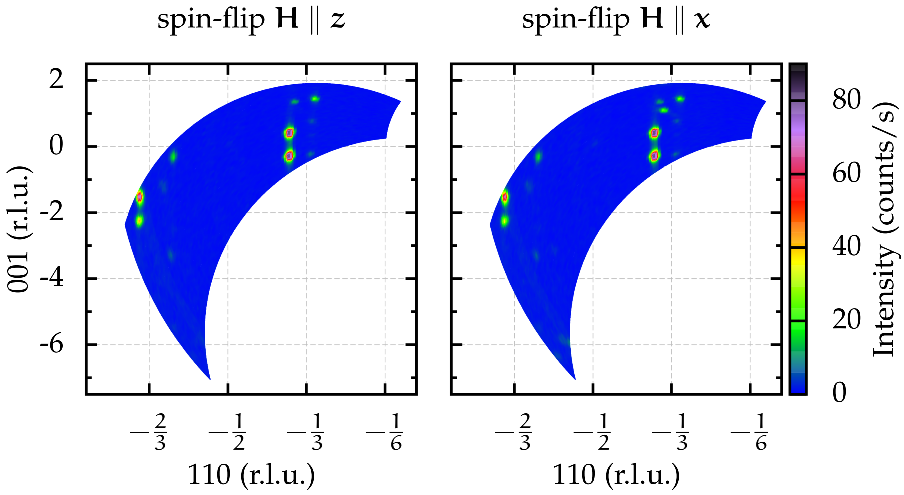

Figure 3.38: $hh\ell$-plane at 160 K on cooling in spin-flip channel with magnetic field $\mathbf{H} \parallel z$ (left) and $\mathbf{H} \parallel x$ (right) — counting time: 15 s — five detector bank positions.

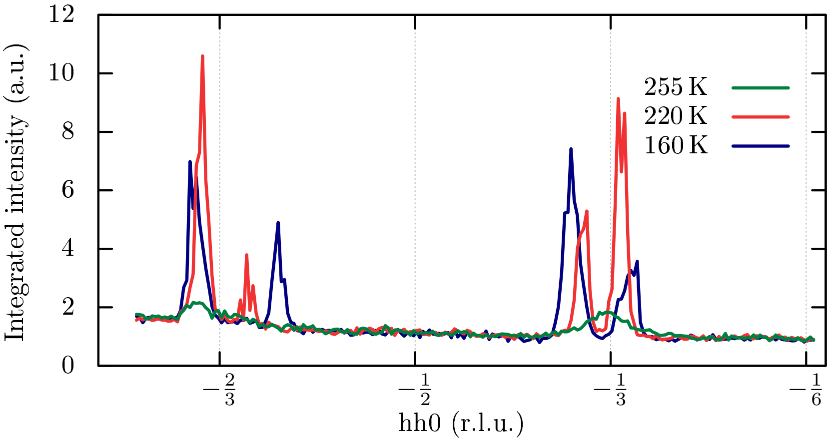

Figure 3.39: Along ℓ integrated intensity at 160 K, 220 K and 255 K, all measured during warming.

marked in Fig. 2.12, to receive the $hh0$ position of the maxima. These positions are shown in dependence of the temperature (on the y-scale) for the $(^1/_3\ ^1/_3\ \ell)$-region in Fig. 3.40 and for the $(^2/_3\ ^2/_3\ \ell)$-region in Fig. 3.41. For temperatures above 240 K on cooling and 255 K on warming only diffuse scattering along $(^1/_3\ ^1/_3\ \ell)$ is observed, hysteretic behaviour therefore vanishes above 255 K. Below this temperature the incommensurability of the $hh0$-position is linked to the hysteretic temperature dependence of the two step transition in the macroscopic magnetization.

In the state with diffuse scattering, switching the neutron polarization parallel to x and therefore parallel to the average $\mathbf{Q}$, leads to higher intensity of the diffuse scattering in spin flip channel, and reduced intensity in non-spin-flip channel. In contrast in the three-dimensional ordered phase at 160 K, there is no increase in intensity in the strongest reflections, while changing the field direction from z to x, as shown in Figure 3.38. Therefore in the ordered phase the magnetic moment is aligned parallel c building an real Ising spin system, as it is also in $LuFe_2O_4$, where there was, already before de Groot [66] determined the ferrimagnetic and an antiferromagnetic spin configuration, a strong consensus that $LuFe_2O_4$is an ideal Ising spin system with hexagonal **c**-axis as easy axis [45, 78, 98–102].

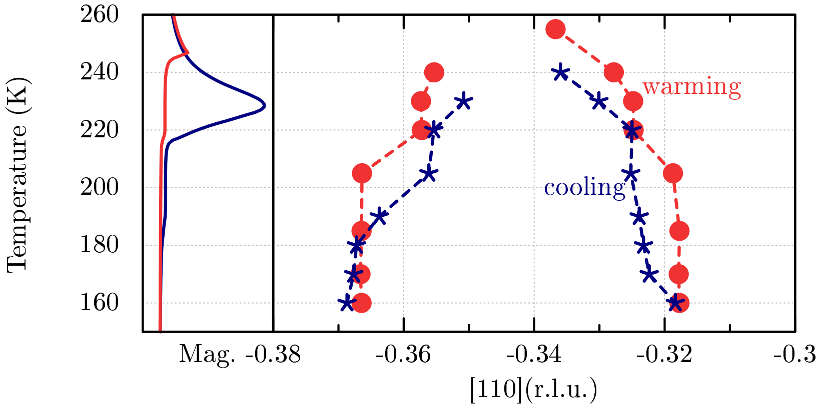

Figure 3.40: Temperature dependence of magnetic superstructure peak position in the (1/3 1/3 ℓ)-region — the points correspond to maxima in the, along ℓ integrated, intensity. An example of the integrated intensity profiles is shown in Fig. 3.39.

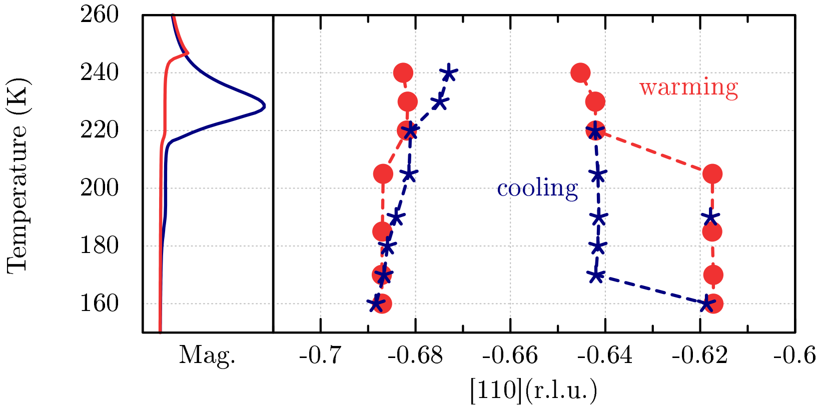

Figure 3.41: Temperature dependence of magnetic superstructure peak position in the (2/3 2/3 ℓ)-region — the points correspond to maxima in the, along ℓ integrated, intensity. An example of the integrated intensity profiles is shown in Fig. 3.39.

3.3.3 *X-ray magnetic circular dichroism*

The X-ray magnetic circular dichroism signal is the difference between x-ray absorption spectra of circular left and right polarized light, measured in a magnetic field [103].

The XMCD process can after [11, 104] be describe as followed: A left or right circularly polarized photon excites a photoelectron from a 2p state. The spin of the photoelectron depends on the polarization direction of the x-ray beam. Now the photoelectron is captured into an empty 3d valence state. If some of the 3d states are occupied with electrons, the transition probability will become different for electrons excited by left or right polarized light. Because the transition probability is proportional to the free 3d states with spin parallel to the spin of the photoelectron. By measuring the x-ray absorption spectra $\mu_{\pm}$ for left and right circular polarized light one can calculate the XMCD signal as $\Delta\mu = \mu_{+} - \mu_{-}$.

By so called sum rules [105] it is possible to get quantitative informations out of the XMCD signal, for example the ration between orbital moment and spin moment.

Our XMCD experiment at 4-ID-C C of the Advanced Photon Source (APS) was dedicated to the charge-spin coupling in $LuFe_2O_4$ the results can be found in [8, 11] and are in principle similar to [106]. We used the beamtime also to measure XMCD spectra on $YFe_2O_{4-\delta}$ samples from the third Z3 and second growth Z2. These samples were later be found to show a macroscopic magnetization of non-stoichiometric Type C and no long-range three-dimensional charge or spin order. Since the XMCD signal in $LuFe_2O_4$ shows almost no variation between stoichiometric [8] and non-stoichiometric samples [100, 106], the results on non-stoichiometric $YFe_2O_{4-\delta}$ are still interesting.

The XMCD signal for the sample from the second growth can be found in Figure 3.42, together with both x-ray absorption spectra for left and right polarized light. The x-ray absorption spectra looks in general the same as for $LuFe_2O_4$ [8], with split L3 peak with contributions from Fe^{3+} and Fe^{3+}.

The resulting XMCD signal differs strongly from $LuFe_2O_4$ which is not surprising, since the charge and spin order differs and the XMCD signal in $LuFe_2O_4$ at 120 K originates from the ferrimagnetic phase, which is not present in $YFe_2O_{4-\delta}$. This is also the reason why the XMCD signal in $YFe_2O_{4-\delta}$ is much weaker than in $LuFe_2O_4$. The XMCD signal in $YFe_2O_{4-\delta}$ is therefore in contrast to $LuFe_2O_4$ completely field induced and the XMCD signal is proportional to the magnetization which is at 4 T (Fig. 3.17) not saturated and more than a factor of 10 smaller at 120 K than in $LuFe_2O_4$ [11].

Since the statistical fluctuations in the XMCD signal in $LuFe_2O_4$were found to be strong, applying sum rules to the XMCD spectra in

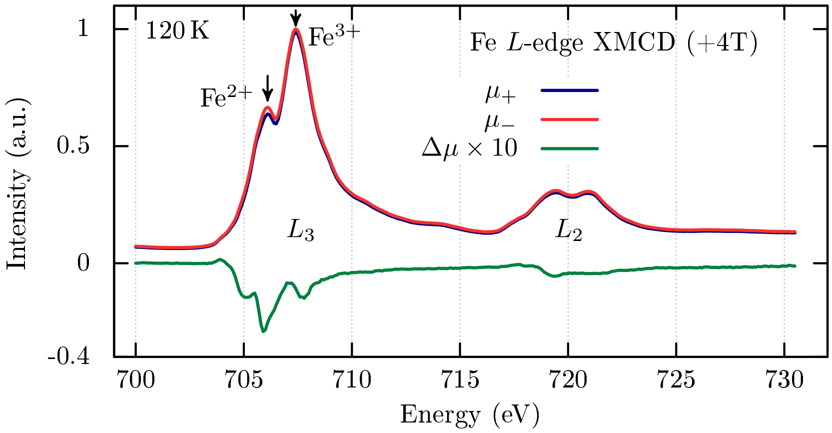

Figure 3.42: XAS spectra for left and right circularly polarized light over the Fe L-edge at 120 K for sample Z2 and XMCD signal. All received from total electron yield.

$YFe_2O_{4-\delta}$ is not a promising idea and is therefore not shown here. In contrast to $LuFe_2O_4$ [8] $YFe_2O_{4-\delta}$ shows no positive XMCD signal at the Fe^{3+} position, this is in accordance with [26], were the positive peak is strongly repressed in the substituted composition $Lu_{0.5}Y_{0.5}Fe_2O_4$. The shown x-ray absorption signal is based on total electron yield and the same signal from fluorescence can be found in Figure 3.43.

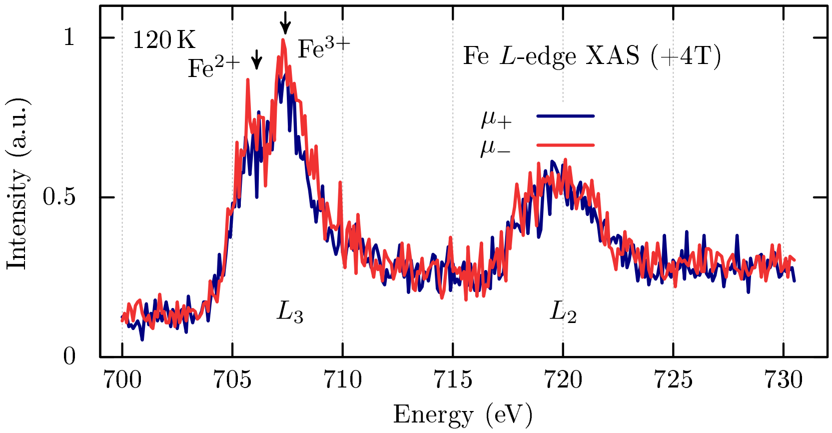

Figure 3.43: XAS spectra for left and right circularly polarized light over the Fe L-edge at 120 K. Measured with fluorescence detector.

The difference hight of the Fe^{3+} and Fe^{3+} peaks in 3.42 is weaker in the fluorescence measurement and therefore partially a surface effect. The XMCD signal for the sample from the second growth can be found in Fig.3.44. The difference between the Fe^{3+} and Fe^{3+} peaks is also smaller in sample Z3 which indicates a more balanced contribution of both valances, therefore a smaller δ in $YFe_2O_{4-\delta}$, this tendency is in accordance with the oxygen partial pressures during growth.

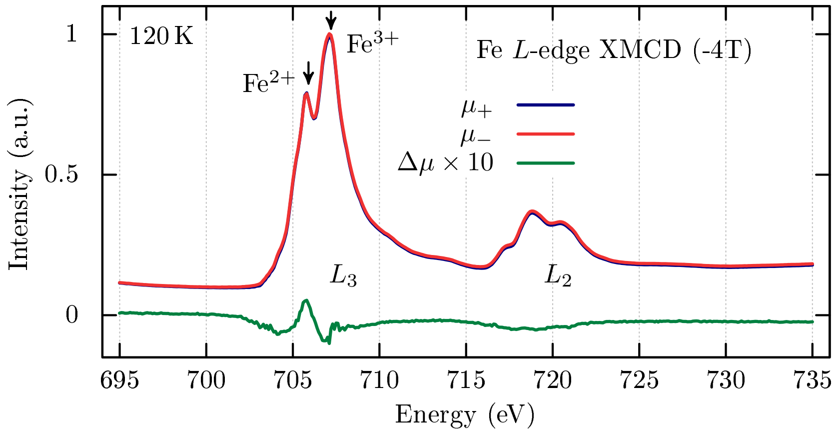

Figure 3.44: XAS spectra for left and right circularly polarized light over the Fe L-edge at 120 K for sample Z3 and XMCD signal. All received from total electron yield.

4

CONCLUSION AND OUTLOOK

4.1 CONCLUSION

We have grown $YFe_2O_{4-\delta}$ single crystals showing for the first time the magnetic behaviour of stoichiometric powder samples, i.e. a two step antiferromagnetic phase transition as show in Figure 3.14. The transition temperatures show a huge thermal hysteresis while the higher transition is at $T_h^w = 248\,\mathrm{K}$ on warming and $T_h^c = 228\,\mathrm{K}$ on cooling which are also the Néel temperatures, the lower transition is a broad dip in magnetization and lays at $T_l^w = 215\,\mathrm{K}$ on warming and $T_l^c = 185\,\mathrm{K}$ on cooling. The magnetization of our sample is equal to the one for which Inazumi [18] specified the an oxygen deficit as $\delta = 0.00$. As a upper limit for the oxygen deficit in our sample we can give $\delta = 0.031$, samples with this deficit in [18] show a clear parasitic ferrimagnetism, in contrast to our sample.

In contrast to non-stoichiometric samples where charge ordering stays two-dimensional down to 100 K, our sample shows complex three-dimensional charge ordered phases below the Néel temperature. We could identify six different charge ordered phases, while diffuse scattering along reciprocal $(^1/_3\ ^1/_3\ \ell)$ line is observed above the Néel temperature, at 200 K the pattern is dominated by superstructure with propagation vector $\mathbf{Q} = (^1/_7{+}\tau\ \ ^1/_7{+}\tau\ \ ^9/_7)$. Cooling further below the second transition in magnetization the superstructure transforms in the only commensurate phase observed with $\mathbf{Q} = (^1/_4\ ^1/_4\ ^3/_4)$. Both phases were also observed in electron diffraction but in different temperature ranges [7, 41, 83, 84]. At 100 K another more complex pattern is observed, which is surprisingly but in coherence with [35, 88], replaced at 37 K by the same diffuse lines observed at room temperature. At 10 K we observed in one sample ($^1/_3\ ^1/_3$ half-integer) reflections, which would correspond to the low temperature phase of $LuFe_2O_4$ [66, 90].

Through full polarization analysis on resonant features in the x-ray diffraction over the Fe K-edge at PETRA III P09, we found weak anisotropies, which might indicate some kind of orbital order. In $LuFe_2O_4$ such an anisotropic contribution was excluded through full polarization analysis [11].

During our 4-ID-C XMCD experiment on $LuFe_2O_4$, from which the results are already published [8], we measured also two x-ray magnetic circular dichroism signals on $YFe_2O_{4-\delta}$ at the Fe L_3 and L_2 edge. The samples were non-stoichiometric, through the experiment was at the beginning of this thesis. The XMCD signal is different to $LuFe_2O_4$ which is not surprising, since charge ordering and spin ordering are totally different. Also the XMCD signal in $LuFe_2O_4$ at 120 K originates from the ferrimagnetic phase, which is not present in $YFe_2O_{4-\delta}$, which is antiferromagnetic at 120 K.

Our samples show in neutron diffraction at DNS at FRM II, also for the first time in $YFe_2O_{4-\delta}$single crystals, three-dimensional spin ordering, which is in contrast to the two-dimensional spin ordering observed in non-stoichiometric samples in [16, 19, 34]. Diffuse magnetic scattering along ($1/3$ $1/3$ ℓ) is observed in stoichiometric $YFe_2O_{4-\delta}$ above the Néel temperature (Figure 3.32), originating from random stacking of the still magnetically ordered trigonal layers. This is the same as in $LuFe_2O_4$ [66]. Below the Néel temperature complex three-dimensional ordering occurs indicating long range interlayer spin ordering. This pattern varies while cooling through the lower transition in macroscopic magnetization and shows no further variations down to 10 K. Both patterns consist of peaky lines slightly incommensurate shifted from ($1/3$ $1/3$ ℓ), the incommensurability shows the same thermal hysteresis as macroscopic magnetization.

The primary goal of this thesis was to grow stoichiometric single crystals of $YFe_2O_{4-\delta}$ which has been tried for over 30 years [14, 84]. This goal was achieved and we have grown stoichiometric single crystals of $YFe_2O_{4-\delta}$, with magnetic properties comparable to highest quality powder samples. This allowed us to continue with different x-ray and neutron diffraction studies on stoichiometric $YFe_2O_{4-\delta}$ which are a significant and original contribution to the investigation of $YFe_2O_{4-\delta}$ and the RFe_2O_4 system in general.

4.2 OUTLOOK

All three-dimensional charge orders as well as the spin orders, are not understood and determination of charge and spin structure in $YFe_2O_{4-\delta}$ is the most challenging part for future work. To determine the spin structure further neutron diffraction experiments with better resolution and the possibility to reach arbitrary reflections easily, without remounting and reorientating the crystals as it has to be done on DNS for different planes, would be beneficial. In the case of x-ray diffraction a single domain non twinned crystal could be the key to solve the structure.

From modelling the near edge resonant signal in the x-ray diffraction over the Fe K-edge in $YFe_2O_{4-\delta}$ one could receive the chemical shift between different Fe ions in $YFe_2O_{4-\delta}$, as it was done for $LuFe_2O_4$ in [60].

Resonant soft x-ray diffraction on the Fe $L_{2/3}$-edges may be better to probe electronic properties than the experiment at the Fe K-edge, where the polarization analysis mainly probed the structure, due to weak resonances.

Mössbauer spectroscopy would be the best technique to measure the oxygen deficit in our crystals, since the mean iron valence of 2.5 in YFe_2O_4 originates from equal parts of Fe^{3+} and Fe^{2+} which can easily be distinguished in the by Mössbauer spectrum. This was done on powder samples [18, 22, 81, 107].

To understand the differences between $YFe_2O_{4-\delta}$ and $LuFe_2O_4$ which should only originate from an ion sizing effect, since Y is larger than Lu, substitutions $Lu_{(1-x)}Y_xFe_2O_4$ would be helpful. This was already done, but without addressing stoichiometry [23–26].

Intensive XMCD measurements on stoichiometric samples, with higher statistics, could reveal correlations between spin, charge and orbital order.

It may be possible to optimize the crystal growth process to receive a stoichiometric crystals from the last grown part. At the moment the decomposition process and the slow cooling seem to be essential for achieving stoichiometric crystals.

Dielectric measurements on stoichiometric samples are very interesting for the question of ferroelectricity in $YFe_2O_{4-\delta}$, like they are reported for $LuFe_2O_4$ in [9, 10]

If ferroelectricity in $YFe_2O_{4-\delta}$ exists, magnetic measurements in electric field would be interesting to reveal a possible magnetoelectric coupling.

BIBLIOGRAPHY

[1] G. Moore, "Progress in digital integrated electronics," in *Electron Devices Meeting, 1975 International*, Vol. 21 (1975) pp. 11–13.

[2] C. Walter, "Kryder's Law," Scientific American (2005).

[3] D. Khomskii, "Classifying multiferroics: Mechanisms and effects," Physics **2**, 20 (2009).

[4] N. A. Spaldin and M. Fiebig, "The Renaissance of Magnetoelectric Multiferroics," Science **309**, 391 (2005).

[5] N. A. Hill, "Why Are There so Few Magnetic Ferroelectrics?" The Journal of Physical Chemistry B **104**, 6694 (2000).

[6] H. Schmid, "Some symmetry aspects of ferroics and single phase multiferroics *," J. Phys.: Condens. Matter **20**, 434201 (2008).

[7] N. Ikeda, R. Mori, S. Mori, and K. Kohn, "Structure Transition and Charge Competition on YFe_2O_4," Ferroelectrics **286**, 175 (2003).

[8] J. de Groot, T. Mueller, R. A. Rosenberg, D. J. Keavney, Z. Islam, J.-W. Kim, and M. Angst, "Charge Order in $LuFe_2O_4$: An Unlikely Route to Ferroelectricity," Phys. Rev. Lett. **108**, 187601 (2012).

[9] D. Niermann, F. Waschkowski, J. de Groot, M. Angst, and J. Hemberger, "Dielectric properties of charge ordered $LuFe_2O_4$ revisited: The apparent influence of contacts," ArXiv e-prints accepted for publication in PRL (2012), arXiv:1203.1200 [cond-mat.str-el] .

[10] A. Ruff, S. Krohns, F. Schrettle, V. Tsurkan, P. Lunkenheimer, and A. Loidl, "Absence of polar order in LuFe2O4," eprint arXiv:1204.1244 (2012), arXiv:1204.1244 [cond-mat.str-el] .

[11] J. de Groot, *Charge, spin and orbital order in the candidate multiferroic material* $LuFe_2O_4$, Ph.D. thesis, RWTH Aachen (2012).

[12] N. Kimizuka and T. Katsura, "Standard free energy of formation of $YFeO_3$, $Y_3Fe_5O_{12}$, and a new compound YFe_2O_4 in the Fe—Fe_2O_3—Y_2O_3 system at 1200°C," J. Solid State Chem. **13**, 176 (1975).

[13] K. Kitayama, M. Sakaguchi, Y. Takahara, H. Endo, and H. Ueki, "Phase equilibrium in the system Y-Fe-O at 1100°C," J. Solid State Chem. **177**, 1933 (2004).

[14] I. Shindo, N. Kimizuka, and S. Kimura, "Growth of YFe_2O_4 single crystals by floating zone method," Mater. Res. Bull. **11**, 637 (1976).

[15] T. Sugihara, K. Siratori, I. Shindo, and T. Katsura, "Parasitic Ferrimagnetism of YFe_2O_4," J. Phys. Soc. Jpn. **45**, 1191 (1978).

[16] J. Akimitsu, Y. Inada, K. Siratori, I. Shindo, and N. Kimizuka, "Two-dimensional spin ordering in YFe_2O_4," Solid State Commun. **32**, 1065 (1979).

[17] Y. Nakagawa, M. Inazumi, N. Kimizuka, and K. Siratori, "Low-Temperature Phase Transitions and Magnetic Properties of YFe_2O_4," J. Phys. Soc. Jpn. **47**, 1369 (1979).

[18] M. Inazumi, Y. Nakagawa, M. Tanaka, N. Kimizuka, and K. Siratori, "Magnetizations and Mössbauer Spectra of YFe_2O_{4-x}," J. Phys. Soc. Jpn. **50**, 438 (1981).

[19] S. Funahashi, J. Akimitsu, K. Siratori, N. Kimizuka, M. Tanaka, and H. Fujishita, "Two-Dimensional Spin Correlation in YFe_2O_4," J. Phys. Soc. Jpn. **53**, 2688 (1984).

[20] Y. Matsui, "Extra Electron Reflections Observed In YFe_2O_4, $YbFe_2O_2$, $Yb_2Fe_3O_7$ and $Yb_3Fe_4O_{10}$," J. Appl. Crystallogr. **13**, 395 (1980).

[21] M. Tanaka, J. Akimitsu, Y. Inada, N. Kimizuka, I. Shindo, and K. Siratori, "Conductivity and specific heat anomalies at the low temperature transition in the stoichiometric YFe_2O_4," Solid State Commun. **44**, 687 (1982).

[22] M. Tanaka, M. Kato, N. Kimizuka, and K. Siratori, "Mössbauer Study of Stoichiometric YFe_2O_4," J. Phys. Soc. Jpn. **47**, 1737 (1979).

[23] M. Kishi, Y. Nakagawa, M. Tanaka, N. Kimizuka, and I. Shindo, "Low-temperature Transitions of RFe_2O_4," J. Magn. Magn. Mater. **31-4**, 807 (1983).

[24] K. Siratori, N. Môri, H. Takahashi, G. Oomi, J. Iida, M. Tanaka, M. Kishi, Y. Nakagawa, and N. Kimizuka, "Effect of the Pressure and the Rare-Earth Substitution on the Verwey Transition of YFe_2O_4," J. Phys. Soc. Jpn. **59**, 631 (1990).

[25] C. R. Serrao, J. R. Sahu, K. Ramesha, and C. N. R. Rao, "Magnetoelectric effect in rare earth ferrites, $LnFe_2O_4$," J. Appl. Phys. **104**, 016102 (2008).

[26] H. J. Noh, H. Sung, J. Jeong, J. Jeong, S. B. Kim, J. Y. Kim, J. Y. Kim, and B. K. Cho, "Effect of structural distortion on ferrimagnetic order in $Lu_{(1-x)}L_{(x)}Fe_{(2)}O_{(4)}$ (L=Y and Er; x=0.0, 0.1, and 0.5)," Phys. Rev. B **82**, 024423 (2010).

[27] A. Enomura, S. Asai, Y. Ishiwata, T. Inabe, Y. Sakai, N. Tsuda, M. Tanaka, and K. Siratori, "Seebeck Coefficient of YFe_2O_4," J. Phys. Soc. Jpn. **52**, 4286 (1983).

[28] Y. Sakai, K. Kaneda, N. Tsuda, M. Tanaka, and K. Siratori, "Seebeck Coefficient of YFe_2O_4 at Lower Transition Temperature," J. Phys. Soc. Jpn. **54**, 4089 (1985).

[29] J. Iida, S. Kakugawa, G. Kido, Y. Nakagawa, S. Takekawa, and N. Kimizuka, "High field magnetization of single crystals YFe_2O_4, $YbFe_2O_4$ and $LuFe_2O_4$," Physica B: Condensed Matter **155**, 307 (1989).

[30] M. Mekata, "Antiferro-Ferrimagnatic Transition in Triangular Ising Lattice," J. Phys. Soc. Jpn. **42**, 76 (1977).

[31] T. Matsumoto, N. Môri, J. Iida, M. Tanaka, and K. Siratori, "Magnetic Properties of the Two Dimensional Antiferromagnets RFe_2O_4 (R=Y, Er) at High Pressure," J. Phys. Soc. Jpn. **61**, 2916 (1992).

[32] T. Matsumoto, N. Môri, J. Iida, M. Tanaka, K. Siratori, F. Izumi, and H. Asano, "Crystal structures of the two dimensional antiferromagnets RFe_2O_4 (R = Y, Er) and their magnetic properties under pressure," Physica B: Condensed Matter **180-181, Part 2**, 603 (1992).

[33] S. Katano, T. Matsumoto, S. Funahashi, J. Iida, M. Tanaka, and J. Cable, "Crystal and magnetic structure of stoichiometric YFe_2O_4," Physica B: Condensed Matter **213-214**, 218 (1995).

[34] S. Funahashi, Y. Morii, and H. R. Child, "Two-dimensional neutron diffraction of YFe_2O_4 and $CoCr_2O_4$," J. Appl. Phys. **61**, 4114 (1987).

[35] N. Ikeda, R. Mori, K. Kohn, M. Mizumaki, and T. Akao, "Dielectric and Structure Properties of Charge Competing System YFe_2O_4," Ferroelectrics **272**, 309 (2002).

[36] Y. Horibe, K. Kishimoto, S. Mori, and N. Ikeda, "Dielectric Anomaly and Structural Phase Transitions in $YFe_2O_{4-\delta}$," Integr. Ferroelectr. **67**, 151 (2004).

[37] Y. Sakai, K. Kaneda, N. Tsuda, and M. Tanaka, "Electrical Resistivity of YFe_2O_4," J. Phys. Soc. Jpn. **55**, 3181 (1986).

[38] B. Fisher, J. Genossar, L. Patlagan, and G. M. Reisner, “Electronic transport and I-V characteristics of polycrystalline $LuFe_2O_4$,” J. Appl. Phys. **109**, 084111 (2011).

[39] Y. Horibe, K. Kishimoto, S. Mori, and N. Ikeda, “Nano-sized domains related to dielectric anomaly in $YFe_2O_{4-\delta}$,” J. Electron Microsc. **54**, i87 (2005).

[40] S. Mori, S. Shinohara, Y. Matsuo, Y. Horibe, K. Yoshii, and N. Ikeda, “Effect of Oxygen Vacancies on Charge Ordered Structure in $YFe_2O_{4-\delta}$,” Jpn. J. Appl. Phys. **47**, 7595 (2008).

[41] Y. Horibe, K. Yoshii, N. Ikeda, and S. Mori, “Oxygen-deficient effect on charge ordering in spin- and charge-frustrated ferrite $YFe_2O_{4-\delta}$,” Phys. Rev. B **80**, 092104 (2009).

[42] W. Piekarczyk, W. Wepper, and A. Rabenau, “Solid State Electrochemical Study of Phase Equilibria and Thermodynamics of the Ternary System Y-Fe-O at Elvated Temperatures,” Z. Naturforsch. **34a**, 430 (1979).

[43] A. L. Bail, H. Duroy, and J. Fourquet, “Ab-initio structure determination of $LiSbWO_6$ by X-ray powder diffraction,” Mater. Res. Bull. **23**, 447 (1988).

[44] V. Petricek, M. Dusek, and L. Palatinus, “Jana2006. The crystallographic computing system,” Institute of Physics, Praha, Czech Republic (2006).

[45] A. D. Christianson, M. D. Lumsden, M. Angst, Z. Yamani, W. Tian, R. Jin, E. A. Payzant, S. E. Nagler, B. C. Sales, and D. Mandrus, “Three-Dimensional Magnetic Correlations in Multiferroic $LuFe_2O_4$,” Phys. Rev. Lett. **100**, 107601 (2008).

[46] J. Iida, S. Takekawa, and N. Kimizuka, “Single crystal growth of $LuFe_2O_4$, $LuFeCoO_4$ and $YbFeMgO_4$ by the floating zone method,” J. Cryst. Growth **102**, 398 (1990).

[47] “`http://www.chem.agilent.com/en-US/Products/Instruments/x-raycrystallography/smallmoleculesystem/supernova/Pages/default.aspx`,” (2012).

[48] “`http://www.chem.agilent.com/en-US/Products/Instruments/x-raycrystallography/accessories/cryojetht/pages/default.aspx`,” (2012).

[49] “`http://www.chem.agilent.com/en-US/Products/Instruments/x-raycrystallography/accessories/helijet/pages/default.aspx`,” (2012).

[50] “`http://www.chem.agilent.com/en-US/Products/Software/x-ray/crysalis/Pages/default.aspx`,” (2012).

[51] L. J. Farrugia, "*WinGX* suite for small-molecule single-crystal crystallography," J. Appl. Crystallogr. **32**, 837 (1999).

[52] G. M. Sheldrick, "A short history of *SHELX*," Acta Crystallogr. Sect. A **64**, 112 (2008).

[53] A. Altomare, G. Cascarano, C. Giacovazzo, A. Guagliardi, M. C. Burla, G. Polidori, and M. Camalli, "*SIR*92 – a program for automatic solution of crystal structures by direct methods," J. Appl. Crystallogr. **27**, 435 (1994).

[54] H. Schenk, "An introduction to direct methods http://www.iucr.org/education/pamphlets/17," .

[55] C. Giacovazzo, "Quintets in *P*1 and related phase relationships: a probabilistic approach," Acta Crystallogr. Sect. A **33**, 944 (1977).

[56] C. Giacovazzo, "The method of representations of structure seminvariants. II. New theoretical and practical aspects," Acta Crystallogr. Sect. A **36**, 362 (1980).

[57] W. Massa, *Kristallstrukturbestimmung*, edited by H. H. Christoph Elschenbroich, Friedrich Hensel (STUDIUM Vieweg+Teubner, 2009).

[58] J. Strempfer, "Anomalous and Resonant X-ray Scattering: Spin, charge and orbital order," in *Lecture Notes of the 43rd IFF Spring School "Scattering Methods for Condensed Matter Research: Towards Novel Applications at Future Sources" Schriften des Forschungszentrums Jülich . Reihe Schlüsseltechnologien / Key Technologies*, Vol. 33, edited by M. Angst, T. Brückel, D. Richter, and R. Zorn (Forschungszentrum Jülich GmbH Zentralbibliothek, Verlag, 2012) Chap. D11.

[59] G. Materlik, C. J. Sparks, and K. Fischer, eds., *Resonant anomalous X-ray scattering: Theory and Applications* (Elsevier Science B.V., 1994).

[60] A. M. Mulders, S. M. Lawrence, U. Staub, M. Garcia-Fernandez, V. Scagnoli, C. Mazzoli, E. Pomjakushina, K. Conder, and Y. Wang, "Direct Observation of Charge Order and an Orbital Glass State in Multiferroic $LuFe_2O_4$," Phys. Rev. Lett. **103**, 077602 (2009).

[61] C. Mazzoli, S. B. Wilkins, S. Di Matteo, B. Detlefs, C. Detlefs, V. Scagnoli, L. Paolasini, and P. Ghigna, "Disentangling multipole resonances through a full x-ray polarization analysis," Phys. Rev. B **76**, 195118 (2007).

[62] C. Detlefs, M. Sanchez del Rio, and C. Mazzoli, "X-ray polarization: General formalism and polarization analysis," (2011), arXiv:1106.4446 [cond-mat.str-el] .

[63] J. Strempfer, "`http://hasylab.desy.de/facilities/petra_iii/beamlines/p09_resonant_scattering_and_diffraction/beamline_layout/index_eng.html`," .

[64] T. Brückel, G. Heger, D. Richter, G. Roth, and R. Zorn, *Neutron Scattering Experiment Manuals of the JCNS Laboratory Course (2011) Schriften des Forschungszentrums Jülich . Reihe Schlüsseltechnologien / Key Technologies 28* (Forschungszentrum Jülich GmbH Zentralbibliothek, Verlag, 2010).

[65] W. Schweika, "Polarized neutron scattering and polarization analysis," in *Lectures of the JCNS Laboratory Course Schriften des Forschungszentrums Jülich . Reihe Schlüsseltechnologien / Key Technologies*, Vol. 15, edited by T. Brückel, G. Heger, D. Richter, G. Roth, and R. Zorn (Forschungszentrum Jülich GmbH Zentralbibliothek, Verlag, 2010) Chap. 6.

[66] J. de Groot, K. Marty, M. D. Lumsden, A. D. Christianson, S. E. Nagler, S. Adiga, W. J. H. Borghols, K. Schmalzl, Z. Yamani, S. R. Bland, R. de Souza, U. Staub, W. Schweika, Y. Su, and M. Angst, "Competing Ferri- and Antiferromagnetic Phases in Geometrically Frustrated $LuFe_2O_4$," Phys. Rev. Lett. **108**, 037206 (2012).

[67] A. Dianoux and G. Lander, eds., *Neutron Data Booklet* (Institute Laue-Langevin, 2003).

[68] S. Disch, *The spin structure of magnetic nanoparticles and in magnetic nanostructures*, Ph.D. thesis, Forschungszentrum Jülich (2011).

[69] G. Bergerhoff and I. Brown, in *Crystallographic Databases*, edited by F. A. et al. (International Union of Crystallography, Chester, 1987).

[70] A. C. Thompson and D. Vaughan, eds., *X-ray Data Booklet*, 2nd ed. (Lawrence Berkeley National Laboratory, University of California, 2001).

[71] D. Du Boulay, E. N. Maslen, V. A. Streltsov, and N. Ishizawa, "A synchrotron X-ray study of the electron density in $YFeO_3$," Acta Crystallogr. Sect. B **51**, 921 (1995).

[72] E. J. W. Verwey, "Electronic Conduction of Magnetite (Fe_3O_4) and its Transition Point at Low Temperatures," Nature **144**, 327 (1939).

[73] K. Conder, "Oxygen diffusion in the superconductors of the YBaCuO family: isotope exchange measurements and models," Mater. Sci. Eng. R **32**, 41 (2001).

[74] A. Nemudry, M. Weiss, I. Gainutdinov, V. Boldyrev, and R. Schöllhorn, "Room Temperature Electrochemical Redox Reactions of the Defect Perovskite $SrFeO_{2.5+x}$," Chem. Mater. **10**, 2403 (1998).

[75] T. Sekine and T. Katsura, "Phase equilibria in the system Fe–Fe_2O_3–Lu_2O_3 at 1200° C," J. Solid State Chem. **17**, 49 (1976).

[76] J. Bourgeois, M. Hervieu, M. Poienar, A. M. Abakumov, E. Elkaïm, M. T. Sougrati, F. Porcher, F. Damay, J. Rouquette, G. Van Tendeloo, A. Maignan, J. Haines, and C. Martin, "Evidence of oxygen-dependent modulation in $LuFe_2O_4$," Phys. Rev. B **85**, 064102 (2012).

[77] J. de Groot, "private communication," .

[78] F. Wang, J. Kim, Y.-J. Kim, and G. D. Gu, "Spin-glass behavior in $LuFe_2O_{4+\delta}$," Phys. Rev. B **80**, 024419 (2009).

[79] D. S. F. Viana, R. A. M. Gotardo, L. F. Cotica, I. A. Santos, M. Olzon-Dionysio, S. D. Souza, D. Garcia, J. A. Eiras, and A. A. Coelho, "Ferroic investigations in $LuFe_2O_4$ multiferroic ceramics," J. Appl. Phys. **110**, 034108 (2011).

[80] J. Iida, Y. Nakagawa, and N. Kimizuka, "High field magnetization of single crystals YFe_2O_4, $YbFe_2O_4$ and $LuFe_2O_4$," J. Phys. Soc. Jpn. **55**, 1434 (1986).

[81] T. Sugihara, M. Abe, and T. Katsura, "Magnetic and Mössbauer Studies of a New Compound YFe_2O_4," J. Phys. Soc. Jpn. **40**, 1211 (1976).

[82] T. C. Ozawa and S. J. Kang, "*Balls&Sticks*: easy-to-use structure visualization and animation program," J. Appl. Crystallogr. **37**, 679 (2004).

[83] N. Ikeda, H. Ohsumi, M. Mizumaki, S. Mori, Y. Horibe, and K. Kishimoto, "Frustration and ordering of iron ions on triangular iron mixed valence system RFe_2O_4," J. Magn. Magn. Mater. **272-276**, , Supplement E1037 (2004), proceedings of the International Conference on Magnetism (ICM 2003).

[84] Y. Horibe, N. Ikeda, K. Yoshii, and S. Mori, "Direct observation of low-temperature superstructure in spin- and charge-frustrated ferrite $YFe_2O_{4-\delta}$," Phys. Rev. B **82**, 184119 (2010).

[85] A. J. Hearmon, D. Prabhakaran, H. Nowell, F. Fabrizi, M. J. Gutmann, and P. G. Radaelli, "Helical scattering signatures of strain and electronic textures in $YbFe_2O_4$ from three-dimensional reciprocal-space imaging," Phys. Rev. B **85**, 014115 (2012).

[86] Y. Zhang, H. X. Yang, C. Ma, H. F. Tian, and J. Q. Li, "Charge-Stripe Order in the Electronic Ferroelectric $LuFe_2O_4$," Phys. Rev. Lett. **98**, 247602 (2007).

[87] Y. Zhang, H. X. Yang, Y. Q. Guo, C. Ma, H. F. Tian, J. L. Luo, and J. Q. Li, "Structure, charge ordering and physical properties of $LuFe_2O_4$," Phys. Rev. B **76**, 184105 (2007).

[88] N. Ikeda, S. Mori, and K. Kohn, "Charge Ordering and Dielectric Dispersion in Mixed Valence Oxides RFe_2O_4," Ferroelectrics **314**, 41 (2005).

[89] Y. Yamada, S. Nohdo, and N. Ikeda, "Incommensurate Charge Ordering in Charge-Frustrated $\mathbf{LuFe_2O_4}$ System," J. Phys. Soc. Jpn. **66**, 3733 (1997).

[90] M. Angst, R. P. Hermann, A. D. Christianson, M. D. Lumsden, C. Lee, M. . H. Whangbo, J. . W. Kim, P. J. Ryan, S. E. Nagler, W. Tian, R. Jin, B. C. Sales, and D. Mandrus, "Charge Order in LuFe(2)O(4): Antiferroelectric Ground State and Coupling to Magnetism," Phys. Rev. Lett. **101**, 227601 (2008).

[91] Y. Yamada, K. Kitsuda, S. Nohdo, and N. Ikeda, "Charge and spin ordering process in the mixed-valence system LuFe2O4: Charge ordering," Phys. Rev. B **62**, 12167 (2000).

[92] S. M. Lawrence, *X-ray and neutron scattering of multiferroic $LuFe_2O_4$*, Ph.D. thesis, Curtin University (2011).

[93] A. Nagano and S. Ishihara, "Spin-charge-orbital structures and frustration in multiferroic RFe_2O_4," J. Phys.: Condens. Matter **19**, 145263 (2007).

[94] A. Nagano, M. Naka, J. Nasu, and S. Ishihara, "Electric Polarization, Magnetoelectric Effect, and Orbital State of a Layered Iron Oxide with Frustrated Geometry," Phys. Rev. Lett. **99**, 217202 (2007).

[95] S. Ishihara and S. Maekawa, "Theory of Anomalous X-Ray Scattering in Orbital-Ordered Manganites," Phys. Rev. Lett. **80**, 3799 (1998).

[96] O. Schärpf and H. Capellmann, "The XYZ-Difference Method with Polarized Neutrons and the Separation of Coherent, Spin Incoherent, and Magnetic Scattering Cross Sections in a Multidetector," physica status solidi (a) **135**, 359 (1993).

[97] W. Schweika, "XYZ-polarisation analysis of diffuse magnetic neutron scattering from single crystals," Journal of Physics: Conference Series **211**, 012026 (2010).

[98] J. Iida, M. Tanaka, Y. Nakagawa, S. Funahashi, N. Kimizuka, and S. Takekawa, "Magnetization and Spin Correlation of Two-Dimensional
Triangular Antiferromagnet $LuFe_2O_4$," J. Phys. Soc. Jpn. **62**, 1723 (1993).

[99] J. Iida, Y. Nakagawa, and N. Kimizuka, "Field-Heating Effect–Anomalous Thermomagnetization Curves Observed in Hexagonal $LuFe_2O_4$," J. Phys. Soc. Jpn. **55**, 1434 (1986).

[100] K.-T. Ko, H.-J. Noh, J.-Y. Kim, B.-G. Park, J.-H. Park, A. Tanaka, S. B. Kim, C. L. Zhang, and S.-W. Cheong, "Electronic Origin of Giant Magnetic Anisotropy in Multiferroic $LuFe_2\mathbf{O}_4$," Phys. Rev. Lett. **103**, 207202 (2009).

[101] W. Wu, V. Kiryukhin, H.-J. Noh, K.-T. Ko, J.-H. Park, W. Ratcliff, P. A. Sharma, N. Harrison, Y. J. Choi, Y. Horibe, S. Lee, S. Park, H. T. Yi, C. L. Zhang, and S.-W. Cheong, "Formation of Pancakelike Ising Domains and Giant Magnetic Coercivity in Ferrimagnetic $LuFe_2O_4$," Phys. Rev. Lett. **101**, 137203 (2008).

[102] H. J. Xiang, E. J. Kan, S.-H. Wei, M.-H. Whangbo, and J. Yang, "Origin of the Ising ferrimagnetism and spin-charge coupling in $LuFe_2O_4$," Phys. Rev. B **80**, 132408 (2009).

[103] G. Schütz, W. Wagner, W. Wilhelm, P. Kienle, R. Zeller, R. Frahm, and G. Materlik, "Absorption of circularly polarized x rays in iron," Phys. Rev. Lett. **58**, 737 (1987).

[104] W. S. Lovesey and S. P. Collins, *X-ray scattering and absorption by magnetic materials* (Oxford : Clarendon Pr., 1996).

[105] B. T. Thole, P. Carra, F. Sette, and G. van der Laan, "X-ray circular dichroism as a probe of orbital magnetization," Phys. Rev. Lett. **68**, 1943 (1992).

[106] K. Kuepper, M. Raekers, C. Taubitz, M. Prinz, C. Derks, M. Neumann, A. V. Postnikov, F. M. F. de Groot, C. Piamonteze, D. Prabhakaran, and S. J. Blundell, "Charge order, enhanced orbital moment, and absence of magnetic frustration in layered multiferroic LuFe(2)O(4)," Phys. Rev. B **80**, 220409 (2009).

[107] A. Narayanasamy, T. Nagarajan, P. Muthukumarasamy, and N. Kimizuka, "Mössbauer studies of a series of new compounds RFe_2O_4 (R = Y, Ho, Er, Tm, Yb)," phys. stat. sol. (a) **66**, 377 (1981).

[108] X. S. Xu, M. Angst, T. V. Brinzari, R. P. Hermann, J. L. Musfeldt, A. D. Christianson, D. Mandrus, B. C. Sales, S. McGill, J.-W. Kim, and Z. Islam, "Charge Order, Dynamics, and Magnetostructural Transition in Multiferroic $LuFe_2O_4$," Phys. Rev. Lett. **101**, 227602 (2008).

ACKNOWLEDGEMENTS

Here I would like to thank the following people, with out whom these work would not have been possible. I tried to remember everybody, but if you feel like I have missed you, I am very sorry.

Prof. Dr. Manuel Angst for the introduction to science, the great possibilities he offered to me and enlightening discussions.
Prof. Dr. Uwe Klemradt for his agreement to do the second revision of this thesis..
Prof. Dr. Thomas Brückel for the chance to write this thesis in his wonderful institute.
Joost de Groot for being a great tutor during my whole thesis.
Dr. Jörg Strempfer, Dr. Dinesh Kumar Shukla, Dr. Sonia Francoual for their help during the experiment at the P09 PETRA-III beamline at DESY.
Dr. Yixi Su for his help, discussions and ideas during the DNS experiment at FRM II.
Dr. Richard Rosenberg and **Dr. David Keavney** for the assistance during the 4-ID-C beamtime at the APS.
Jörg Perßon for introduction to crystal growth and Laue Diffraction.
Shilpa Adiga for the heat capacity measurement and organizing PPMS time whenever there was an urgent need.
The other members of the Helmholtz Young Investigator group **Pankaj Thakuria** and **Hailey Wiliamson** I really enjoyed working with you.
Dr. Susanne Mayer for the crystal alignment for the DNS experiments.
Arthur Glavic for his nice program to plot and analyse DNS Data.
The whole JCNS-2 / PGI-4 Institute for a pleasant working atmosphere.

Support from the initiative and networking fund of Helmholtz Association by funding the Helmholtz University Young Investigator Group "Complex Ordering Phenomena in Multifunctional Oxides" is gratefully acknowledged.
Use of the Advance Photon Source was supported by the U.S. Department of Energy, Office of Science, Office of Basic Energy Sciences, under Contract DE-AC02-06CH11357.

And I would like to thank **my family** for the support and love they gave to me.

LIST OF USED SYMBOLS AND ABBREVIATIONS

ABBREVIATIONS

- a.u. – arbitrary units
- CCD – Charge-coupled Device
- CO – charge order
- DNS – Diffuse Neutronen Streuung — instrument at FRM II
- FC – field cooling
- FRM II – Forschungs-Neutronenquelle Heinz Maier-Leibnitz in Garching
- f.u. – formula unit
- FW – field warming
- ICSD – inorganic crystal structure database
- MPMS – Magnetic Property Measurement System (SQUID)from Quantum Design
- NSF – non-spin-flip
- PPMS – Physical Property Measurement System from Quantum Design
- r.l.u – reciprocal lattice units
- RSO – Reciprocating Sample Option for the MPMS
- RT – room temperature
- RXD – resonant x-ray diffraction
- SF – spin-flip
- SQUID – Superconducting Quantum Interference Device
- TRM – thermo remanent magnetisation
- VSM – Vibrating Sample Magnetometer Option for the PPMS
- XMCD – X-ray magnetic circular dichroism
- ZFC – zero field cooling

SYMBOLS

- d – lattice plane spacing
- δ – derivation from stoichiometry in $YFe_2O_{4-\delta}$
- E – electric field strength
- ϵ – Polarization vector
- η – incident polarization angle to σ
- η' – angle of scattered polarization to σ'
- f – scattering amplitude
- F – Structure factor
- f_α– atomic form factor
- H – magnetic field strength
- I – Intensity
- λ – wavelength
- M – Magnetisation
- μ_{bohr} – Bohr magnetron
- n – integer
- ω – weighting factor
- P – Electric polarization
- $P0,P1,P2,P3$ – Stokes parameter
- π – Polarization inside the scattering plane
- $\mathbf{Q}$ – scattering vector
- $\bar{\mathbf{Q}}$ average scattering vector
- ρ – electric charge
- $\mathbf{r}_j$ – atomic positions
- S – Spin
- σ – Polarization perpendicular to scattering plane
- T – Temperature
- τ – incommensurate shifting in reciprocal space
- θ – scattering angle

- U – ration of CO_2 to H_2 during synthesis
- $\mathbf{U}_{ij}$ anisotropic displacement parameters
- V – volume

APPENDIX

A

A.1 RAW-DATA POWDER DIFFRACTOGRAM OF C001

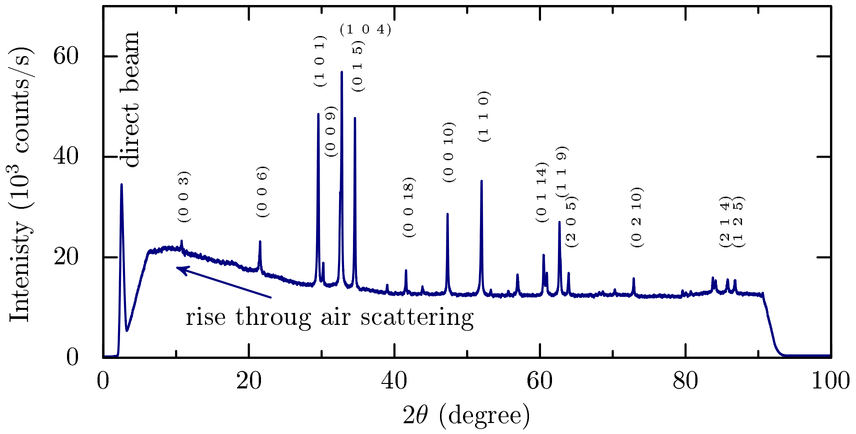

Figure A.1: Raw-data powder diffractogram of C001 (corrected data can be found in Figure 3.1).

A.2 lattice constants for powder samples

Sample	CO_2/H_2	a / b (Å)	c (Å)	R_{wp}
C001	2.50	3.51690(4)	24.7422(4)	0.021
C002	3.33	3.5148(4)	24.7485(4)	0.022
C003	4.17	3.51385(4)	24.7493(4)	0.023
C004	5.83	3.51147(8)	24.7650(7)	0.026
C005	5.00	3.51272(4)	24.7552(4)	0.018
C006	3.75	3.51460(5)	24.7479(5)	0.022
C007	4.58	foreign phase dominant		
C008	4.58	3.51285(5)	24.7540(5)	0.026
C009	5.42	3.51088(5)	24.7512(4)	0.020
C011	5.67	foreign phase dominant		
C012	2.92	3.51642(5)	24.7502(4)	0.024
C013	4.75	3.51222(4)	24.7562(4)	0.025
C014	4.38	3.51277(4)	24.7503(4)	0.024
C015	4.00	3.51300(5)	24.7486(4)	0.023
C016	4.17	3.51275(5)	24.7589(4)	0.022
C017	1.67	3.52252(3)	24.7141(3)	0.018

Table A.1: Lattice constant received from profile matching for different calcinations. Space group is set to $R\bar{3}m$ and angles are fix at $\alpha = \beta = 90^\circ$ and $\gamma = 120^\circ$.

A.3 MAGNETIZATION OF SAMPLE C006 AND C015

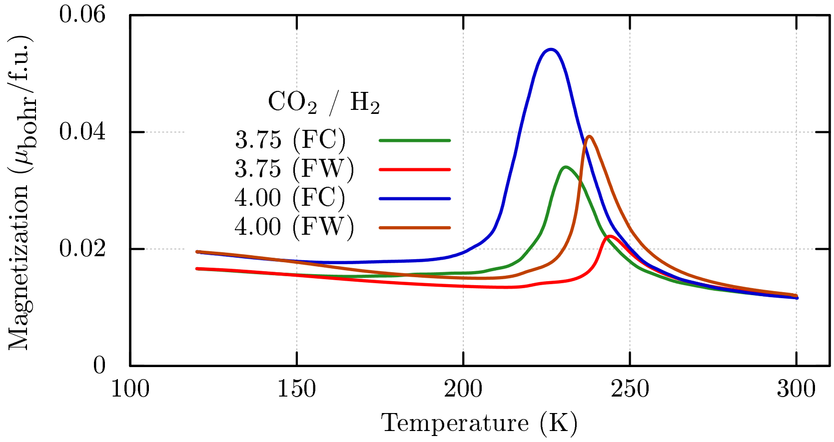

Figure A.2: Magnetization during field cooling and field warming at 3970 Oe for the calcinations C006 (CO_2/H_2 = 3.75) and C015 (CO_2/H_2 = 4.00).

A.4 MAGNETIZATION OF SAMPLE C017

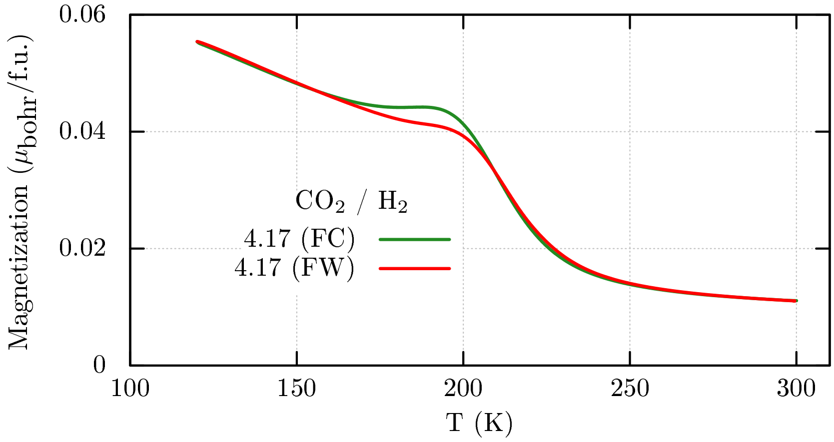

Figure A.3: Magnetization during field cooling and field warming at 3970 Oe for the calcination C017 (CO_2/H_2 = 1.67) .

A.5 MAGNETIZATION OF SAMPLE C014, C008, C013, C005 AND C009

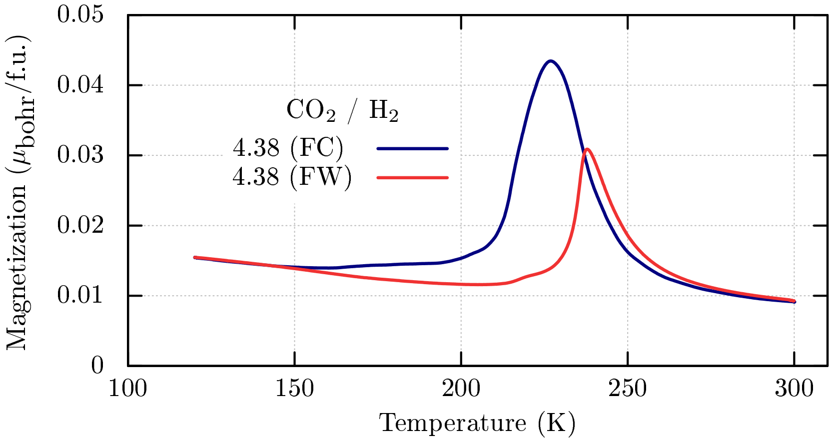

Figure A.4: Magnetization during field cooling and field warming at 3970 Oe for the calcination C014 (CO_2/H_2 = 4.38) .

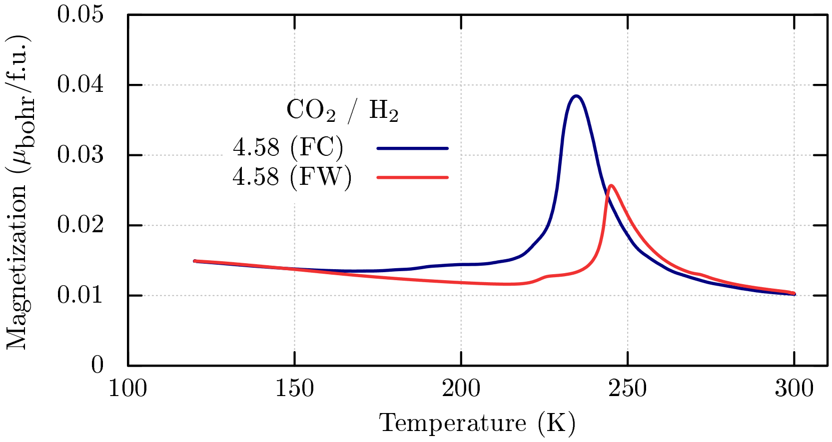

Figure A.5: Magnetization during field cooling and field warming at 3970 Oe for the calcination C008 (CO_2/H_2 = 4.58) .

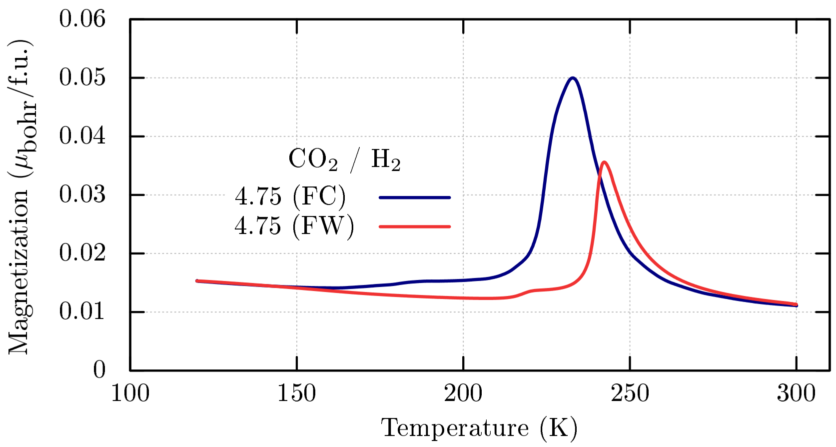

Figure A.6: Magnetization during field cooling and field warming at 3970 Oe for the calcination C013 ($CO_2/H_2 = 4.75$).

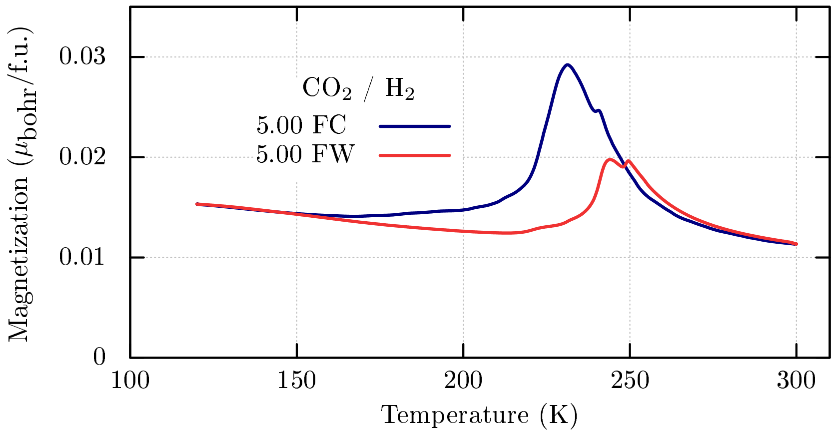

Figure A.7: Magnetization during field cooling and field warming at 3970 Oe for the calcination C005 ($CO_2/H_2 = 5.00$).

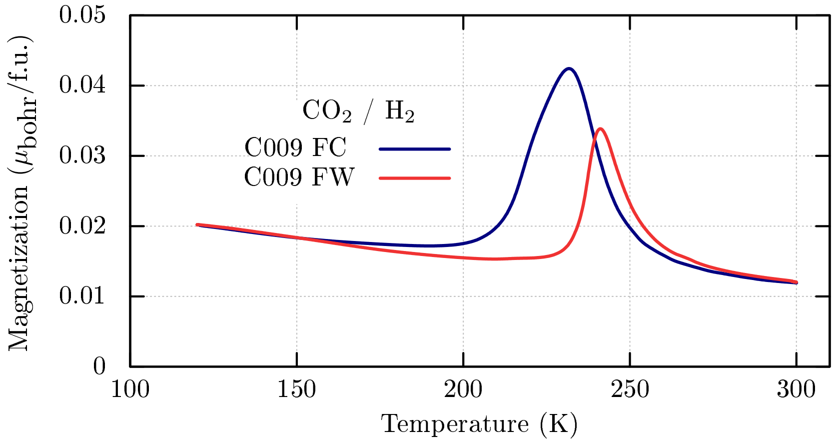

Figure A.8: Magnetization during field cooling and field warming at 3970 Oe for the calcination C009 ($CO_2/H_2 = 5.42$).

A.6 MAGNETIZATION OF Z2GINF_S3

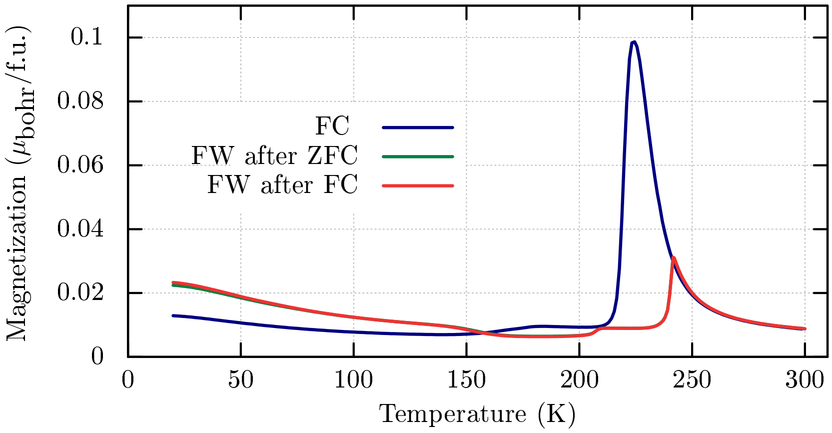

Figure A.9: Magnetization during field cooling and field warming at 3970 Oe after field cooling and zero field cooling for stoichiometric sample Z2Ginf_S3. Both field warming curves were measured after cooling with 10 K/min. While the cooling rate during measurement was 2 K/min. This leads to the difference at lower temperatures between FC and FW after FC. With the same cooling rate the curve would look like the Type B sample in Figure 3.14.

A.7 CRYSTAL STRUCTURE DATA

A.7.1 *Non stoichiometric single crystal Z1*

Atom	(Wyc)	x	y	z
Y	3a	$0.\bar{6}$	$0.\bar{3}$	$0.\bar{3}$
Fe	6c	1	0	0.21435(06)
O1	6c	1	0	0.29238(28)
O2	6c	$0.\bar{6}$	$0.\bar{3}$	0.20568(45)

Table A.2: Atomic positions of sample Z1 from structural refinement of single crystal x-ray data.

Atom	U11	U22	U33	U23	U13	U12
Y	.0047(07)	.0047(07)	.0668(15)	.000	.000	.0023(03)
Fe	.0194(08)	.0194(08)	.0104(09)	.000	.000	.0097(04)
O1	.0154(26)	.0154(26)	.0080(31)	.000	.000	.0077(12)
O2	.0315(37)	.0315(37)	.0362(51)	.000	.000	.0157(18)

Table A.3: Anisotropic displacement parameters of sample Z1 from structural refinement of single crystal x-ray data.

a (Å)	3.5199(3)	α / β (°)	90
c (Å)	24.822(2)	γ (°)	120
Volume (Å^3)	266.34(5)		
Reflections	1376	unique	114
R(int)	0.0456	R(σ)	0.0156
R1	0.0319	ωR2	0.0665
Goof	1.204		

Table A.4: Lattice constants and residuals from structural refinement of single crystal x-ray diffraction data of non stoichiometric sample Z1
.

A.7.2 *Stoichiometric single crystal Z8G5_S1*

Atom	(Wyc)	x	y	z
Y	3a	$0.\bar{6}$	$0.\bar{3}$	$0.\bar{3}$
Fe	6c	1	0	0.2143(1)
O1	6c	1	0	0.2921(2)
O2	6c	$0.\bar{6}$	$0.\bar{3}$	0.2050(5)

Table A.5: Atomic positions of sample Z8G5_S1 from structural refinement of single crystal x-ray data.

Atom	U11	U22	U33	U23	U13	U12
Y	.0033(6)	.0033(6)	.0632(15)	.000	.000	.0017(3)
Fe	.0174(7)	.0174(7)	.0070(09)	.000	.000	.0139(6)
O1	.0144(25)	.0144(25)	.0047(34)	.000	.000	.0112(16)
O2	.0309(35)	.0309(35)	.0244(50)	.000	.000	.0288(22)

Table A.6: Anisotropic displacement parameters of sample Z8G5_S1 from structural refinement of single crystal x-ray data.

a (Å)	3.51425(19)	α / β (°)	90
c (Å)	24.771(2)	γ (°)	120
Volume (Å^3)	264.94(6)		
Reflections	653	unique	118
R(int)	0.039	R(σ)	0.025
R1	0.047	ωR2	0.108
Goof	1.284		

Table A.7: Lattice constants and residuals from structural refinement of single crystal x-ray diffraction data of sample Z8G5_S1.

A.8 POLARIZATION ANALYSIS

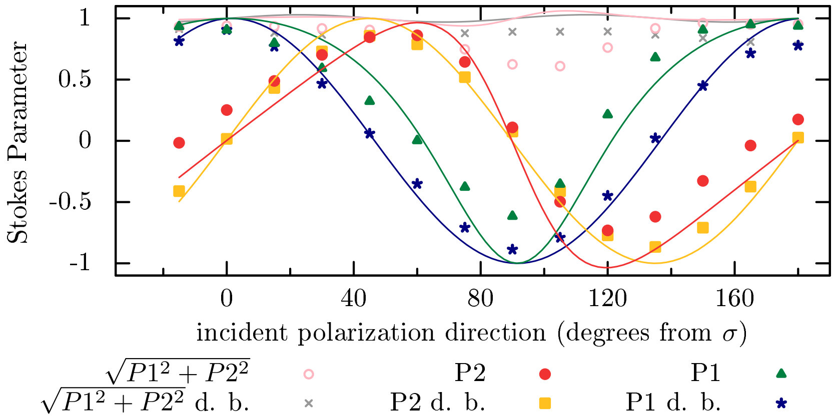

Figure A.10: [Polarization analysis at 120 K on 7125.5 eV feature in RXRD on ($\frac{1}{2}$, $\frac{1}{2}$, 10.6) superstructure reflection (errors are the size of the symbols or smaller). Amplitude of sinusoidal fit of the direct beam is fixed to 1.

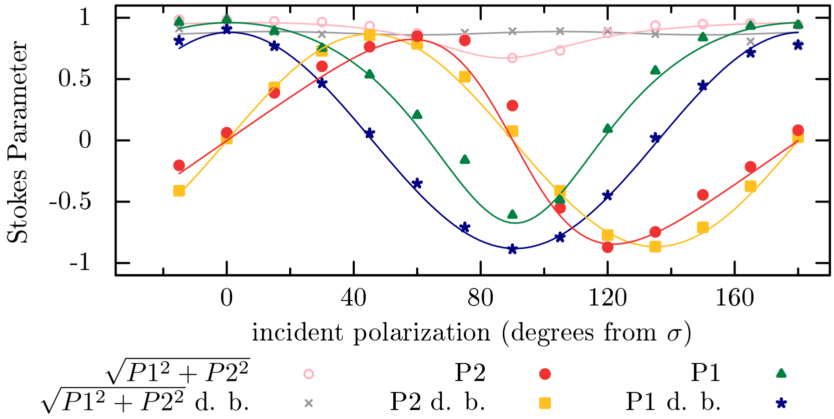

Figure A.11: Polarization analysis at 120 K on 7118 eV feature in RXRD on ($\frac{1}{2}$, $\frac{1}{2}$, 10.6) superstructure reflection (errors are the size of the symbols or smaller).

A.9 hhl-map at 236 k at dns

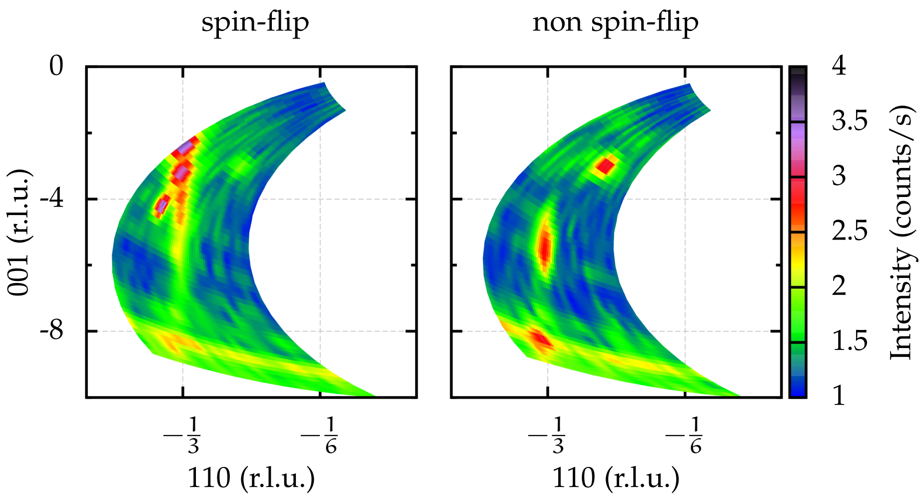

Figure A.12: hhl-plane at 236 K in spin-flip (left) and non spin-flip (right) channel with magnetic field $\mathbf{H} \parallel z$.

The hhl-map at 236 K shows in the spin-flip channel 3D-ordering in the (1/3 1/3 4)-region.

A.10 hhl-MAP AT DIFFERENT TEMPERATURES AT DNS

All figures in this AppendixA.10 are measured in spin-flip (left figure) and non spin-flip (right figure) channel with magnetic field $\mathbf{H} \parallel z$.

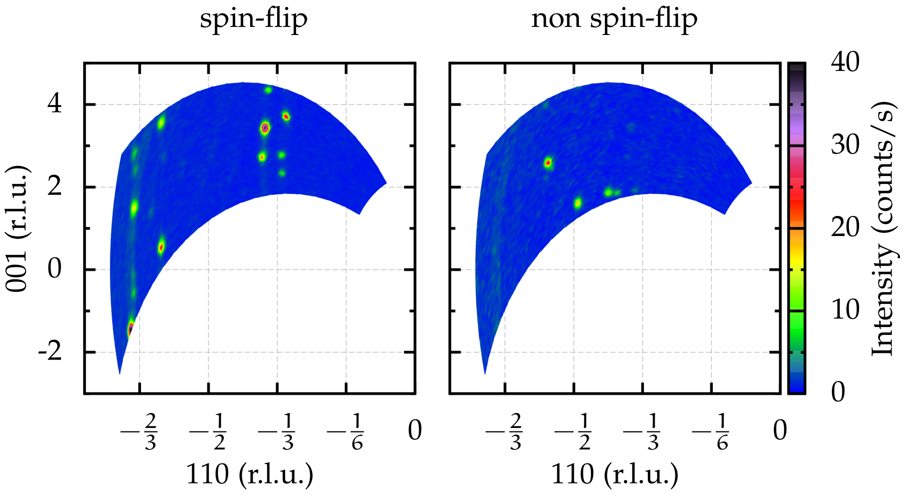

Figure A.13: hhl-plane at 160 K on warming.

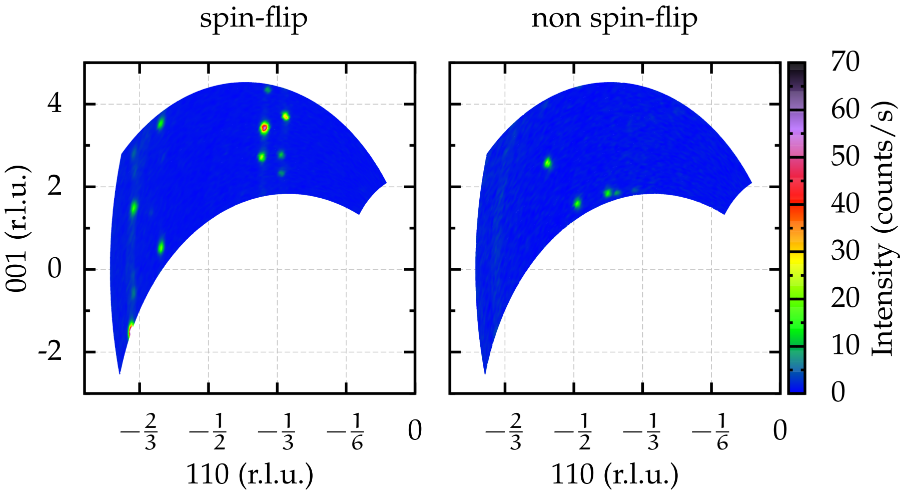

Figure A.14: hhl-plane at 170 K on warming — changed temperature scale.

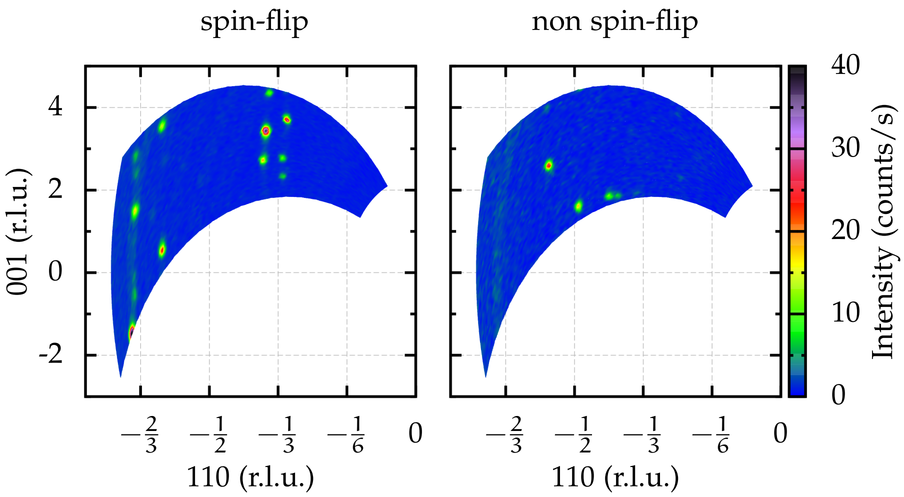

Figure A.15: hhl-plane at 185 K on warming.

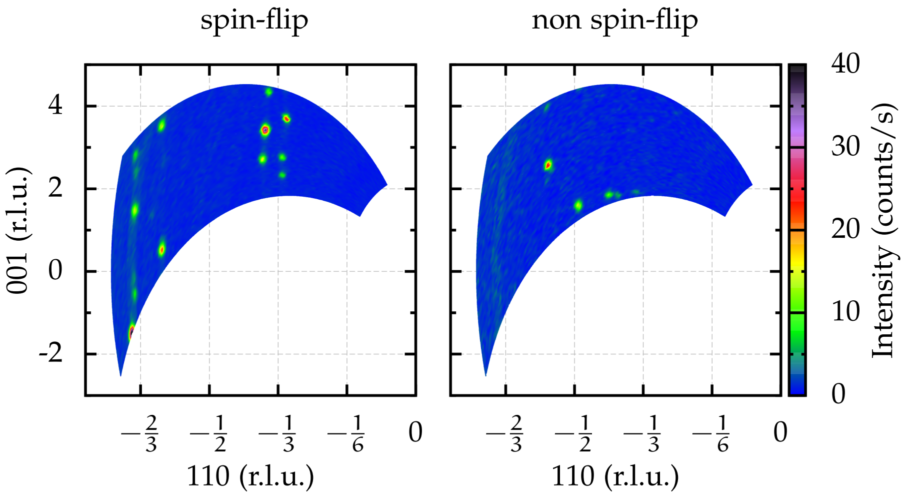

Figure A.16: hhl-plane at 205 K on warming.

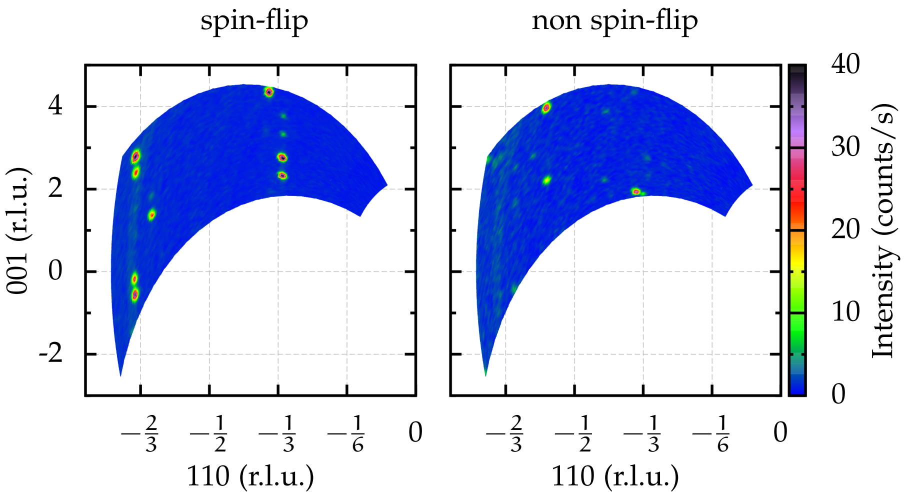

Figure A.17: hhl-plane at 220 K on warming.

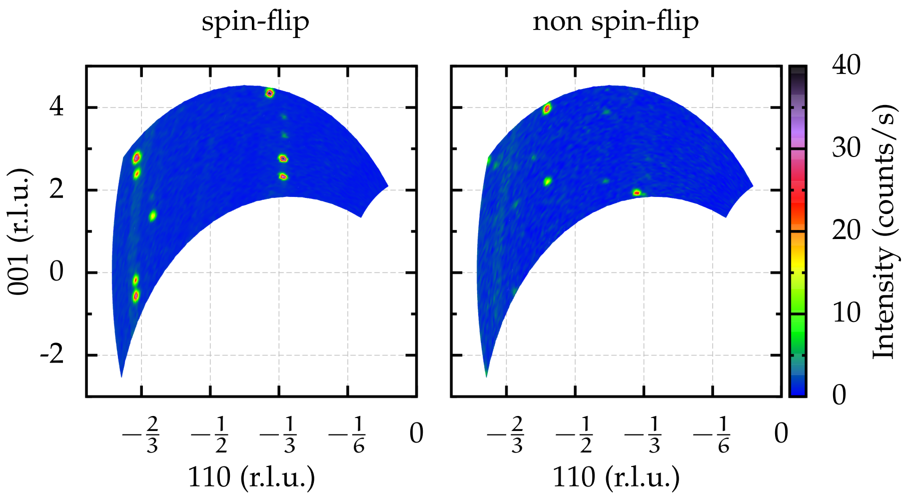

Figure A.18: hhl-plane at 230 K on warming.

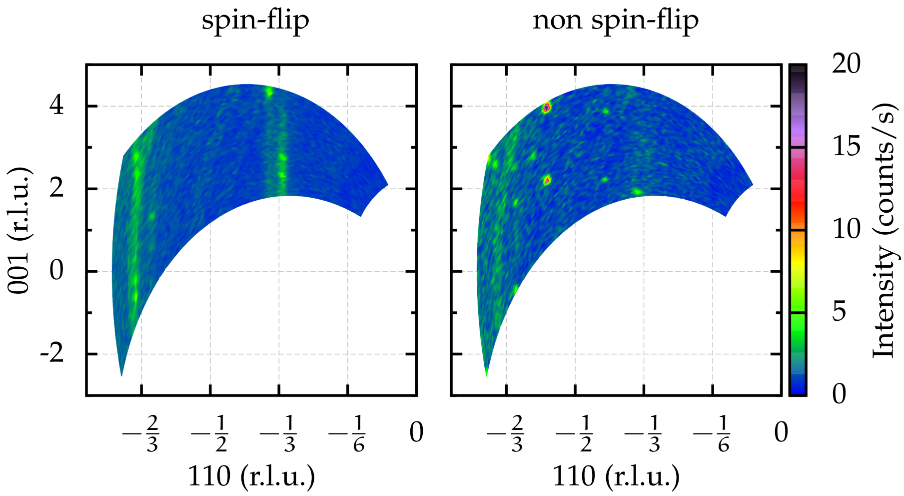

Figure A.19: hhl-plane at 240 K on warming — changed temperature scale.

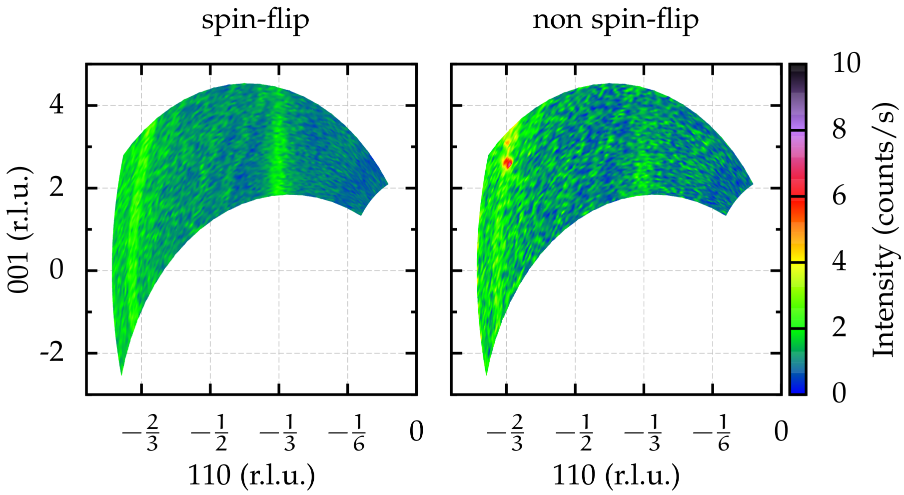

Figure A.20: hhl-plane at 255 K on warming — changed temperature scale.

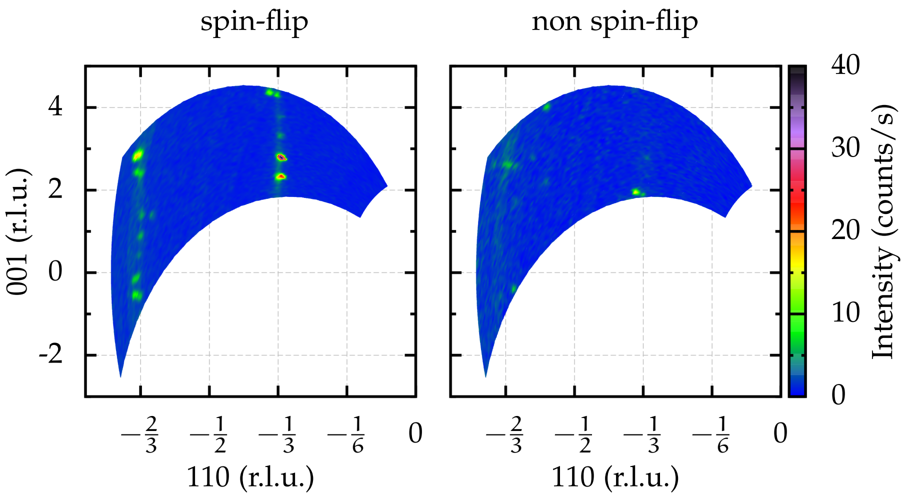

Figure A.21: hhl-plane at 230 K on cooling.

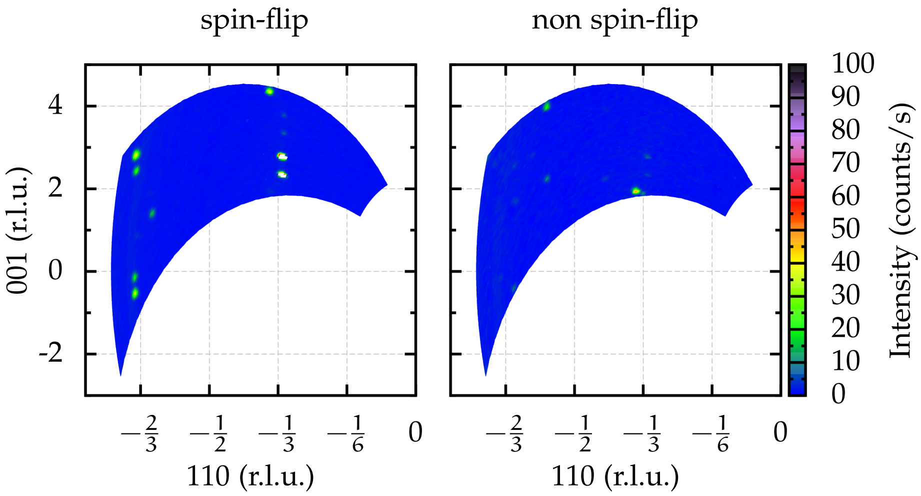

Figure A.22: hhl-plane at 220 K on cooling — changed temperature scale.

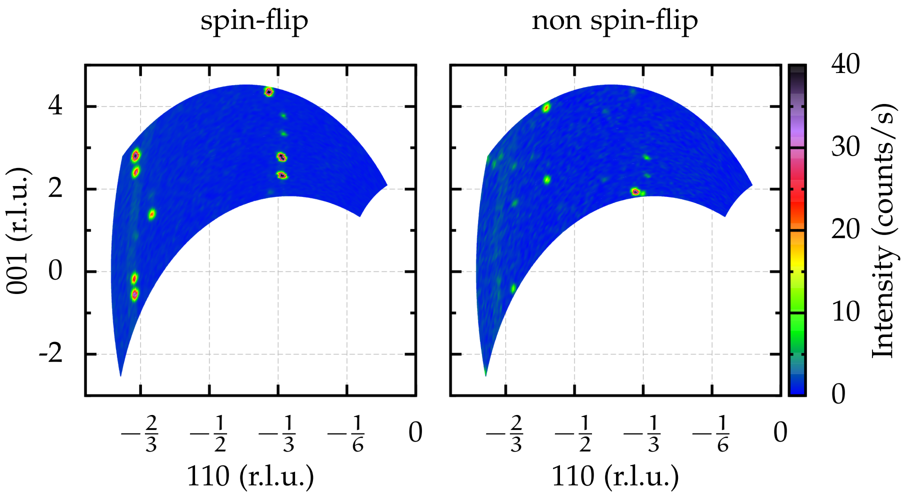

Figure A.23: hhl-plane at 205 K on cooling.

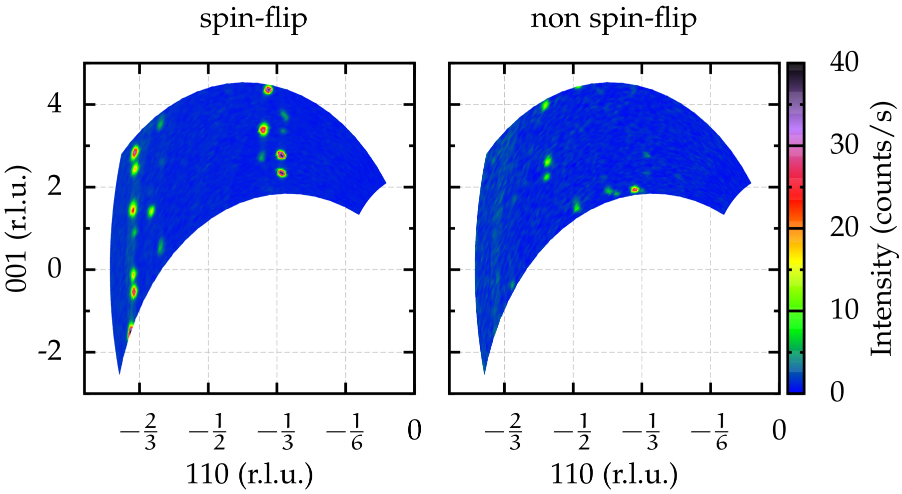

Figure A.24: hhl-plane at 190 K on cooling.

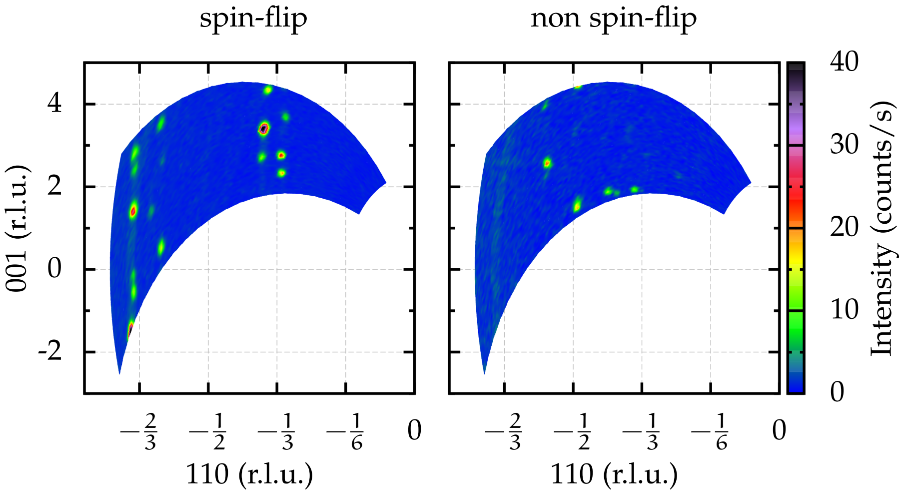

Figure A.25: hhl-plane at 180 K on cooling.

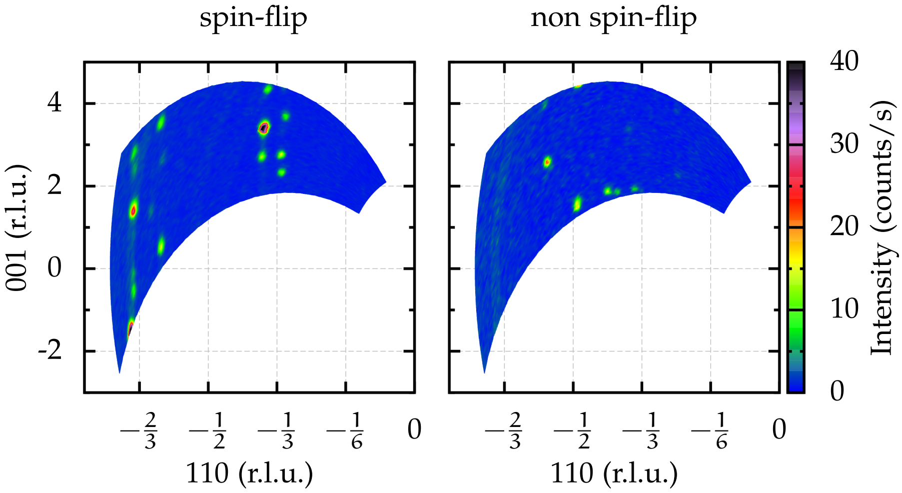

Figure A.26: hhl-plane at 170 K on cooling.

DECLARATION

Ich versichere, dass ich die Arbeit selbstständig verfasst und keine anderen als die angegebenen Quellen und Hilfsmittel benutzt sowie Zitate kenntlich gemacht habe.

Aachen, den 11.06.2012

Thomas Müller